SESSION II - CERAMICS AND NEW ALLOYS

MODELING OF FIBROUS PREFORMS FOR CVI FABRICATION

T.L. Starr

Georgia Tech Research Institute
Georgia Institute of Technology
Atlanta, Georgia 30332

We describe our ongoing efforts toward modeling the chemical vapor infiltration (CVI) of tube shapes, in support of experimental process development at Oak Ridge National Laboratory (ORNL). Model modifications needed to match the ORNL reactor include adding radiant heat transfer and adjusting heat transport conditions at the tube ends. Model densification times are in good agreement with experiment.

For this preform geometry higher gas flow rate and MTS concentration are needed for rapid densification. Higher furnace temperature can be used at these higher gas flow rates and as the tube densifies. A strategy for optimized processing may involve continuous variation of furnace temperature and control of gas flow rate for efficient utilization of MTS.

INTRODUCTION

Chemical vapor infiltration is an effective method for fabrication of tube shapes for fossil energy applications. Equipment design and process conditions are significantly different than for disk-shaped components fabricated previously. Also, our previously developed process model, GTCVI, required modification to include the radiative heat transfer that is an important feature of the ORNL tube CVI system. Initial modeling of the process indicated a need for higher gas flow rate and MTS concentration in order to achieve rapid densification. Further modifications, based on model results, toward optimizing the process are described below.

MODEL OF TUBE CVI SYSTEM

Our "finite volume" method for modeling of FCVI has been described previously[1] and involves dividing the CVI system into an orthogonal

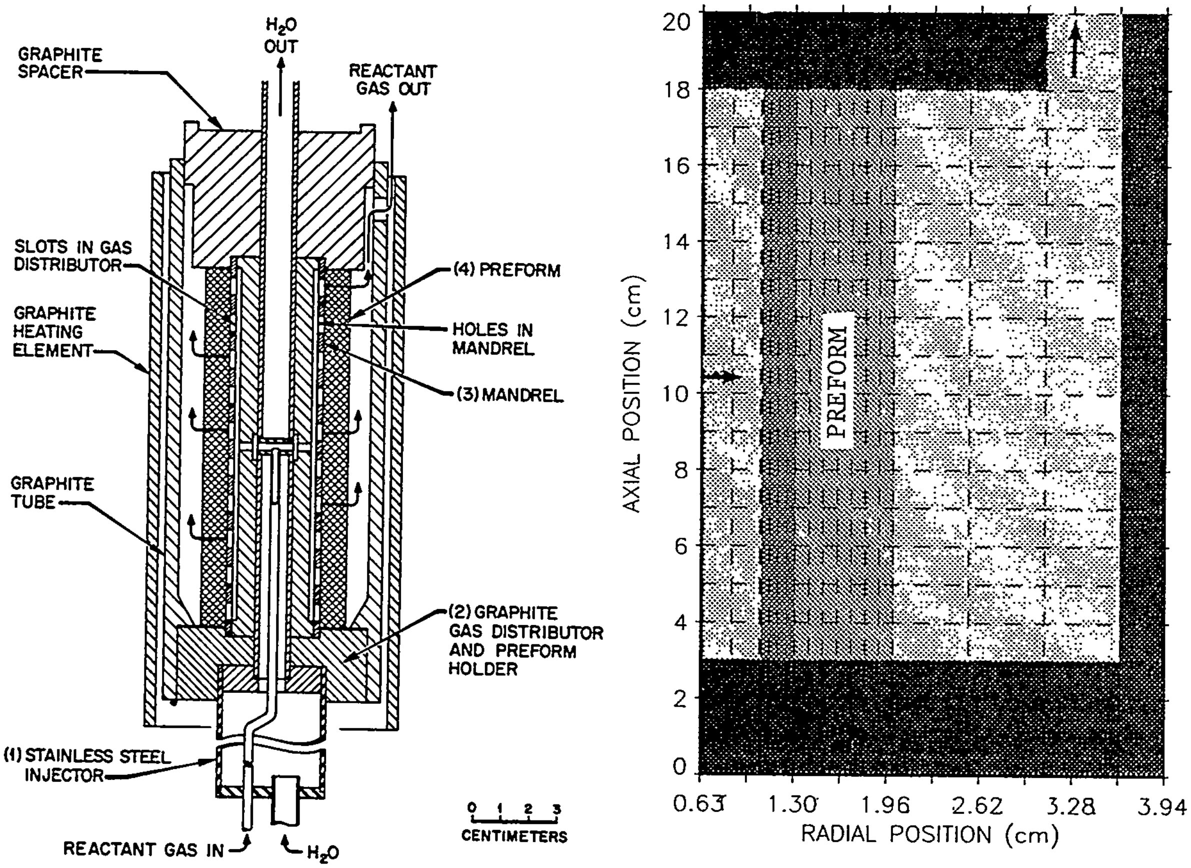

Figure 1. Experimental tube CVI system at Oak Ridge National Laboratory (left) is modeled using a 20x20 volume element grid (right).

array of volume elements. For the tube infiltration system at ORNL (Figure 1) heating of the preform is accomplished primarily by radiation from the hot reactor wall which is held at a set temperature. A mixture of hydrogen and MTS is introduced from a water cooled gas injector in the center of the tube preform. The thermal conductivity of the gas distributor and mandrel is minimized to allow the ID of the preform to reach deposition temperature. Process control parameters include the temperature of the furnace, the overall gas flow rate and the concentration of MTS in the infiltration gas.

PROCESS OPTIMIZATION

"Optimized" process parameters should yield high strength material densified in a short time and with efficient reagent use. The requirement of high strength material yields two process limitations: 1) limit the temperature in the composite to 1200°C to avoid thermal degradation of fiber properties, and 2) maintain H_2:MTS ratio greater than 5 to avoid deposition of free silicon. We have examined four sets of processing conditions in the light of these goals and limitations. These process conditions are described in Table I. Process conditions A and B correspond to experimental runs at ORNL, while conditions C and D correspond to adjusted conditions that should produced reduced processing times.

Table I. Four sets of processing conditions are modeled.

	A	B	C	D
Furnace temperature (C)	1275	1250	1250; 1300 after 10 hours	1300
H_2 flow (sccm)	630	1000	1000	2000
H_2/MTS	10	6	6	6

Set A corresponds to process conditions used at ORNL early in 1993. Densification times under these conditions were found to be very long, greater than 60 hours. Model results agree with experiment, as shown in Figure 2, showing only about 80% full density after 40 hours of processing. Examination of MTS utilization (Figure 3) indicates that nearly 90% of the MTS introduced into the system is converted to matrix material. Thus, the densification rate is limited by the MTS flow rate.

Set B corresponds to more recent experiments at ORNL with higher MTS and H_2 flow rates and a slightly lower furnace temperature. Model

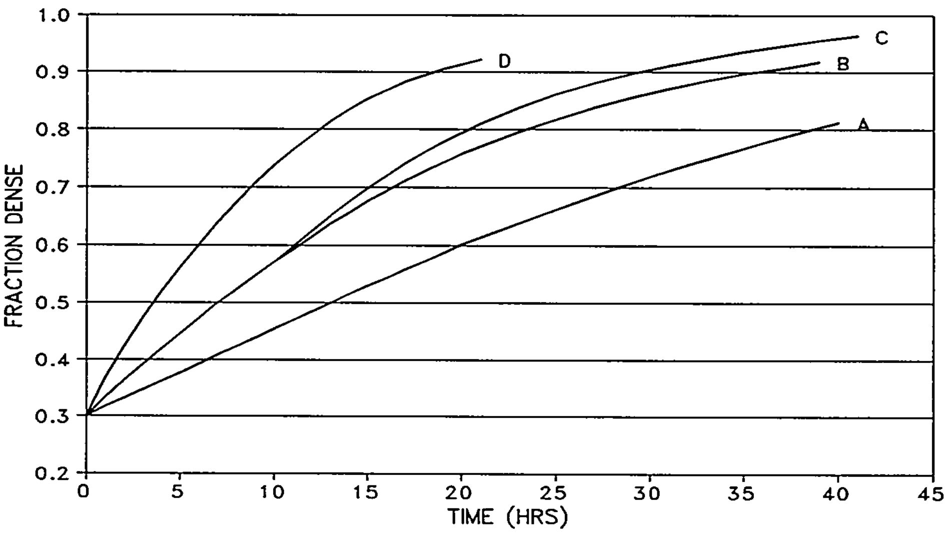

Figure 2. Densification time varies with different processing conditions.

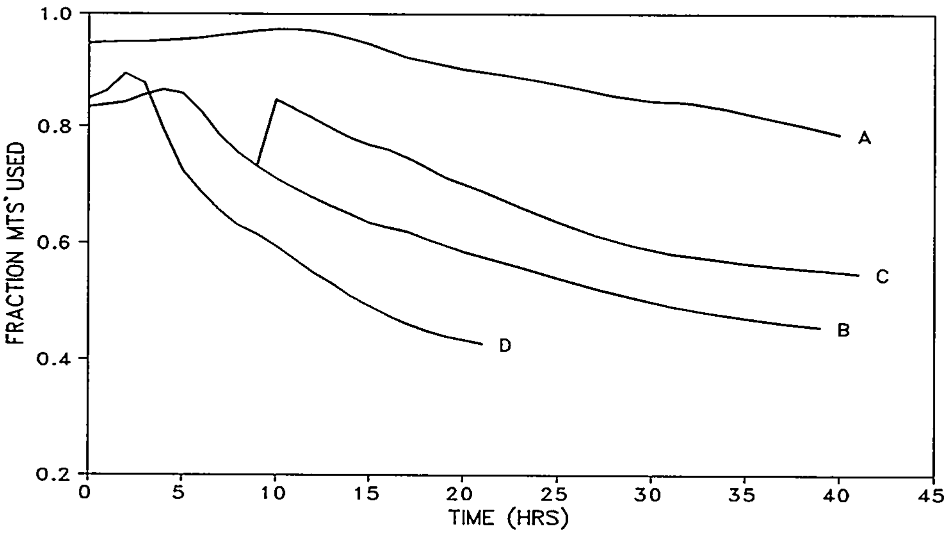

Figure 3. MTS utilization varies with time and processing conditions.

densification time matches experimentally observed time of 40 hours. Although the utilization of MTS is lower on a percentage basis, the higher overall flow yields more rapid densification. The lower furnace temperature yields a temperature in the composite that is lower initially than the 1200°C limit and decreases further as the composite becomes more dense (Figure 4).

In set C we see the effect of increasing the furnace temperature by 50°C after 10 hours of processing. Densification time is reduced by approximately 5-6 hours and the highest temperature in the composite rises above 1200°C only briefly. Set D corresponds to a higher temperature from the beginning of the process and a doubling of the gas flow rate. The corresponding densification time is about 20 hours (Figure 2). Although the temperature in the composite is slightly higher than 1200°C initially, it drops below this limit after 6 hours of processing (Figure 4). Initially between 80-90%. MTS utilization drops below 60% after 10 hours of processing.

SUMMARY

These model runs suggest a strategy for optimizing and controlling the tube CVI process. Since the thermal conductivity of the composite increases during densification, the outer diameter of the tube grows progressively cooler. To maintain a high deposition rate throughout the run the furnace temperature should be increased so as to maintain the highest permissible temperature at the tube O.D. (1200°C for Nicalon). The overall gas flow rate then is adjusted to yield approximately 80% MTS utilization. Higher MTS use would reduced densification rate due to reagent depletion while lower MTS use would increase material and cleanup costs. We plan to use this strategy with the model to select an "optimum" process profile including temperature and gas flow variation. Experimental measurement of preform temperature and outlet gas composition may be useful process monitors for tube CVI.

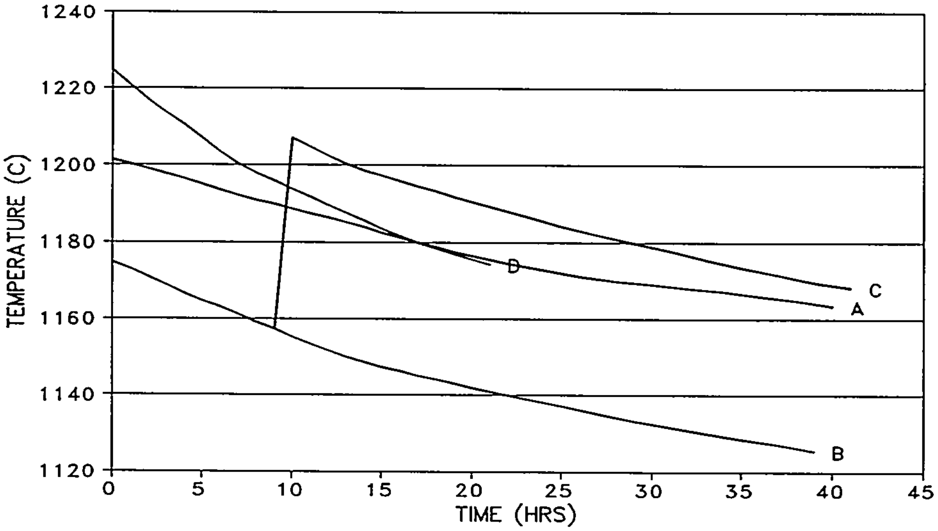

Figure 4. Temperature at tube O.D. decreases during run as density increases.

REFERENCES

1. T.L. Starr and A.W. Smith, "Modeling of Forced Flow/Thermal Gradient Chemical Vapor Infiltration", Oak Ridge National Laboratory Report ORNL/sub/85-55901/03 (September 1993).

DEVELOPMENT OF OXIDATION-RESISTANT INTERFACE COATINGS

R. A. Lowden, O. J. Schwarz, and D. P. Stinton

Oak Ridge National Laboratory
P. O. Box 2008
Oak Ridge, TN 37831-6063

ABSTRACT

Porous silicon carbide (SiC) was examined as an interlayer to improve the elevated-temperature stability of Nicalon[•]/SiC composites. Porous SiC coatings were deposited on fibrous preforms from gas mixtures containing methylsilane (CH_3SiH_3), methane (CH_4), argon, and hydrogen. The effects of the carbon to silicon ratio and the concentration of hydrogen in the gas mixture, on the microstructure and composition of the SiC interlayer were examined. The coated preforms were densified with a silicon carbide matrix using the forced-flow, thermal-gradient chemical vapor infiltration (FCVI) process. Room-temperature flexure strengths of as-fabricated composites and specimens exposed to 1273 K in air for 24 h, were measured to assess the effectiveness of the interlayer. Layer thickness, microstructure, and composition influenced as-fabricated and post-exposure properties. Materials fabricated with a variety of porous SiC coatings showed improvements in retained strength as compared to those with traditional carbon coatings.

INTRODUCTION

Continuous fiber-reinforced SiC matrix composites are being developed for use in high-temperature oxidative environments.[1,2] These materials typically use graphitic carbon interface coatings to limit the forces acting at the fiber-matrix interface and control mechanical properties.[3-5] Nicalon/SiC composites with a graphitic carbon interface layer exhibit properties favorable for use in fossil energy applications, and thus have been exposed to oxidizing and simulated fossil fuel environments to assess their stability.[6,7] Composite specimens with and without an external SiC surface coating were oxidized in air and exposed to a variety of combustion environments at

---

Nicalon[•], Nippon Carbon Company, Tokyo, Japan.

elevated temperatures. The mechanical properties of unprotected Nicalon/SiC specimens were degraded after short periods of exposure, due to the oxidation and removal of the carbon interface coating. Longer exposures resulted in the oxidation of the fibers and matrix to form silica, which with time bonded the components together, and produced brittle behavior. Combustion environments hastened the oxidation of the constituents, and thus the embrittlement of the composites.

The specimens protected by a SiC surface coating exhibited no decrease in strength after exposure to oxidative or combustion environments. The SiC layer sealed the surface of the composites, protecting the exposed fibers ends, and thus preventing oxidation at the fiber-matrix interface. Previous efforts in the use of topical coatings and sealants for carbon-carbon composites, however, have demonstrated that there are many difficulties associated with protective surface layers.[8] Processing flaws and cracks in the coating caused by thermal expansion mismatch stresses or applied loads, can expose the substrate, leaving it susceptible to oxidation. It is generally accepted that these surface protection measures are only one component of a more complex protection system. A complete system may require combinations of surface layers, oxidation inhibitors, and fiber coatings.

To date, much of the work on interface coatings with improved oxidation resistance for use in silicon-based ceramic composite materials has paralleled the efforts to advance the stability of carbonaceous materials, such as structural graphite and carbon-carbon composites. These efforts have focused on the development of glass forming materials, which when oxidized form a surface film that, at elevated temperatures, can flow to ensure complete coverage, seal cracks and pores, and impede attack of the underlying substrate. Most recent studies have focused on glasses with melting temperatures and viscosities lower than that of silica. Boron is the most frequently studied addition for temperatures around 1273 K.[9-11] Boron forms a lower melting glass ($T_m \approx$ 725 K) that flows more readily to seal the surface of the material. However, the high temperature stability of boria and the sensitivity of the glass to thermal shock and moisture are of concern.

It is speculated that the ideal interface layer for a Nicalon/SiC composite would be a modified form of SiC. The interlayer, and matrix would be thermochemically and thermomechanically stable with respect to each other and would exhibit similar stability at any operating temperature. An "all SiC" composite would be protected by a silica surface layer, adding to the life of the material in corrosive environments. The interlayer of choice would be a soft or low modulus SiC that would ensure debonding at the fiber-matrix interface and controlled fiber slip to produce toughness and gradual failure.

It has been shown that the properties of an interlayer can be altered by adjusting the porosity of the fiber coating material.[5] Porosity lowers the strength and modulus of a ceramic. Thus it is hypothesized that the properties of a fiber coating could be modified by including controlled porosity. This concept has been examined in the development of fuels for high temperature graphite reactors.[12] High-temperature gas-cooled reactor fuels were produced by encapsulating small spheres of uranium-containing compounds in a series of coatings beginning with a soft carbon layer and finishing with a SiC external coating. As in the Nicalon/SiC composites, the soft carbon inner layer was used to accommodate fuel expansion during the fission process, and had the additional purpose of offering void space for the gaseous fission byproducts. The SiC external layer acted as final containment for fission gases and provided mechanical integrity.

Silicon carbide is relatively unaffected by neutrons, thus modified SiC coatings were explored for replacing the graphite layers with some success. Porous, low modulus SiC coatings were deposited on fuel kernels from methylsilanes and subsequently sealed with a dense SiC outer skin. Limited success was reported for this application.

Similar coatings were employed for controlling the fiber-matrix interface in the Nicalon/SiC system.[5] It was thought that the low modulus SiC material would act much like the soft carbon interlayer typically used in these composites. Porous SiC coatings were deposited on fibrous preforms from methylsilane in argon at low temperatures (< 1000 K). These were densified with a SiC matrix and the properties of the composites and the fiber-matrix interfaces examined. Extensive fiber debonding and low interfacial forces were observed. However, the strength of the Nicalon fibers was severely degraded during interlayer deposition. It appeared that free silicon, present in the reactant gases or in the coating, reacted with the Nicalon fibers with deleterious effects. The latest attempts at a Porous SiC interlayer have included a 5-7 nm layer of carbon deposited from C_3H_6 to protect the fibers during processing.

This paper describes efforts to reexamine SiC derived from methylsilane as an interlayer for Nicalon/SiC composites. Coatings were deposited on fibrous preforms from gas mixtures containing varying concentrations of methylsilane, argon, methane, and hydrogen. The concentrations of methane and hydrogen were altered to examine the influence of carbon potential (carbon to silicon ratio) in the reactant gas mixture on the composition and microstructure of the deposits. Coating thickness and composition were varied. As-fabricated strength and short-term oxidation resistance were used to assess the effectiveness of the modified SiC as an interface coating for Nicalon/SiC composites.

EXPERIMENTAL PROCEDURE

Composite Fabrication

Fibrous preforms were fabricated by stacking multiple layers of Nicalon plain-weave fabric rotated in a 0 ± 30° sequence within the cavity of a graphite holder. The layers were hand compressed to produce a preform with a nominal fiber loading of 40 vol. % and were held in place by a perforated graphite lid pinned to the holder. The cloth sizing was removed through multiple washings with acetone. The nominal size of the disk-shaped fibrous preforms was 45 mm in diameter and 12.5 mm thick.

The sensitivity of the Nicalon fibers to degradation during exposure to methylsilane was previously described, and reconfirmed in this effort, thus a thin (< 50 nm) carbon layer was deposited on the fibers to protect the reinforcement during subsequent processing. The carbon layer was deposited at 1373 K and 3.3 kPa from a gas mixture containing propylene and argon using a forced-flow, isothermal technique. The fibers were then coated with the porous SiC interface layers. The coatings were deposited at 1373 K and 3.3 kPa from gas mixtures containing methylsilane, argon, methane, and hydrogen again using a forced-flow, isothermal method. The composition of the reactant gas mixture was varied to alter the composition and microstructure of the deposit (Table 1). Reactant flows were adjusted to produce deposition rates comparable to those of the standard graphitic carbon layer, and to produce a uniform layer throughout the preform. Layer deposition times were 1 h which produced coatings thicknesses of 0.2 - 0.5 μm. The thicknesses of the interface layers were calculated from weight gains and examined employing electron microscopy techniques .

The preforms were densified with silicon carbide using the FCVI process. The densification of porous structures using the FCVI process has been previously described in detail.[1,12-14] The SiC matrix was produced by the decomposition of methyltrichlorosilane (CH_3SiCl_3 or MTS) in hydrogen at a hot-surface temperature of 1473 K and atmospheric pressure. The preforms were infiltrated with SiC to 75 to 85 % of theoretical density in ~ 20 h.

Table 1. Interface coating deposition parameters.

CVI number	CH_3SiH_3 Flow (sccm)	CH_4 Flow (sccm)	Ar Diluent (sccm)	H_2 Diluent (sccm)	Weight gain (g)	C:Si Ratio
812	40	0	500	500	2.78	1
820	30	0	500	500	2.60	1
821	20	0	500	500	1.50	1
822	40	250	250	500	3.50	7.25
832	40	500	0	500	3.40	13.5
833	40	250	500	250	3.20	7.25
834	40	500	500	0	3.60	13.5

Characterization and Testing

Test bars were cut from the samples parallel to the 0° orientation of the top layer of cloth using a diamond saw, and tensile and compressive surfaces were ground parallel to the long axis of the specimen. The average dimensions of the specimens were 2.5 x 3 x 40 mm and all specimens were measured and weighed to determine densities.

Half of the specimens were oxidized in static air at 1273 K for 24 hours. Flexure bars were placed on an alumina plate in the cavity of an atmospheric box furnace and heated to temperature at a rate of 300°/h. Once the furnace achieved equilibrium, the final temperature was measured using a hand-held optical pyrometer and then maintained using a thermocouple-controlled programmer. At the specified time, the furnace was shut off and allowed to cool unassisted.

Room temperature flexure strengths for as-fabricated and heat-treated composites were measured in four-point bending. A support span of 25 mm and a loading span of 6 mm were used with a crosshead speed of 0.50 mm/min. The load was applied perpendicular to the layers of cloth. Load-displacement curves were recorded to examine the fracture process and determine the loads for ultimate strength calculations. Fracture surfaces of the specimens were examined using a scanning electron microscope. Interlayer composition and microstructure were characterized employing transmission electron microscopy.

RESULTS

Mechanical Properties

The densities and room-temperature flexure strengths for the composites are summarized in Table 2. Typical load-displacement curves for the as-fabricated Nicalon/SiC composites with the methylsilane-derived interlayers of varying thickness and composition are shown in Fig. 1. Strength and toughness were influenced by coatings thickness and composition (Tables 1 and 2). Coating thickness seemed to optimize mechanical properties at a thickness of $\approx .36\mu m$. Mechanical properties of composites containing porous SiC coatings with additional carbon from CH_4 seemed most improved with increasing C:Si ratio and Ar diluent.

Oxidation

Exposure to 1273 K in air for 24 h produced a slight discoloration of all specimens suggesting some degree of surface oxidation. Specimens with a carbon interface exhibited significant losses in flexure strength after the short-term exposure oxidation, retaining an average of only 25% of their as-fabricated strength. Performance was far better for specimens with the porous SiC interface. The most promising samples retained up to 76% of their as-fabricated strengths. Toughness of the porous SiC samples was little effected by oxidation.

Characterization

Preliminary analysis of the interlayers was conducted. The layers deposited from methylsilane in argon were found to be amorphous with high silicon concentrations. The coatings fabricated from gas mixtures containing methane were more crystalline with compositions closer to that of stoichiometric SiC. Interlayers from the highest methane additions contained small carbon inclusions.

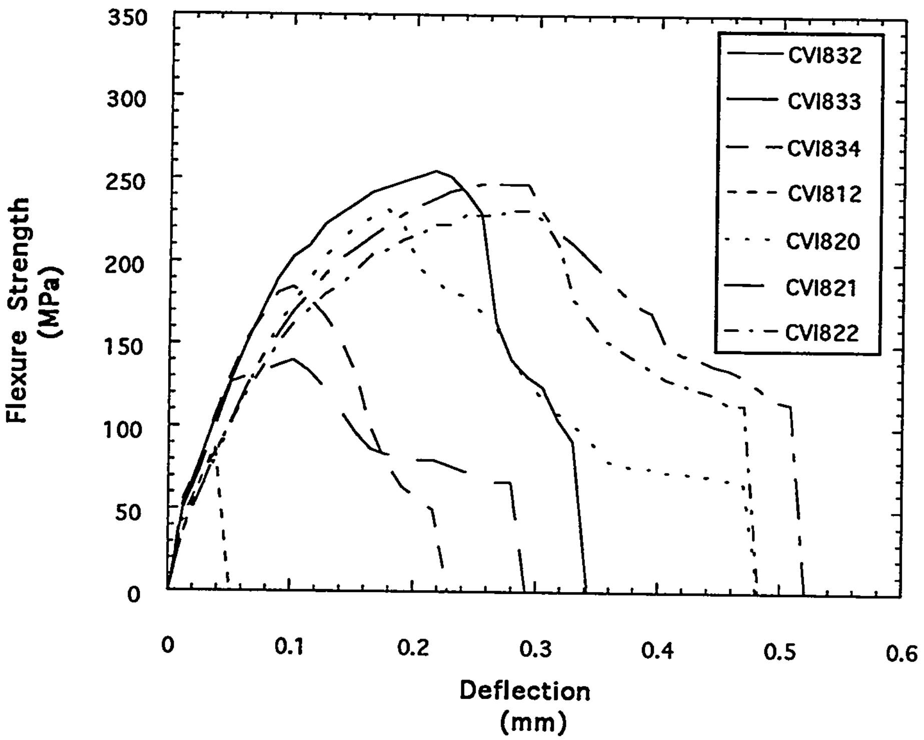

Figure 1. Representative load-deflection curves for as-fabricated composites with methylsilane-derived SiC interface coatings.

Table 2. Flexure Strengths for Nicalon/SiC Composites with a SiC Interface Coating

CVI Number	Average Density (g/cc)	Coating Thickness (μm)	As-Fabricated Strength (MPa)	Post-Exposure Strength (MPa)
carbon	2.50	0.35	404 ± 67	108 ± 14
812	2.26	0.38	78 ± 16	79 ±18
820	2.18	0.36	224 ± 27	148 ± 45
821	2.35	0.21	169 ± 56	89 ± 15
822	2.30	0.49	179 ± 85	83 ± 33
832	2.42	0.47	155 ± 58	99 ± 36
833	2.38	0.45	175 ± 62	120 ± 50
834	2.38	0.50	174 ± 70	132 ± 53

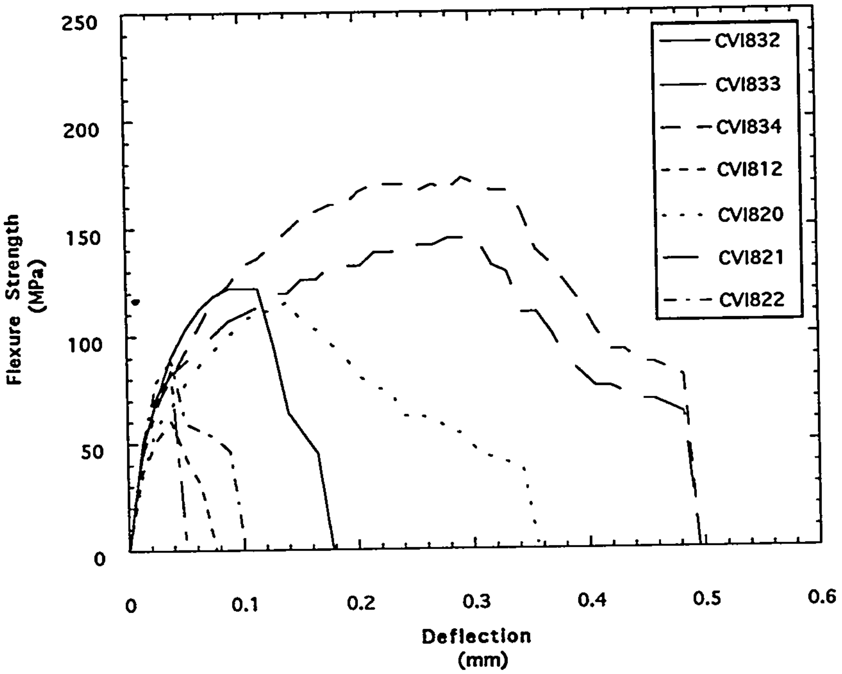

Figure 2. Representative load-deflection curves for oxidized composites with methylsilane-derived SiC interface coatings.

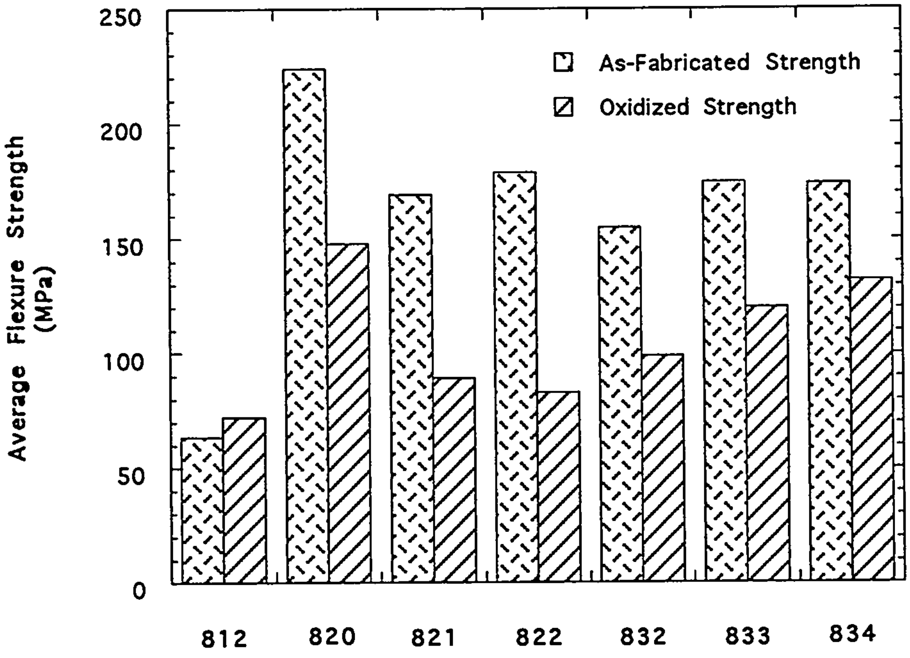

Figure 3. Flexure strength comparison of as-fabricated and oxidized composites with SiC interface coatings.

DISCUSSION

Oxidation poses problems with traditional carbon interface coatings that simple overcoating alone cannot always solve. During oxidation, the carbon interlayer is removed in the form of carbon monoxide. With further oxidation, the matrix and fiber form a silica layer that eventually bonds the components together, resulting in brittle fracture behavior of the composite. Protection of the composite with a SiC overcoating can have a limited effectiveness as processing flaws, or cracks in the coating caused by thermal expansion mismatch stresses or applied loads, can expose the underlying fiber coatings, leaving them susceptible to oxidation. An oxidation resistant fiber coating would seem to be the solution.

Coatings were deposited from CH_3SiH_3 gas mixtures to examine the effect of porous SiC interface layers. Little information regarding the decomposition of methylsilane has been reported. The limited information from the coating of nuclear materials demonstrated that composition and microstructure could be controlled through changes in processing temperature, methylsilane concentration, and selection of carrier gas composition (argon and hydrogen mixtures).[12] In the work presented here, layers deposited from methylsilane in argon were amorphous and Si-rich. The addition of methane during deposition resulted in the formation of a more stoichiometric coating with improved crystallinity.

The as-fabricated strengths of the composites were lower than those observed for composites of similar construction but with different interface layer chemistries. This suggests that the fibers were degraded during processing in spite of the carbon precoating. As with carbon interlayers, strength was influenced by coating thickness, thus the layers could be acting to absorb some of the residual thermal expansion mismatch stresses.

Strength retention improved with increased carbon content in the gas mixture. The interlayers were more structured and closer to SiC in composition. Post-exposure strength retention was better than for composites with carbon interlayers, however, the results are only preliminary in nature. Additional effort is needed to better understand the processing-composition-property relationships for the interlayers, and the subsequent effect of these parameters on the behavior and stability of composites using them.

CONCLUSIONS

Porous silicon carbide deposited from methylsilane was investigated as an interface layer for Nicalon/SiC composites. The composition of the reactant gas mixture was varied to produce coatings with different structures and compositions. In general, the as-fabricated strengths were not as high as those for composites with carbon interlayers, however, the porous SiC coated composites retained a far greater portion of their strength after oxidation.The thickness of the interlayer influenced both as-fabricated and post-exposure strengths, however, for a given coating thickness, as-fabricated properties were unaffected by composition. The carbon content of the gas mixture did influence post-exposure strength. Strength retention was improved with increasing methane concentration.

ACKNOWLEDGEMENTS

This research is sponsored by the U.S. Department of Energy, Fossil Energy AR&TD Materials Program, under contract DE-AC05-84OR21400 with Martin Marietta Energy Systems, Inc. The authors would like to thank the ORNL High Temperature Materials Laboratory User Center for the use of the Hitachi S-800 scanning electron microscope and access to the other analytical and mechanical property testing equipment.

REFERENCES

1. T. M. Besmann, B. W. Sheldon, R. A. Lowden, and D. P. Stinton, "Chemical Vapor Infiltration," *Science* **253**, pp. 1104-1109, September 6, 1991.

2. R. Warren, *Ceramic Matrix Composites*, Chapman and Hall, New York, New York (1992).

3. R. A. Lowden, "Fiber Coatings and the Mechanical Properties of a Fiber-Reinforced Ceramic Composite," pp. 619-630 in *Ceramic Transactions*, Vol. 19, Advanced Composite Materials, ed. by Michael D. Sacks, The American Ceramic Society, Westerville, Ohio (1991).

4. R. A. Lowden, "Interface Effects and Fracture in Nicalon/SiC Composites," pp. 97-114 in the *Proceedings of the Fourth Annual Conference on Fossil Energy Materials*, ed. by R. Judkins, Oak Ridge, TN, May 15-17, 1990.

5. R. A. Lowden, *Characterization and Control of the Fiber-Matrix Interface in Ceramic Matrix Composites*, ORNL/TM-11039, March 1989.

6. R. A. Lowden and R. D. James, *High Temperature Corrosion of Nicalon/SiC Composites*, ORNL/TM-11893, August 1991.

7. R. D. James, R. A. Lowden, and K. L. More, "The Effects of Oxidation and Corrosion on the Properties of Nicalon®/SiC Composites," pp. 925-935 in *Ceramic Transactions*, Vol. 19, Advanced Composite Materials, ed. by Michael D. Sacks, The American Ceramic Society, Westerville, Ohio (1991).

8. J. E. Sheehan, "Oxidation-Resistant Carbon-Carbon Composites," pp. 920-923 in *Engineered Materials Handbook*, Vol. 1: Composites, ASM International, Metals Park, Ohio (1987).

9. D. W. McKee, C. L. Spiro, and E. J. Lamby, "The Effects of Boron Additives on the Oxidation Behavior of Carbons," *Carbon* 22[6], 507-511 (1984).

10. P. Ehrburger, P. Baranne, and J. Lahaye, "Inhibition of the Oxidation of Carbon-Carbon Composite by Boron Oxide," *Carbon* 24[4], 495-499 (1986).

11. D. W. McKee, "Borate Treatment of Carbon Fibers and Carbon/Carbon Composites for Improved Oxidation Resistance," *Carbon* 24[8], 737-741 (1986).

12. P. Angelini, “Chemical Vapor Deposition of Silicon carbide from Methylsilan and Coating of Nuclear Waste Ceramics,” Ph. D. dissertation, University of Tennessee, June 1985.

13. D. P. Stinton, A. J. Caputo, and R. A. Lowden, "Synthesis of Fiber-Reinforced SiC Composites by Chemical Vapor Infiltration," *Am. Ceram. Soc. Bull.* 65(2), 347-350 (1986).

14. A. J. Caputo, D. P. Stinton, R. A. Lowden, and T. M. Besmann, "Fiber-Reinforced SiC Composites with Improved Mechanical Properties," *Am. Ceram. Soc. Bull.* 66(2), 268-272 (1987).

15. T. M. Besmann, R. A. Lowden, D. P. Stinton, and T. L. Starr, "A Method for the Rapid Chemical Vapor Infiltration of Ceramic Composites," *J. de Physique* 5(50), Colloque C5, 229-239 (1989).

16. J. J. Brennan, "Interfacial Characterization of Glass and Glass-Ceramic Matrix/Nicalon SiC Fiber Composites," *MRS Proceedings, Vol. 20, Tailoring Multiphase and Composite Ceramics,* ed. R. E. Tressler et al., Plenum Publishing Corporation, 549-560 (1986).

JOINING OF SiC CERAMICS AND SiC/SiC COMPOSITES

B. H. Rabin

Idaho National Engineering Laboratory
P.O. Box 1625
Idaho Falls, ID 83415-2218

ABSTRACT

Reaction processing methods have been developed and employed to produce SiC-to-SiC joints for use in elevated temperature fossil energy applications. The strength and fracture toughness of joints were characterized and found to be comparable to commercial bulk reaction bonded silicon carbide (RBSC), making these joints potentially useful for service temperatures exceeding 1000°C. Recent efforts have focused on constructing and testing a localized induction heating apparatus for fabricating tube-to-tube joints. It has been demonstrated that microstructurally sound tube-to-tube joints can be produced; further research is needed to evaluate the properties of joined tubular components, and to scale up the process to allow larger diameter and longer length tubes to be handled. Technology transfer activities involving industry are discussed.

INTRODUCTION

SiC ceramics have considerable potential as elevated temperature structural materials in fossil energy applications. Ceramic-to-ceramic joining methods are needed to allow the fabrication of large or complex shaped parts, and ceramic-to-metal joining methods are needed to allow integration of ceramic components into existing engineering systems. Although considerable efforts have been devoted to understanding the processing, microstructures and properties of SiC-based structural materials, joining remains largely an unresolved issue, particularly with respect to elevated temperature applications. Ideally, joined components should exhibit mechanical properties (including reliability), elevated temperature capabilities and environmental resistance comparable to the base material. Furthermore, the joining method should be practical, cost effective and applicable to different types of SiC ceramics, including SiC fiber-reinforced composites.

This project has successfully developed a reaction processing method for fabricating SiC ceramic-to-ceramic joints [1,2]. The processing method involves tape casting thin sheet SiC+C interlayer precursors, clamping the tape between the SiC parts, and infiltrating the joint with molten Si to form a reaction bonded silicon carbide (RBSC) joint interlayer. This method is attractive since the interlayer material is compatible with

SiC, and excellent room and elevated temperature mechanical properties can be achieved. In addition, as with brazing, external pressure is not required, thus making the process inexpensive and practical compared to alternative joining methods. Recent research has aimed to extend the laboratory joining method to more practical component geometries relevant to fossil energy systems, notably SiC tubes for heat exchanger applications. Efforts have also been made to transfer this joining technology to the private sector.

EXPERIMENTAL

Details of the joining procedure have been described previously [1,2]; therefore, the processing methods are only be summarized here. Joining studies have been conducted using pressureless sintered α-SiC (Hexalloy SA, The Carborundum Company, Niagara Falls, NY). After cleaning the mating surfaces, a thin layer of SiC+C powders, in the form of a tape-cast green sheet, was placed and held firmly between the parts to be joined. In the case of small test bars, a simple graphite fixture was used for holding the parts together and joining was conducted in a tube furnace. In the case of tube-to-tube joints, a special apparatus consisting of a hydraulic press and an induction heater was used; the details of this equipment will be presented later. In either case, a small piece of silicon was placed near the joint, the assembly was heated at ~20°C min^{-1} under flowing argon to ~1450°C, and the temperature was held for 30 min to allow infiltration and reaction bonding to occur.

After joining, specimens were sectioned and polished for microscopic examination. Standard bend bars having dimensions of 3 x 4 x 50 mm were prepared by surface grinding. The edges were beveled, and the surfaces were polished to a 12 μm finish. Strength and fracture toughness were measured in four-point bending with spans of 20 and 40 mm using a crosshead speed of 0.13 mm min^{-1}. Fracture toughness was determined using the single-edge notched beam (SENB) method [3] in which a 0.16 mm wide x 1.0 mm deep notch was cut into the joint region with a high speed saw. Elevated temperature tests were performed in air. Specimens were heated to the desired temperature at a rate of ~20°C min^{-1}, and held for 10 min prior to testing. A minimum of 8 specimens were tested for each condition; the average and standard deviations were determined.

RESULTS AND DISCUSSION

Bulk commercial RBSC is produced by capillary infiltration of molten silicon into compacts containing SiC and C. The processing, microstructures, and properties of these materials have been studied extensively [4-7]. Typical materials are near full density composites consisting of 85 to 90 vol% of SiC and 5 to 15 vol% of free Si. The joint interlayers fabricated in this work exhibited similar microstructures, as shown in Figure 1. The joint interlayer thickness was approximately the same as the thickness of the starting tape, about 150 μm in the case of the joint in Figure 1. Complete infiltration of the interlayer usually occurred, and in most cases the interlayer material exhibited fewer and smaller defects than what was typically observed in the SiC.

The tape casting method offers several advantages for fabricating joining precursor materials from powder mixtures. This approach allows the production of high quality, uniform and controlled thickness tapes, thus providing a simple means for adjusting joint interlayer thickness. Once formed, the tapes can be stored indefinitely and are easy to handle. Furthermore, because the tapes are flexible, they can be cut into various shapes and molded to allow the joining of curved surfaces and complex-shaped parts. Thus, for tube-to-tube joints of the butt geometry the tapes were cut into the shape of a ring to match the tube end surfaces.

Joint Properties

The results of mechanical property measurements have been reported previously. Room temperature strength averaged 327 MPa, comparable to the strength reported in the literature for bulk pressureless sintered α-SiC [8-12]. The strength remained relatively constant for testing temperatures up to 1200°C, and at 1400°C the strength decreased to an average of 208 MPa. The reduction in strength at this temperature is characteristic of RBSC [13]. The decrease in strength occurs as the Si phase approaches its melting point (i.e. 1412°C). Near and above the melting point of Si the RBSC materials can still retain some strength as a result of the continuous network of SiC grains within the microstructure. Failure probabilities calculated using the Weibull distribution were also shown to be comparable to values reported in the literature for bulk pressureless sintered α-SiC [12]. In almost all cases, fracture occurred either within the joint interlayer or within the α-SiC adjacent to the joint; few interface failures were observed.

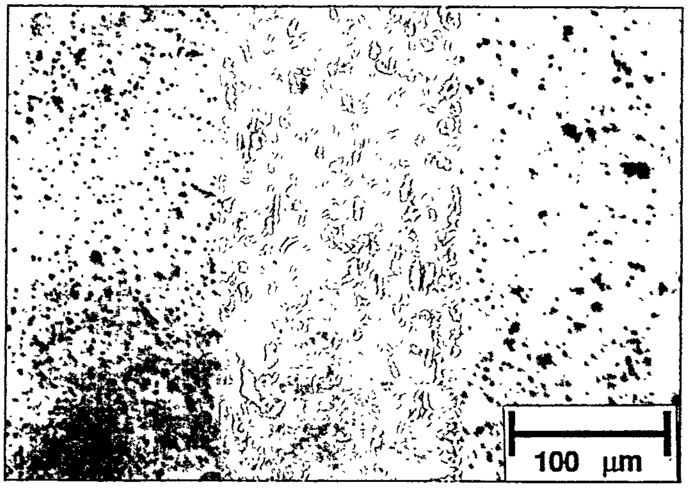

Figure 1. Typical microstructure of a SiC-to-SiC joint bonded with a RBSC interlayer fabricated by Si infiltration of SiC+C tape cast precursors.

Fracture toughness measurements made using SENB specimens tested in four-point bending showed an average room temperature K_{Ic} of 2.8 MPa•m$^{1/2}$. This value is similar to the toughness values reported in the literature for bulk SiC [10,14-16]. The joint toughness remained constant at 600°C, but increased significantly at higher testing temperatures. The effective K_{Ic} values calculated for the 1200 and 1400°C tests were ~7 MPa•m$^{1/2}$. This behavior can be explained based on the presence of free Si in the joints. The compressive flow stress of Si is known to decrease markedly above ~800°C, allowing for increased plasticity and crack-tip blunting at higher testing temperatures [17].

In both strength and fracture toughness tests, particularly at low temperatures, failures were frequently observed to occur entirely within the base ceramic adjacent to the joint as a result of the larger defects present within the pressureless sintered material. At higher temperatures failure more frequently occurred within the joint interlayer and the strength and toughness were controlled by the properties of the RBSC interlayer. The potential exists to improve the elevated temperature joint properties by altering the RBSC microstructure, for example by infiltrating with alloyed Si-Mo melts to produce reaction bonded SiC-$MoSi_2$ composite interlayers that exhibit superior elevated temperature capabilities [18].

Additional mechanical properties studies are planned to examine the long term stability of joints under simulated fossil energy service conditions. These studies will likely be conducted in collaboration with industrial participants.

Tube-to-Tube Joining

The apparatus that has been constructed and used to prepare the SiC tube-to-tube joints is shown in Figure 2. It consists of an insulated chamber equipped with an inert gas purge, an induction heating coil and susceptor used to locally heat the joint region, an hydraulic press for applying the necessary force to hold the joint assembly firmly clamped together, and an optical pyrometer for controlling temperature. Figure 2 shows the apparatus fully loaded prior to a joining experiment. Figure 3 is a photograph of a joint produced between two 2.5" OD x 6" long SiC tubes. After joining, the joint region was sectioned and examined metallographically and the microstructure was found to be identical to that shown in Figure 1. Experiments are in progress to improve the atmosphere and temperature control of this apparatus, and a new apparatus is being designed that will allow larger diameter and longer tubes to be joined. Future mechanical properties studies will also examine the behavior of joined tubular structures under elevated temperature and high pressure conditions expected in heat exchanger applications.

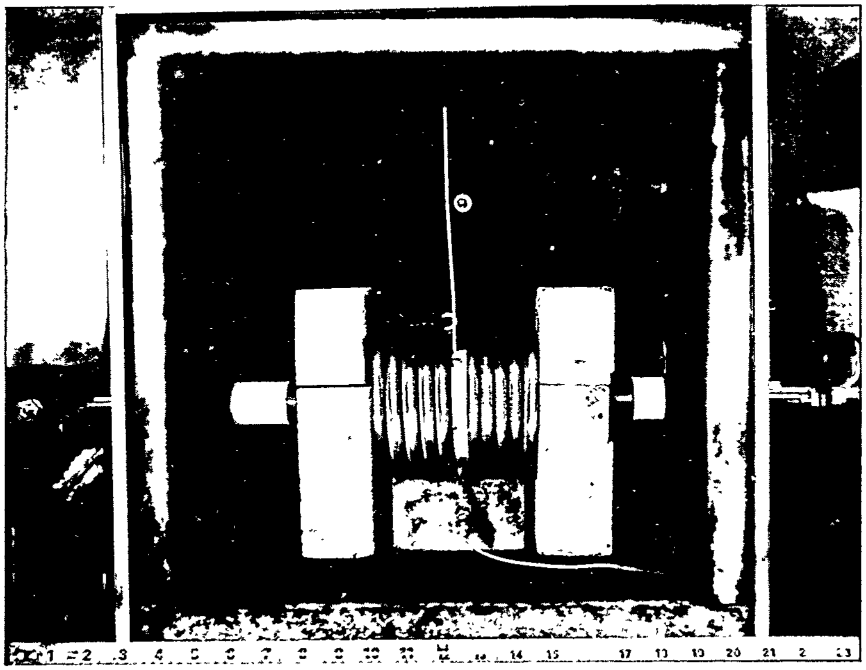

Figure 2. Photograph of the localized induction heating apparatus used to fabricate SiC tube-to-tube joints. See text for description.

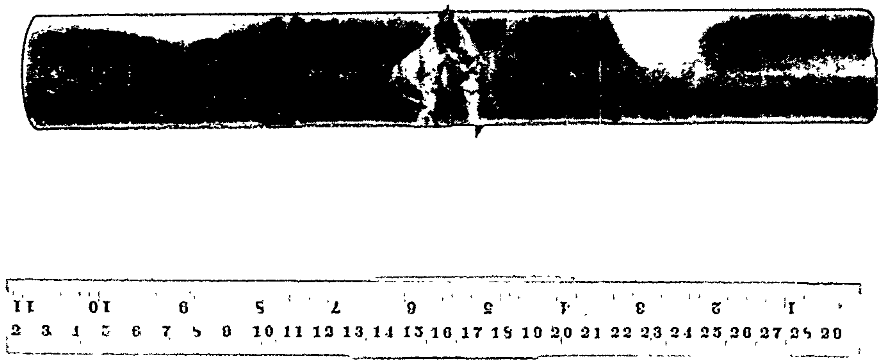

Figure 3. Photograph showing tube-to-tube joint between two 2.5" OD x 6" long SiC Tubes.

Technology Transfer Activities

Numerous industry contacts were made in the past year and detailed discussions were held regarding industrial needs for SiC joining as related to fossil energy applications. As a result of these discussions, several technology transfer activities are now in progress. In one area, a joint work statement has been agreed upon with DuPont/Lanxide to develop joining techniques for their CVI SiC/SiC composite materials being developed under support from the DOE Continuous Fiber Ceramic Composites (CFCC) Program. Planned research includes laboratory joining of composite specimens of several geometries, investigation of various joint configurations (i.e. butt vs. lap), microstructure and property assessments, and composite tube-to-tube joint development and evaluation. Additional support for the INEL contribution to this technology transfer effort is being sought through the CFCC Program.

In a second effort, a Cooperative Research and Development Agreement (CRADA) is currently being negotiated with Allied Signal Aerospace Corp., a subcontractor to Foster Wheeler Development Corp., to investigate the use of the INEL joining techniques in the development of the Ceramic Air Heater for the DOE High Temperature Advanced Furnace. This research also includes laboratory joining studies that will be followed by demonstration and high temperature pressure testing of tube-to-tube joints.

SUMMARY

Reaction processing methods have been described for fabricating SiC-to-SiC joints for potential use at elevated temperatures. The strength and fracture toughness of joined specimens were found to be controlled primarily by the properties of the RBSC interlayer. The joining technique has been extended to fabricate SiC tube-to-tube joints. Technology transfer activities are in progress.

REFERENCES

1. B. H. Rabin and G. A. Moore, "Joining of SiC Ceramics and SiC/SiC Composites," ORNL/FMP-93/1, Oak Ridge National Laboratory, July 1993, pp. 33-42.

2. B. H. Rabin and G. A. Moore, "Reaction Processing and Properties of SiC-to-SiC Joints," Mat. Res. Soc. Symp. Proc., Vol. 314, 1993, pp. 197-203.

3. J. E. Srawley and B. Gross, in ASTM STP601, J. L. Swedlow and M. L. Williams (ed.), ASTM, Philidelphia, 1976, pp. 559.

4. P. Popper, "The Preparation of Dense Self-Bonded Silicon Carbide," in Special Ceramics, Heywood & Company, London, 1960, pp. 209-219.

5. C. W. Forrest, P. Kennedy and J. V. Shennan, "The Fabrciation and Properties of Self-Bonded Silicon Carbide Bodies," in Special Ceramics 5, P. Popper (ed.), British Ceramic Research Association, Stoke-on-Trent, 1972, pp. 99-123.

6. G. R. Sawyer and T. F. Page, "Microstructural Characterization of "REFEL" (Reaction-Bonded) Silicon Carbides," *J. Mater. Sci.*, **13**, 1978, pp. 885-904.

7. J. N. Ness and T. F. Page, "Microstructural Evolution in Reaction-Bonded Silicon Carbide," *J. Mater. Sci.*, **21**(4), 1986, pp. 1377-1397.

8. S. Dutta, "Sinterability, Strength and Oxidation Resistance of Alpha Silicon Carbide Powders," *J. Mater. Sci.*, **19**, 1984, pp. 1307-1313.

9. R. K. Govila, "Phenomenology of Fracture in Sintered Alpha Silicon Carbide," *J. Mater. Sci.*, **19**, 1984, pp. 2111-2120.

10. A. K. Ghosh, *et al.*, "Elevated-Temperature Fracture Resistance of a Sintered α-Silicon Carbide," *J. Amer. Ceram. Soc.*, **72**(2), 1989, pp. 242-247.

11. S. G. Seshadri, M. Srinivasan and K. Y. Chia, "Microstructure and Mechanical Properties of Pressureless Sintered α-SiC," in Ceramic Transactions, Vol. 2: Silicon Carbide '87, J. D. Cawley and C. E. Semler (ed.), The American Ceramic Society, Westerville, OH, 1989, pp. 215-226.

12. A. Charif and F. Osterstock, "On the Fracture Statistics of Polycrystalline α-SiC at Room Temperature," *Mater. Sci. Eng.*, **B11**, 1992, pp. 299-302.

13. G. C. Trantina and R. L. Mehan, "High-Temperature Time-Dependent Strength of an Si/SIC Composite," *J. Amer. Ceram. Soc.*, **60**(3-4), 1977, pp. 177-178.

14. A. G. Evans and F. F. Lange, "Crack Propagation and Fracture in Silicon Carbide," *J. Mater. Sci.*, **10**, 1975, pp. 1659-1664.

15. K. D. McHenry and R. E. Tressler, "Frature Toughness and High-Temperature Slow Crack Growth in SiC," *J. Amer. Ceram. Soc.*, **63**(3-4), 1980, pp. 152-156.

16. I. Merkel and U. Messerschmidt, "Fracture Toughness of Sintered SiC Ceramics: A Comparison Between Different Methods," *Mater. Sci. Eng.*, **A151**, 1992, pp. 131-135.

17. M. Brede, "The Ductile-to-Brittle Transition in Silicon," *Acta Metall. Mater.*, **41**(1), 1993, pp. 211-228.

18. R. P. Messner and Y.-M. Chang, "Liquid-Phase Reaction-Bonding of Silicon Carbide Using Alloyed Silicon-Molybdenum Melts," *J. Amer. Ceram. Soc.*, **73**(5), 1990, pp. 1193-1200.

DENSIFICATION OF NANO-SIZE POWDERS

Wei Chen, Subhas G. Malghan, Stanley J. Dapkunas, Gasper Piermarini and Stephen C. Danforth[1]

Ceramics Division
National Institute of Standards and Technology

ABSTRACT

Green compacts from a nano-size silicon nitride powder were fabricated having density up to 67% of theoretical at 2.8 GPa pressure using liquid nitrogen and pentane as compaction lubricant media. Pressureless sintering of these transparent samples did not promote further densification beyond that obtained for the green state. To further increase the density of these samples, a hot-pressing device was designed. In a series of experiments, hot-pressing of these samples at 0.5 to 1.0 GPa and 800 °C, followed by pressureless sintering at 1400 °C was studied. The resulting silicon nitride ceramic had a Vickers hardness of 9.0 GPa while transparency under visible light was maintained. Without the use of hot pressing, the hardness obtained was 5.8 GPa. In addition, the effect of compaction pressure on densification was studied for nano-size Al_2O_3 to further understand factors contributing to achieving high green densities. The dense Al_2O_3 green samples were pressureless sintered to near full density at temperatures several hundred degrees lower than those needed for sintering low density green material.

INTRODUCTION

The feasibility of producing nanostructured Si_3N_4 with improved properties, and ultrafine-grained nano-phase transparent Si_3N_4 from amorphous nano-size powders without the use of sintering aids has been investigated in the present work. The approach uses cryogenic compaction of nano-size particles followed by pressureless sintering

---

[1] Rutgers University, Piscataway, NJ.

of the transparent green compact [1]. This new procedure potentially offers (1) improved reliability in manufacturing of ceramic parts because flaws are easily visible owing to the transparent nature of the green state, and (2) a decrease in sintering temperature from approximately 2000 to 1400 °C for fabrication of dense silicon nitrides. Early diamond anvil cell results [1] encouraged us to study the processing of silicon nitride on a larger scale. The approach does not involve the use of sintering aids and slurry processing or hot isostatic pressing (HIPing), which may have the effect of reducing the overall fabrication cost.

Cryogenic or other lubricant compaction techniques were used to produce a dense compact (67 % or higher density at 2.8 GPa) from amorphous nano-size silicon nitride powder. Following this, the dense compact was hot-pressed at pressures from 0.6 to 1 GPa at temperatures up to 800 °C in order to increase contact areas between particles. Finally, the compact was pressureless sintered at 1400 °C. This process is expected to promote a strong bonding at the contact area due to solid-state surface diffusion. The density of the new microstructure of silicon nitride ceramic with nano-scale porosity and grain size is expected to be in the range of 65 - 80 % of theoretical with enhanced optical, electrical, and mechanical properties.

The project also addresses the study of selected nano-scale oxide powders to understand the basic phenomena involved during lubricant-aided compaction of powders to high green density and further densification by sintering. These studies, aided by pore structure analysis using small angle neutron scattering (SANS) and transmission electron microscopy (TEM), were used to develop an improved understanding of limitations to achieving full densification of nano-scale powders. These data may not only help us develop a new class of materials, but also may have far reaching implications in the development of nano-powders processing technology.

OBJECTIVES

The objective of this research is to fabricate transparent Si_3N_4 from nano-size amorphous powders at much lower temperatures than the conventional sintering temperature of approximately 1800-2000 °C without using extrinsic sintering aids. Specifically, the following major steps were planned to accomplish this goal:

- Design and fabrication of computer controlled equipment for investigating the rheology of powder compaction under different lubricating conditions.
- Production of transparent green compact disks, 3 mm in diameter and 0.3-1.0 mm in thickness.
- Optimization of packing density by using cryogenic or other lubricant compaction techniques to obtain the maximum random packing density of about 67% for mono-size particles at pressures up to 2.8 GPa.
- Increase of contact area at particle interfaces by hot-pressing green compacts at 0.6 - 1.0 GPa and 800 °C.
- Pressureless sintering (at 1400 °C) to control surface solid-state diffusion along contact area interfaces.
- Characterization of dense (65-80 % theoretical) ceramic for functional and microstructural properties.

RESULTS

Equipment Design and Development

Compaction Equipment

To study the cryogenic liquid nitrogen or other lubricant compaction process in more detail and for fabricating larger volume samples, we designed and constructed a novel apparatus. This apparatus [2] is capable of producing 3 mm disk-shaped samples under vacuum or in a variety of controlled conditions such as surrounding gaseous or liquid environments and temperatures in the range from liquid nitrogen to room, and pressures up to 3 GPa. In addition, during the compaction procedure, continuous measurements of volume of the sample, applied force, and frictional force between the sample and the die walls are performed.

The equipment is designed for two different modes of operation in the powder compaction experiments: (1) gas lubrication, and (2) liquid lubrication. In the first mode, a small amount of lubricating cover gas is introduced into the environmental chamber under controlled pressure. The introduced gas condenses on the surface of particles and the powder is compacted under dry or semi-dry conditions. An alternative design of the experimental system is to study liquid lubrication-type compaction of powders as shown in Figure 1. Due to the large amount of data accumulated during an experimental run with this system, a real-time computer control of all measurements and experimental procedures is necessary. For more details, the reader is referred to a recent publication [2].

Hot-Pressing Equipment

Experimental results using the above described equipment indicate that phase transformation and grain growth at sintering temperatures above 1400 °C will generate larger scale (about 100 nm according to TEM analysis) porosity. The transformation from amorphous to α-phase causes a volume shrinkage of the original particle which destroys the packing in the green body and produces large-scale porosity. If the size of grain and porosity are controlled in the nano-scale, the sintering temperature could be below 1500 °C.

To avoid phase transformation and grain growth, the new approach to fabricate transparent true nano-phase Si_3N_4 is to hot press the densely-packed green compact before pressureless sintering. The contact area, ΔS divided by the total area S of a single particle, is given by

$$\frac{\Delta S}{S} = \frac{Po}{Hardness}$$

where P_0 is pressure. Therefore, the contact area of particles can be increased by elevating either the hot-pressing temperature to reduce hardness of Si_3N_4 or the hot-pressing pressure. Since the solid-state surface diffusion is much more likely to happen than the volume diffusion at low-temperature, the surface diffusion along contact areas can form a very strong bond between the particles if the contact area is large enough.

To accomplish this, it was necessary to design a special apparatus to generate high temperature and high pressure. This apparatus shown in Figure 1, called the "belt apparatus," was designed and fabricated to carry out hot pressing of Si_3N_4 green compacts. The belt apparatus may be described as a cross between a piston/cylinder device and opposed Bridgman anvils. It combines massive support for the pistons with a central die for the sample. The pressure generation is through the compression of a gasket material in the apparatus.

The belt apparatus has evolved from Bridgman anvils by first incorporating a well in one of the anvils and compressing a pyrophyllite assembly. However, the pressure limit is quickly reached when the pyrophyllite expands to its limiting volume and halts further compression inside the well. A major advance in the design was made with the realization that the shape profile of the "belt system" is that of a frustum of a cone. In this design, for a given vertical compression stroke of the beveled piston, the pyrophyllite gasket material is forced to move toward the end of the cone frustum which has the smaller diameter. Thus considerable compression of the sample may be obtained before the limiting volume of the gasket is reached.

The final step was to double-end the apparatus about a horizontal axis producing a device consisting of two opposed anvils (beveled pistons) compressing a sample restricted in a central die as shown in Figure 1.

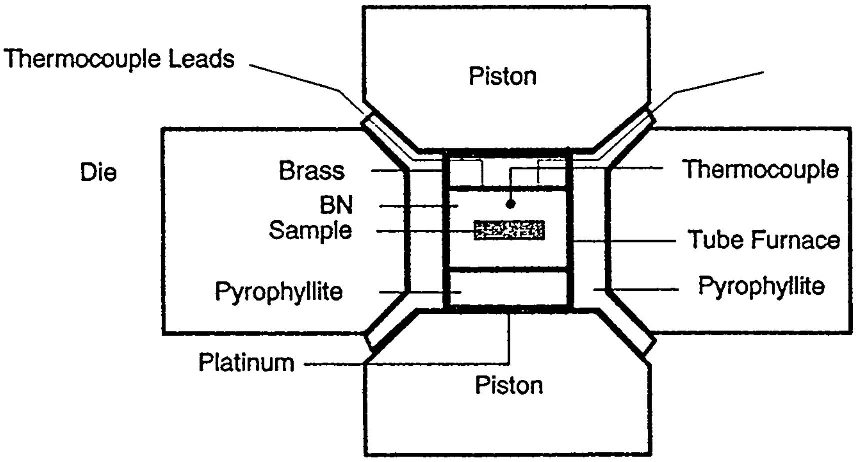

Figure 1. Green density of silicon nitride vs. compaction pressure for a nano-size silicon nitride powder.

The piston and die are constructed from tungsten carbide. The gaskets are usually constructed separately for the upper and lower halves of the apparatus. They consist of two conical pyrophyllite gaskets sandwiching a hollow steel cone. The presence of steel which should be annealed is important since it prevents the thick pyrophyllite gaskets from breaking at low pressures and helps to lower the compressibility of the combination.

The sample is placed at the center of the internal tube furnace (made of graphite), and surrounded with boron nitride packing powder which can provide a homogeneous temperature distribution and isostatic pressure around the sample. To generate high temperature within the tube furnace, a cooling system around the die was needed to prevent heat loss to other components of the system. A power supply with 7.5 V and 200 A is necessary to provide the power needed in this experiment. This high temperature and high pressure device was designed to generate pressures up to 1 GPa and temperatures up to 1000°C.

Experimental Data

Forming densely-packed green compacts from nano-size particles is very difficult. Strong aggregation forces, such as the Van der Waals attraction, increase dramatically as particle size decreases. For nano-size particles, the van der Waals attraction forces can prevent the particles from sliding past each other, and, thereby, promote agglomeration by diffusion across particle contact boundaries during compaction. As a result of aggregation and subsequent agglomeration of primary particles, compacts of nano-size particles usually have low densities after cold pressing. The low density is due to two factors: (1) the presence of large voids in the green-state and (2) inefficient packing of particles in the structure of the green-state. We now know that the use of suitable lubricants can improve the packing properties of the nano-size particles, but, in selecting a lubricant, one is severely limited because of the strongly reacting interface between the particles and the small size of voids in the resulting green microstructure formed by densely-packed nano-size particles.

Figure 2 shows a maximum random packing density of approximately 64% and 57% of theoretical for nano-size amorphous silicon nitride powder compacted at pressure up to 2.5 GPa under liquid nitrogen and with no lubricant, respectively. The density of green Si_3N_4 compact under pentane is about 63 % of theoretical at compaction pressure up to 2.5 GPa. These results indicate that liquid nitrogen and pentane as lubricant media are an efficient technique to reduce compaction pressure to obtain high packing density and small-scale porosity. The green bodies produced by liquid nitrogen and pentane processing exhibit transparency under visible light which is an indication of nano-scale porosity and the existence of homogeneous porosity.

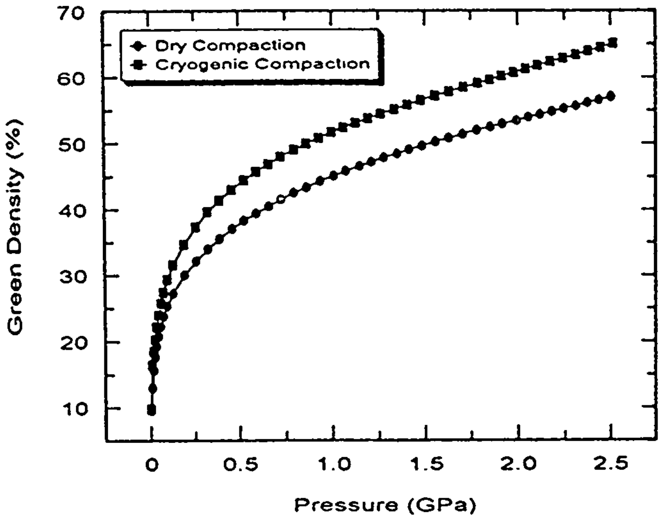

Figure 2. The variation of density of green and sintered compacts of gamma-alumina as a function of sintering temperature and compaction pressure.

The Vickers hardness of the green compacts by dry and cryogenic compaction is shown as Figure 3.

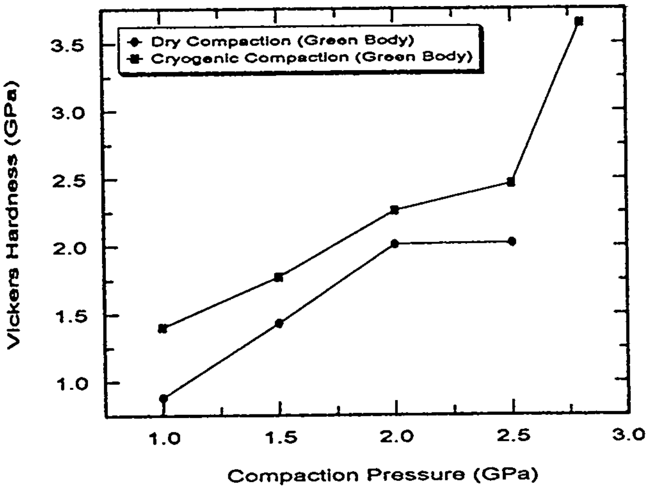

Figure 3. Configuration of a hot-pressing device, called "belt apparatus".

Pressureless Sintering and HIPing

The high density green compacts were studied by pressureless sintering and HIPing to achieve additional densification. The sintering temperature was limited by phase transformation and grain growth at 1400 °C. In one series of tests, the transparent green compacts were sintered without pressure at different temperatures from 1200-1600 °C under flowing nitrogen gas. The transparency was lost at a sintering temperature of about 1500 °C as expected because the phase transformation from amorphous to α-phase is accompanied by shrinkage and grain growth. Shrinkage in atomic distances is expected to result in random shrinkage whereas, grain growth is expected to destroy the orderly porosity existing in the green body. The overall result is an increase in the scale of porosity which was estimated to be on the order of the wavelength of visible light (380nm - 780nm). The XRD, BET, and TEM measurements indicate that the phase transformation and grain growth initiate at approximately 1400 °C. Also, it should be noted that the samples were not densified at this pressureless sintering temperature. The maximum hardness of about 5.8 GPa was obtained at a (green body) compaction pressure of 2.8 GPa and 1400 °C sintering temperature.

In another series of experiments, conventional HIPing at 200 MPa using nitrogen gas as pressure transmission medium was attempted at 1200, 1300, and 1400 °C to further densify the transparent high density green compacts of nano-size Si_3N_4. The samples were embedded in BN, BN+Si_3N_4, or Si_3N_4 as packing powders. In one case, at 1300 °C with BN+Si_3N_4 as packing powders, some densification was observed. The sample was encapsulated in a glass or stainless steel envelop.

Phase transformations from amorphous to α-phase and β-phase for pressureless sintered and HIPed compacts were studied by TEM and XRD. The transformation point for both processing methods is above 1400 °C. In general, no significant densification was observed by HIPing.

In another series of experiments we used a gamma alumina nano-powder to investigate the influence of green density on sintering temperature and densification. These experiments were conducted by compacting the alumina powder at room temperature. The reason for using the alumina powder was the readily available sintering and densification data for this material. Results of these experiments, shown in Figure 4, indicate the following:

a. Low density green compacts cannot be densified at temperatures up to 1000 °C.
b. High density transparent green compacts were sintered to higher than 90% theoretical density at 1000 °C.
c. Higher compaction pressure resulted in a higher green density.

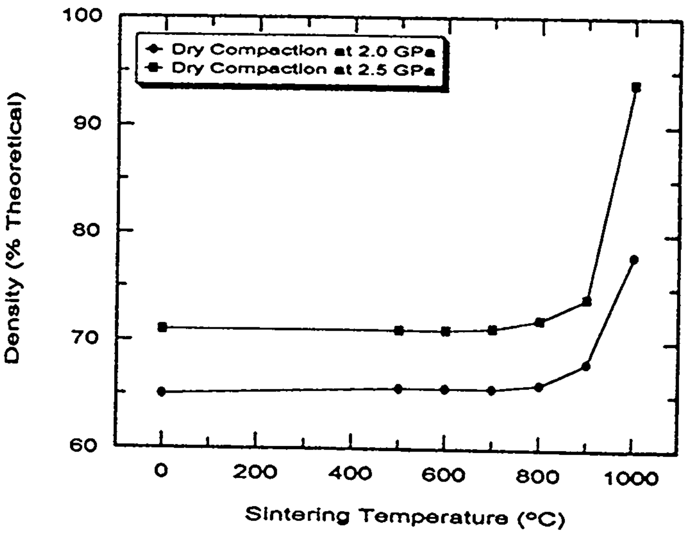

Figure 4. Vickers hardness vs. compaction pressure for green compacts using cryogenic and dry compaction techniques, respectively.

These results demonstrate that one can achieve a high degree of densification at a low sintering temperature of 1000 °C provided that sufficient high green density is achieved during compaction. Thus, the result clearly illustrates that nano-size powders must be compacted to a high density in the green state before further densification is achieved at temperatures lower than the conventional.

Hot-Pressing of High Density Green Compacts

Experiments have been performed to study the densification behavior of silicon nitride using the newly completed hot-pressing device. The primary purpose of these experiments was to investigate the role of hot pressing to improve the mechanical properties of the resulting ceramic. The procedure consisted of the preparation of high density green compacts at 2.8 GPa followed by hot-pressing and pressureless sintering. The pressure and range of temperatures for hot-pressing were 0.6 GPa and 500-800 °C, respectively. Pressures below 0.6 GPa cannot be used because at 0.5 GPa the pressure cell gasket material leaks internal pressure fluid.

Based on results obtained from these tests, the highest Vickers hardness of 9.0 GPa was obtained using the following experimental conditions:

> Pressing of powder at 2.8 GPa using a lubricant
> Hot-pressing at 0.6 GPa and 800 °C
> Pressureless sintering at 1400 °C for five hours

The resulting ceramic is transparent under visible light and shows the presence of a nanophase microstructure. The results are considered to be significant since the hardness has increased to 9.0 GPa from a nominal value of 5.8 GPa. This value, however, is far short of that for a commercial silicon nitride. The Vickers hardness for pressureless sintered compacts only and for hot-pressed and pressureless sintered for different compaction pressures are shown as Figure 5.

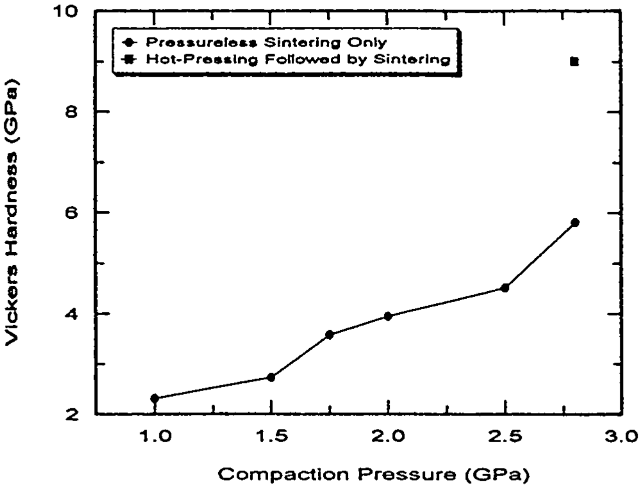

Figure 5. Vickers hardness vs. compaction pressure for hot-pressing at 0.6 GPa and 800 °C followed by pressureless sintering at 1400 °C for 5 hours, and pressureless sintering at 1400 °C for 5 hours only.

CONCLUSIONS

Lubricant-aided compaction has resulted in an improved green density for both silicon nitride and alumina powders. The green densities of these compacts are 6-8% higher than those obtained without the use of lubricants such as liquid nitrogen and pentane. Hot pressing of these green compacts followed by sintering has resulted in an increased hardness of the sintered silicon nitride to 9..0 MPa which is higher than that using low density green compacts. Studies are in progress to identify accompanying microstructural changes.

REFERENCES

1. A. Pechenik, G. Piermarini, and S. C. Danforth, "Fabrication of Transparent Silicon Nitride from Nanosize Particles", J. Am. Ceram. Soc., 75, [12]3283 (1992).

2. W. Chen, A.Pechenik, S. J. Dapkunas, G. J. Piermarini and S. G. Malghan, "Novel Equipment for the Study of the Compaction of Fine Powders", Accepted by J. Am. Ceram. Soc., October 1993.

ACTIVATION AND MICROPORE STRUCTURE DETERMINATION OF CARBON-FIBER COMPOSITE MOLECULAR SIEVES

Frank Derbyshire, You Qing Fei, Marit Jagtoyen,
Geoff Kimber, Mike Matheney and Tim Burchell*

Center for Applied Energy Research
University of Kentucky
3572 Iron Works Pike
Lexington KY 40511-8433
USA

*Oak Ridge National Laboratory, PO Box 2008,
Oak Ridge, TN 37831-6088, USA

INTRODUCTION

Carbon fibers are produced commercially from rayon, phenolics, polyacrylonitrile (PAN), or pitch. The last are further divided into fibers produced from isotropic pitch precursors, and those derived from pitch that has been pretreated to introduce a high concentration of carbonaceous mesophase. Over the past few decades, interest in research and manufacturing carbon fibers has overwhelmingly centered on producing fibers with high tensile strength and high modulus for lightweight, high performance composites, where polymers, metals, and carbon can form the continuous matrix. The fibers most commonly used in advanced materials are produced from PAN or mesophase pitch. Graphitized mesophase pitch fibers tend to have higher modulus and lower tensile strength than the PAN-based equivalents. They have advantages in applications requiring high stiffness, high electrical and thermal conductivity, low thermal expansion, and high temperature oxidation resistance, while PAN fibers are employed where high strength is required.

An impressive volume of research and scientific literature has been amassed on the subject of high performance carbon fibers and composites. However, relatively little attention has been given to the synthesis of lower performance, general purpose fibers that can be produced more cheaply from isotropic pitch precursors. These materials are produced as short, blown fibers (rather than continuous filaments) from precursors such as ethylene cracker tar,[1] coal-tar pitch,[2] and petroleum pitch prepared from decant oils produced by fluidized catalytic cracking.[3] There is a rapidly growing market for these fibers in applications that include: composite friction materials such as brake pads; the reinforcement of engineering plastics; ablation and thermal insulating materials; electrically conductive fillers for polymers; filter media; paper and panels; the production of hybrid yarns with other fibers; and reinforcing concrete to improve flexural strength and other properties.[4,5,6]

More recently still, interest has developed in the activated forms of isotropic carbon fibers, where high surface areas can be produced by partial gasification in steam or other oxidizing gas.[3,7] Activated carbon fibers have novel properties that make them more attractive than conventional forms (powder or large-size carbons) for certain applications.[7] While porosity can be generated in most types of carbon fiber, low-modulus fibers produced from isotropic pitch are particularly suited for activation due to their unique structure in which the random packing of small crystallites allows the development of an extensive pore structure.

Among the possible applications, activated carbon fibers are of interest for the adsorption and recovery of organic vapors; in environmental protection; the removal of SO_x and NO_x from flue gas; the improvement of air quality; and water treatment.[7-12] Difficulties in handling and utilizing activated fibers can be surmounted by their incorporation into composites, such as woven and non-woven fabrics, felt, and paper. This paper describes the development of a rigid activated carbon fiber composite material that can be produced in single pieces to a given size and shape. Because of the potential molecular sieve properties, the composites have been termed activated carbon fiber composite molecular sieves, or CFCMS.

EXPERIMENTAL

A carbon fiber composite material was developed by researchers at the Oak Ridge National Laboratory (ORNL) in the 1980s[13] as a low-density, mechanically strong thermal insulator for a radioisotopic heat source on spacecraft for the Galileo and Ulysses Missions. The material was prepared by vacuum molding from water slurries containing chopped carbonized rayon fibers ($\sim$6.5 μm diameter x $\sim$0.15 mm) and a phenolic resin. The slurry was vacuum molded into tubular or plate configuration, followed by drying, curing, and carbonization to 1600°C. This technique was the forerunner of a procedure that has been subsequently used to produce high surface area carbon fiber composites. The process is currently the subject of a patent application, and details of the composite-forming method and activation procedure cannot yet be disclosed. However, in the following section, some of the characteristics and properties of activated composites formed from isotropic petroleum pitch fibers and activated in steam will be discussed. Specimens have, to date, been activated as plates of dimensions of 1.5x4x12 cm and tubes of length 10 cm, inner diameter 3 cm, and wall thickness 0.5 cm.

RESULTS AND DISCUSSION

Activated carbon fibers produced from isotropic petroleum pitch have been reported to develop surface areas up to 2000 m^2g^{-1}, with almost all of the pore volume present in micropores (< 2nm diameter pores)[3,14]. These properties are retained by the composites, as illustrated in Figure 1, where the nitrogen BET surface area is shown as a function of burn-off. It can be seen that high surface areas can be attained at moderate burn-off.

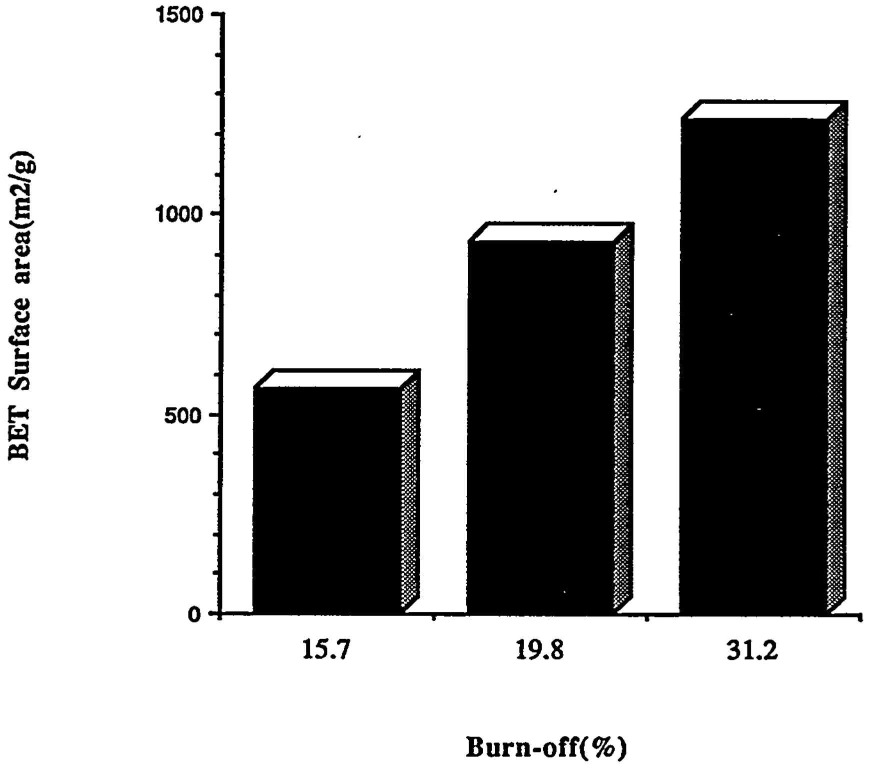

Figure 1. Development of surface area in CFCMS at different burn-offs.

The pore size distribution is narrow, although it broadens with increasing activation: the average pore width increases from 0.58 to 0.83 nm as the burn-off increases from 16 to 31% (Figure 2). The sample at 16% burn-off has the narrowest pore size distribution with almost all pores less than 6 nm in diameter, while the more activated samples have significant proportions of pores from 6-8 nm in diameter. Depending on the application, a compromise may be required between pore size distribution and total surface area.

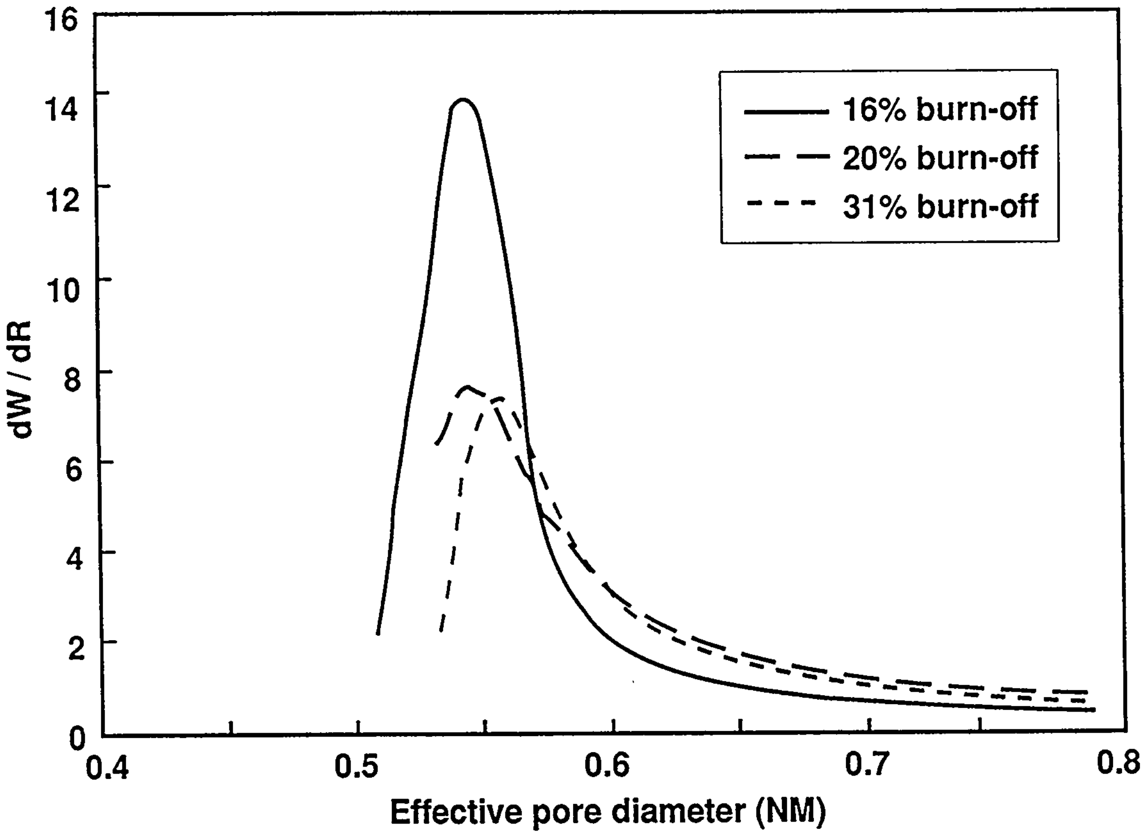

Figure 2. Pore size distribution of CFCMS at different burn-offs.

Examination of the activated composites by scanning electron microscopy reveals an open structure that allows the free flow of fluid while providing a high internal surface for adsorption. Measurements have shown that for a composite thickness of 15mm, an air flow of 15 l/min through a disc of diameter 25mm (i.e. $30m^3$/min per m^2) generates a pressure differential less than 20 kNm^{-2}. This permeability is comparable to that of a bed of 2mm sized granules, and much higher than for a bed of 14 micron sized powder. Because of the open architecture of the composite, the fibers within are almost as accessible as free fibers. While the rate of activation of the composite (fibers *and* binder) is about 70% of that determined for a collection of individual fibers, the rate of adsorption on the activated forms has been found to be similar, and much higher than for granular carbons, due to the essential absence of diffusion limitations, as illustrated for the adsorption of NO measured by thermogravimetry (Figure 3). Only when granular carbons (commercial coconut shell product) are reduced to a comparable particle size (av diam 14 microns vs 12-15 microns fiber diameter) do the rates begin to correspond.

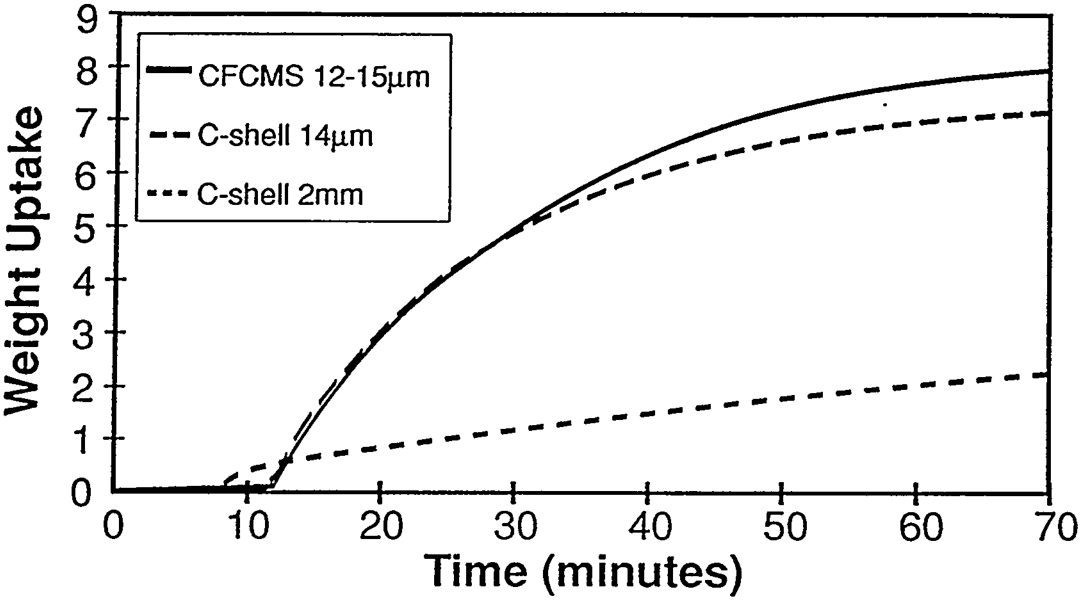

Figure 3. Influence of particle diameter on the adsorption of NO on particulate activated carbons and activated composites (28°C, no O_2 present).

In spite of their open structure, the composites are strong, as indicated by crush strength determinations, and there is appreciable retention of strength with burn-off during activation (Figure 4).

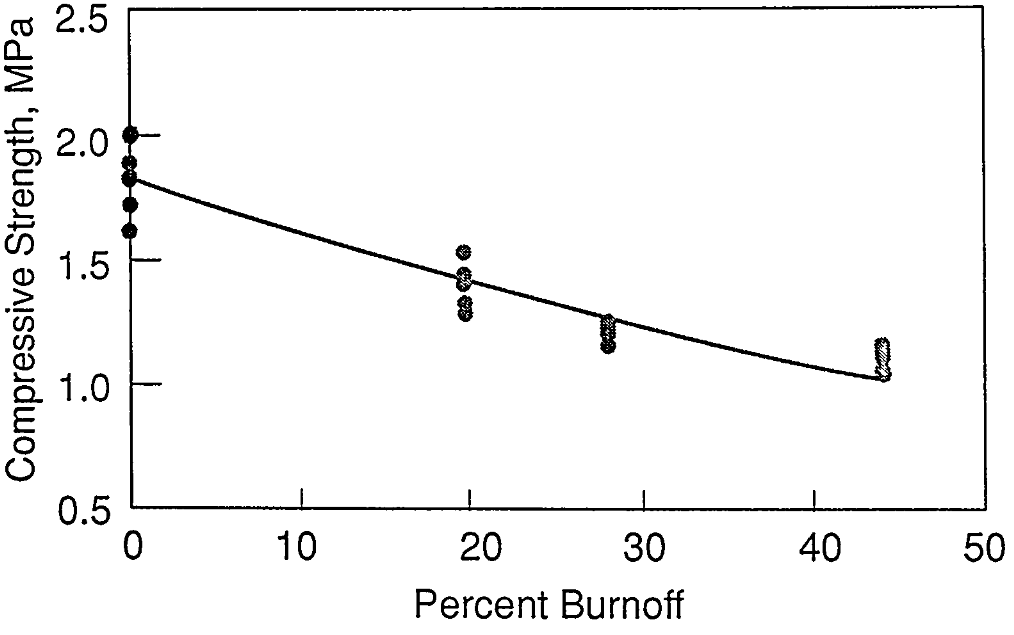

Figure 4. Crush strength of carbon fiber composites at different levels of burn-off.

The unique properties of the activated composites - narrow, unimodal pore structure, high surface area, rapid rates of adsorption and desorption, the ability to form specific shapes with high permeability and strength - suggest that, among other applications, notably in environmental protection, they may be suitable for molecular separation on the basis of size and shape. For this reason, preliminary experiments have been conducted to examine the separation of gas mixtures. The system CH_4-CO_2 was selected as the initial model. The adsorption of the individual gases on activated CFCMS was investigated by TGA, and showed that CO_2 is preferentially adsorbed. Subsequent experiments were made to determine the effective separation that can be attained.

A 75%/25% CH_4/CO_2 mixture was passed through a sample of activated CFCMS and the composition and flow rate of the emergent gases were determined as a function of time using a mass spectrometer and a mass flow meter, respectively. Breakthrough plots (Figure 5) clearly show that CO_2 is preferentially retained on the carbon, and that the separation can be improved by modifying the composite structure.

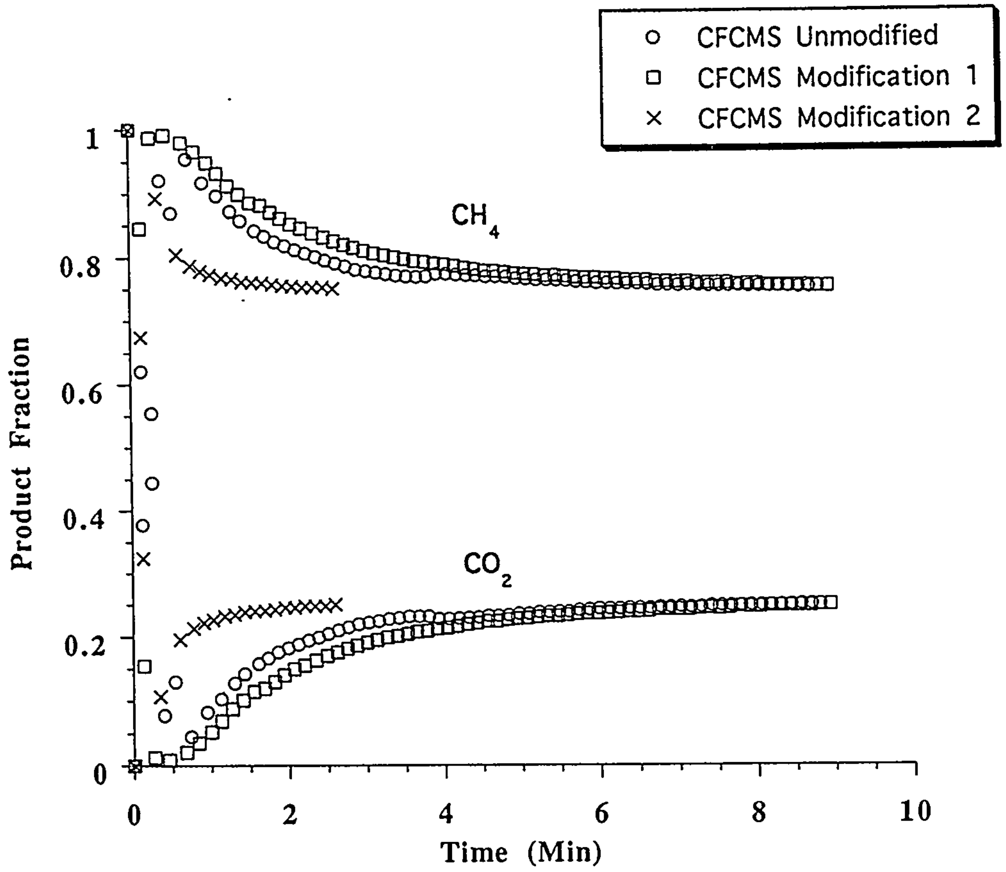

Figure 5. Separation of CO_2 and CH_4 through CFCMS at atmospheric pressure, 25°C. (Initial composition 75 vol% CH_4 and 25 vol% CO_2).

REFERENCES

1. K. Okuda, *Petrotech*, **5**(1), 37 (1982).
2. Y. Matsumura, *Seikiyu Gakaishi*, **30**(5), 291 (1987).
3. M. W. Thwaites, M. L. Stewart, B. E. McNeese, and M. Sumner, *Fuel Proc. Tech.*, **34**, 137-145 (1993).
4. K. Okuda, *TANSO*, **155**, 426 (1992).
5. P. Soroushian, F. Aouadi and M. Nagi, *ACI Materials Journal*, **88**, No. 1, p. 11-18 (1991).
6. F. Derbyshire, M. Jagtoyen, Y. Q. Fei and G. Kimber, *Am. Chem. Soc., Div. Fuel Chem. Preprint*, **39**(1), 113-120 (1994).
7. M. Suzuki, Proc. Biennial Carbon Conference, Buffalo (1993).
8. I. Mochida, Y-N. Sun, H. Fijitsu, S. Kisamori, and S. Kawano, Nippon Kagaku Kaishi (J. Chemical Society of Japan), **6**, 885-890 (1991).
9. I. Mochida, T. Hirayama, S. Kisamori, S. Kawano, and H. Fijitsu, *Langmuir*, **8**(9), 2290-94 (1992).
10. K. L. Foster, R. G. Fuerman, J. Economy, S. M. Larson, and M. J. Rood, *Chem. Mater.*, **4**, 1068-1073 (1992).
11. J. Economy, K. Foster, A. Andreopoulos, and H. Jung, *Chemtech*, 597-603, October (1992).
12. M. Suzuki, *Water Science Technology*, **23**, 1649 (1991).
13. G. C. Wei, and J. M. Robbins, *Ceramic Bull.*, **64** (5), 691-699 (1985).
14. Y. Q. Fei, F. Derbyshire, M. Jagtoyen and I. Mochida, Eastern Oil Shale Symposium, Lexington, KY, USA, 17-19 November (1993).

Ceramic Catalyst Materials

A. G. Sault and T. J. Gardner
Sandia National Laboratories
Albuquerque, NM 87185

S. Srinivasan, A. Hanprasopwattanna and A. K. Datye
University of New Mexico
Albuquerque, NM 87131

ABSTRACT

Hydrous titanium oxide (HTO) ion-exchange materials show great potential as ceramic catalyst supports due to an inherently high ion-exchange capacity which allows facile loading of catalytically active transition metal ions, and an ability to be cast as thin films on virtually any substrate. While earlier work delineated optimum ion-exchange and activation procedures for noble metal catalysts supported on bulk HTO materials, current efforts focus on understanding and controlling HTO thin film formation on porous, high surface area substrates. The ability to tailor thin film properties offers a number of important advantages for catalytic applications. First, the use of a cheap, high surface area material as a substrate for HTO films improves the economics of HTO supported catalysts, as bulk HTO materials are substantially more expensive than conventional catalyst supports. Second, HTO thin film technology offers a convenient method for separately engineering the chemical (ion-exchange, activation, activity, *etc.*) and mechanical (porosity, pore size, surface area, mechanical strength, *etc.*) properties of catalytic materials. In order to take full advantage of HTO thin film technology, methods must be developed for forming continuous multilayer HTO films on high surface area substrates. We are addressing this problem by varying the properties of the sol-gel precursors used to form HTO films, and by altering HTO film deposition procedures. The effects of changes in film formation techniques on film properties are being investigated using transmission electron microscopy and isopropanol dehydration as a specific surface area probe. In order to assess the effects of changes in film properties on catalytic properties, ion-exchange and catalytic activity measurements are being made for a variety of catalytic reactions, including hydrogenation, hydrogenolysis (cracking) and upgrading of coal liquids. Results from earlier studies of bulk HTO supported catalysts are guiding the studies of thin film HTO supported catalysts.

INTRODUCTION

The economical direct conversion of coal into liquid transportation fuels relies heavily on the development of improved catalyst materials with greater activity and longer lifetimes than currently available catalysts. Current state-of-the-art coal liquefaction catalysts, consisting of sulfided NiMo particles supported on an alumina substrate, are derived from catalysts developed for upgrading of resid and heavy crude. Unfortunately, the activity and lifetime of these catalysts under typical direct liquefaction conditions are inadequate for economical coal conversion. The development of new catalyst technologies for direct liquefaction is therefore necessary to allow efficient utilization of coal, the most abundant fossil energy source in the United States, as a transportation fuel.

One promising new technology involves ceramic catalyst support materials known as hydrous metal oxide (HMO) ion-exchangers. These materials are formed by the reaction of a metal alkoxide (typically titanium tetraisopropoxide (TTIP), although alkoxides of zirconium, niobium and tantalum can also be used) with a solution of NaOH in a suitable solvent (*e.g.*, methanol or toluene), followed by hydrolysis with an acetone/water mixture.[1] For hydrous titanium oxide (HTO), the resulting amorphous powders have surface areas on the order of 300 m^2/g, and contain as many as one sodium ion for every two titanium atoms. These sodium ions can be quantitatively exchanged for metal cations in aqueous solution, providing a simple and effective method for preparing supported metal catalysts. With proper control of ion-exchange conditions, high metal loadings can be achieved with essentially atomic dispersion.[2,3] Experimental sulfided NiMo/HMO catalysts exhibit activities for reactions relevant to coal liquefaction exceeding those of currently available commercial catalysts.[1]

Because of raw material costs, the synthesis of bulk HTO materials is prohibitively expensive, making the use of bulk HTO materials uneconomical. The successful application of HMO materials therefore requires the development of catalysts based on thin HMO films deposited on a suitable inexpensive, high surface area substrate. The alkoxide/NaOH/solvent precursor solutions used to make bulk HMO materials can also form thin HMO film an a wide variety of substrates by dip coating in the presence of added or atmospheric moisture. The thin film forms present two important advantages over bulk forms. First, by coating an inexpensive, high surface area substrate, such as silica or alumina, the total amount of alkoxide required to achieve a given surface area is greatly reduced, thereby lowering catalyst manufacturing costs and improving the economic outlook for application of HTO materials. Second, thin film forms allow the catalytic and mechanical properties of the final catalyst formulation to be separately engineered. The HTO film properties determine catalytic behavior, while the substrate properties determine mechanical strength, surface area, and porosity. Although thin film HTO catalysts have been explored and shown to have superior properties compared to bulk HTO materials, no systematic study of the variables affecting HTO thin film properties has been performed. It is the purpose of this program to explore variables such as precursor identity and concentration, solvent identity, deposition methods, substrate properties, and water addition on the coverage and thickness of HTO films on porous substrates. By proper manipulation of these variables, we hope to gain precise control over substrate coverage and film thickness. The approach to this problem involves development of analytical techniques to determine titania coverage on various substrates, comparison of titania and HTO film growth, use of model substrates such as nonporous spheres to facilitate film characterization, and model catalytic reactions to determine the catalytic behavior of thin film HTO catalysts in comparison with bulk HTO catalysts. In addition to applications as coal liquefaction catalysts, the development of improved HTO thin film technology enables the generic application of HTO materials to a numerous catalytic applications, including hydrogenation, hydrogenolysis (cracking), and automotive catalysis.

DISCUSSION OF CURRENT ACTIVITIES

HTO Thin Film Formation and Characterization

Because the formation of HTO films is more complicated than formation of titania films, initial studies focused on the deposition of titania films. Results from the titania films were then used to develop techniques for depositing HTO films. Also, since films on porous substrates are more difficult to characterize than films on nonporous substrates, initial experiments dealt with nonporous silica Stöber spheres approximately 200 nm in diameter. The absence of porosity in these spheres greatly simplifies analysis by transmission electron microscopy (TEM) since the coating resides entirely on the exposed surface of the spheres. Also, measurement of titania surface area using rates of isopropanol dehydration[4] is simplified on the spheres since diffusion limitations within pores need not be considered. To date only silica substrates have been studied even though alumina is a more promising substrate for the severe environments encountered in liquefaction. The choice of silica is dictated by the availability of a specific surface area probe which can distinguish between silica and titania surface area, although selective probes which can distinguish between titania and alumina surface area are under development. As described in a previous annual report[5] the rate of isopropanol dehydration can be used as a measure of titania surface area. Thus, by measuring isopropanol dehydration rates on bulk titania and HTO materials, and normalizing the rates to the BET surface area, specific rates can be calculated. Since this reaction occurs selectively on titania but not on silica, these specific rates are then used to convert dehydration rates measured on silica supported thin films into titania surface areas. By comparing the specific surface areas to the total BET surface area of the substrate, coverage of the substrate by the films can be calculated. Coupled with TEM measurements of film morphology and structure, the dehydration data allows the properties of the films to be evaluated in a quantitative manner.

Titania and HTO films on silica spheres

Monolayer titania films can be formed by reaction of titanium *tert*-butoxide (TBOT) with hydroxyl groups on the surface of silica Stöber spheres in the absence of water, followed by heating in helium at 773K to decompose the precursor and form TiO_2. These monolayer films exhibit isopropanol dehydration rates consistent with complete coverage of the silica surface with titania.[4] TEM images of the coated spheres show no visible film, yet energy dispersive X-ray analysis shows that titania is uniformly distributed throughout the sample. Taken together, these results clearly indicate the formation of a monolayer film of titania on the surface of the silica spheres. By proper addition of water and adjustment of reaction conditions, multilayer titania films can be formed which are clearly visible by TEM. These films are very uniform and smooth and isopropanol dehydration rate measurements are underway to determine the surface area of these films.

HTO monolayer films can also be formed by allowing the TTIP/NaOH/MeOH HTO precursor solution to contact the silica spheres for short times, *e.g.* by dispersing the spheres on a filter paper and filtering the solution through the spheres in the absence of water. The incorporation of sodium into these films has been demonstrated by the ability of the monolayer films to incorporate rhodium by ion-exchange under conditions which result in two orders of magnitude less uptake on the uncoated silica spheres. Thus, true HTO films are being formed, and not merely titania films containing no sodium ions. TEM indicates that the HTO films are much rougher than the titania films. Attempts to produce multilayer HTO films by controlled addition of water to the precursor solution and variation of the deposition procedure have not yet been successful. The presence of NaOH in the precursor appears to accelerate the rate of hydrolysis and condensation of the titanium alkoxide such that film formation is accompanied by precipitation of HTO clusters which are not attached to the silica spheres. Best efforts to date have formed extremely rough films which may be the result of physical adsorption of precipitated HTO clusters on the surface of the spheres rather than true film formation. Additional efforts are underway to understand and control the rate of hydrolysis and condensation of the HTO materials in order to allow formation of uniform, multilayer HTO films. The successful development of multilayer HTO film technology would enhance the applicability of HTO films by increasing the number of ion-exchangeable sodium ions present per unit area of the substrate.

Titania and HTO films on porous silica gels

The formation and characterization of titania and HTO films on porous substrates presents greater challenges than on nonporous substrates. In addition to complications in TEM image interpretation and possible diffusion limitations during isopropanol dehydration, film formation itself is more complex since the pore structure can limit access of the alkoxide precursors to silica surfaces within the pores. Titania film formation was investigated on four different silicas with BET surface areas ranging from 100 to 250 m^2/g and median pore sizes ranging from 75 to 273 Å. One gram of each silica was dispersed in 250 ml ethanol and 1 ml of TBOT was then added. After refluxing for 2 h the mixtures were filtered and dried. Treatment at 300-400°C in helium was performed to convert the precursor into TiO_2 prior to measurement of isopropanol dehydration rates. The coverage of titania, determined by comparison of the dehydration rates with that of Degussa P-25, varied from 0.13% to 5%, with no obvious correlation with either surface area or pore size. Thus, either the reflux time was not long enough, or the surface hydroxyl concentration on these silicas are much lower than on the Stöber spheres.

In an attempt to increase the coverage of the silicas by titania, the addition of water to the reaction mixture was explored. We explored various methods of contacting the water with the silica to optimize titania dispersion. These methods included addition of water to the silica followed by mixing with the precursor solution, or alternatively addition of water to the precursor solution followed by addition of silica. In order to facilitate comparison of the different methods, a single silica with a surface area of 159 m^2/g and a median pore diameter of 273 Å was the substrate for all of the films. Pretreatment at 400°C overnight in He to convert the precursor into TiO_2 was used for all samples prior to measurement of dehydration activity. Titania surface areas ranging from 38 to 168 m^2/g are formed depending on the specific loading procedure used. These surface areas correspond to coverages of 24 to 106 % of the silica surface. TEM images of these films as prepared are not noticeably different from the uncoated silicas, indicating uniform film formation without large agglomerates or surface roughness. During pretreatment or isopropanol dehydration, however, the morphology of the films can change depending on the deposition method and the titania loading. This effect is currently under study. Attempts are now underway to coat high surface area silicas with HTO films. As with the Stöber spheres, it is anticipated that the presence of NaOH in the precursor solutions will adversely affect the HTO film formation resulting in a need to strictly control the coating method in order to obtain high quality, uniform films

Catalytic Activity of Bulk Rh/HTO Catalysts

Figure 1 presents activity data for bulk HTO materials as a function of rhodium loading and reduction time at 300°C in hydrogen. The reaction was carried out at 200°C with a hydrogen to n-butane ratio of 20 to 1. The activities are normalized to the total weight of rhodium present in the catalysts. For low rhodium loadings the activity increases with activation time, while for high loadings the activity decreases with activation time. Curiously, normalized activities for all weight loadings converge to a constant value of approximately 4 μmoles of butane converted per gram of Rh per second. Given that hydrogenolysis is a structure sensitive reaction, with a rate dependent on particle size and morphology, the invariance of the normalized rate with rhodium loading suggests that similar rhodium particle sizes are present for all weight loadings. TEM images seem to support this conclusion, showing rhodium particles on the order of 2-3 nm in diameter for the higher weight loading catalysts. (For weight loadings below 5%, the particles are very difficult to find by TEM, presumably because the number of particles is low. TEM particle size measurements for these catalysts are therefore not conclusive.) This behavior is contrary to expectations regarding the effects of loading on particle size. Normally particle size increases with loading. Thus, unlike the Ni/HTO catalysts, in which the atomically dispersed nickel ions formed during ion exchange agglomerate into large, 20-30 nm particles during reduction,[2,3] rhodium ions remain highly dispersed during reduction, even for high weight loadings. One possible explanation for the changes in activity with reduction time observed for high and low weight loading catalysts involves the transformation of the atomically dispersed rhodium into metallic rhodium particles. For low loadings the

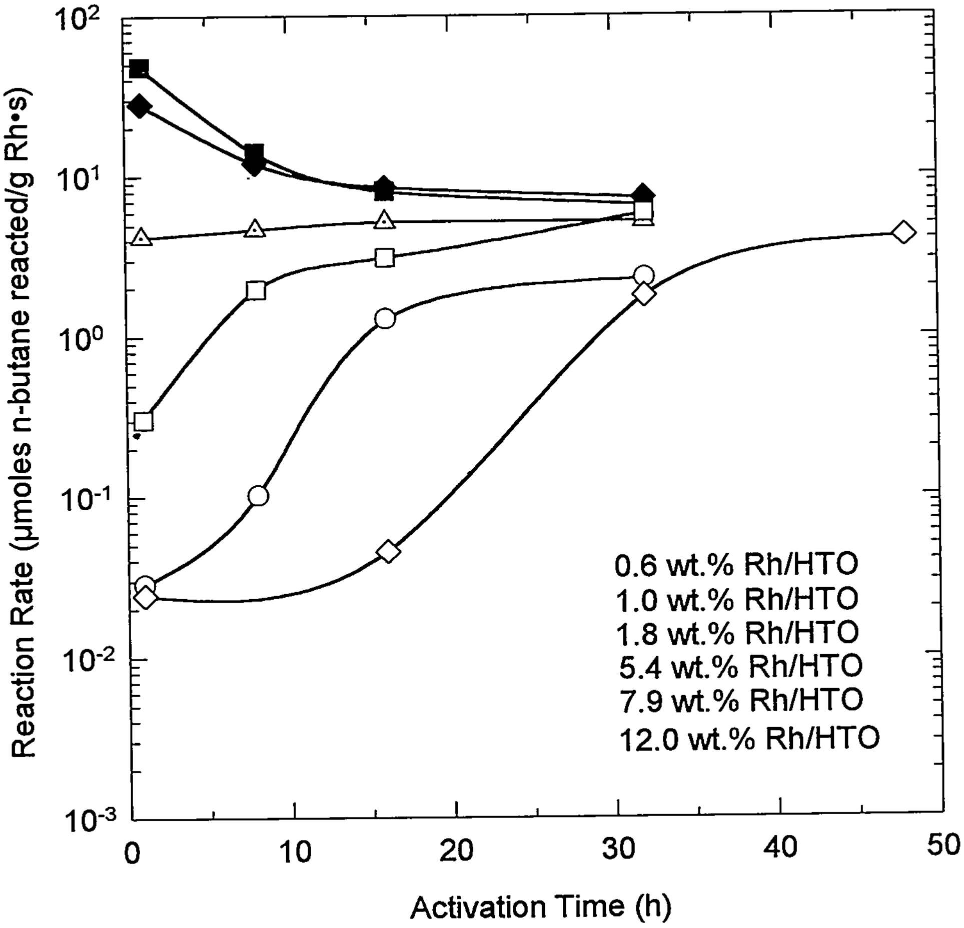

Figure 1: n-Butane Hydrogenolysis Activity of Rh/HTO Catalysts as a Function of Rhodium Loading and Hydrogen Activation Time. Reaction Conditions: 200°C, H_2:n-Butane = 20:1.

distance between individual rhodium ions is large and short reduction times are insufficient to form catalytically active particles. As the reduction time increases, the particles gradually grow to a sufficient size to be active and the normalized rate increases. As the particles continue to grow, the rate of diffusion and aggregation of the particles decreases and finally becomes negligible after 20-30 h. For high rhodium loadings, initial particle formation is rapid since the individual rhodium ions are in close proximity to each other. Thus, the catalysts are active even after very short reduction times. As reduction time increases, the initially formed small particles coalesce to form larger particles which present a smaller fraction of the rhodium atoms at the surface. Thus, the reaction rate decreases. As in the case of the low weight loading catalysts, the particle size eventually reaches a point at which further diffusion and particle growth is negligible and further changes in particle size do not occur.

Comparison of the steady state activity of the Rh/HTO catalysts to the activity of Rh/TiO_2 catalysts prepared by impregnation with $Rh(NO_3)_3$ indicates that the Rh/TiO_2 catalysts are substantially more active than the Rh/HTO catalysts, and also do not exhibit the variations in activity with reduction

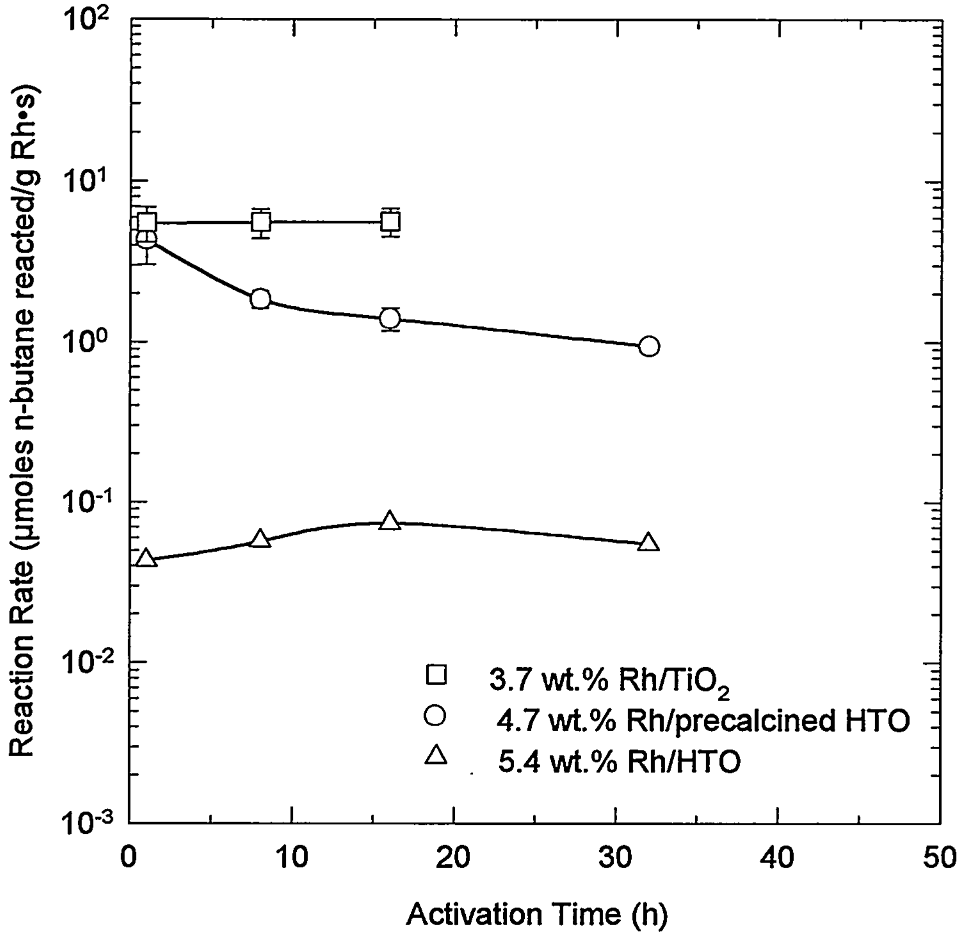

Figure 2: Comparison of n-Butane Hydrogenolysis Activity of Rh/HTO and Rh/TiO_2 Catalysts. The Catalyst Labeled "Precalcined" was Treated at 500°C in Air for 2 h Prior to Rhodium Exchange. Reaction Conditions Same as Figure 1 Except Temperature was 150°C.

time observed for the Rh/HTO catalysts (figure 2). The Rh/HTO catalysts exhibit substantially higher selectivity to ethane than Rh/TiO_2 catalysts. Figure 2 demonstrates that proper treatment of the HTO support prior to rhodium ion-exchange can increase the activity of Rh/HTO to levels comparable to that of a Rh/TiO_2 catalyst with a similar metal loading. This treatment involves calcining the HTO material at 500°C for 2 h prior to ion-exchange. High selectivity to ethane is retained with the calcined material. The increase in normalized activity comes at the expense of ion-exchange capacity and surface area, and the maximum Rh loading decreases from ~12% to ~5%. Nevertheless, the fact that HTO catalysts can be made comparable in activity to conventional impregnated Rh/TiO_2 catalysts is an important milestone in the development of HTO supported catalysts. Even if the activity of the HTO catalysts cannot be made superior to TiO_2 catalysts, the other superior properties of HTO materials, including flexibility in metal loading, higher selectivity, and thin film capabilities make the HTO system an attractive alternative to conventional catalysts.

Catalytic Activity of Thin Film Rh/HTO Catalysts

As mentioned above, the silica spheres coated with a monolayer HTO film have a large ion-exchange capacity, as demonstrated by exchange of rhodium onto the film surface at a pH of 4.0. Based on total weight of the coated sphere (silica plus HTO) the rhodium loading obtained under these conditions was 0.6 percent by weight, determined by atomic absorption. Based on the weight of HTO alone, the loading would of course be much higher. Identical exchange conditions result in negligible uptake of rhodium by the uncoated silica spheres.

The activity of the rhodium exchanged HTO film for n-butane hydrogenolysis was measured and compared to that of the bulk Rh/HTO materials. Figure 3 shows that the 0.6 wt% thin film Rh/HTO catalyst behaves similarly to the 12% bulk Rh/HTO catalyst, but quite differently from the 0.6% bulk Rh/HTO catalyst. This result is expected since both the 12% bulk catalyst and the 0.6% thin film catalyst have been loaded under conditions which maximize the amount of rhodium exchanged. As noted above, based on weight of the HTO film alone, the loading of the thin film catalyst would be much greater than 0.6%. EDX analysis of the HTO thin film indicates a titania loading of roughly 2-3%, meaning that the rhodium loading relative to titania is on the order of 20%. Thus, provided that thin film and bulk HTO materials have similar catalytic properties, correspondence between the 12% bulk Rh/HTO catalyst and the 0.6% thin film Rh/HTO catalyst is expected. The experimental observation of such a correspondence strongly suggests that the catalytic properties of bulk and thin film HTO materials are, in fact, similar. This result provides confidence that the extensive data on bulk HTO catalyst materials obtained in previous work will be directly applicable to thin film HTO materials, thereby decreasing the time necessary for development of thin film HTO supported catalysts.

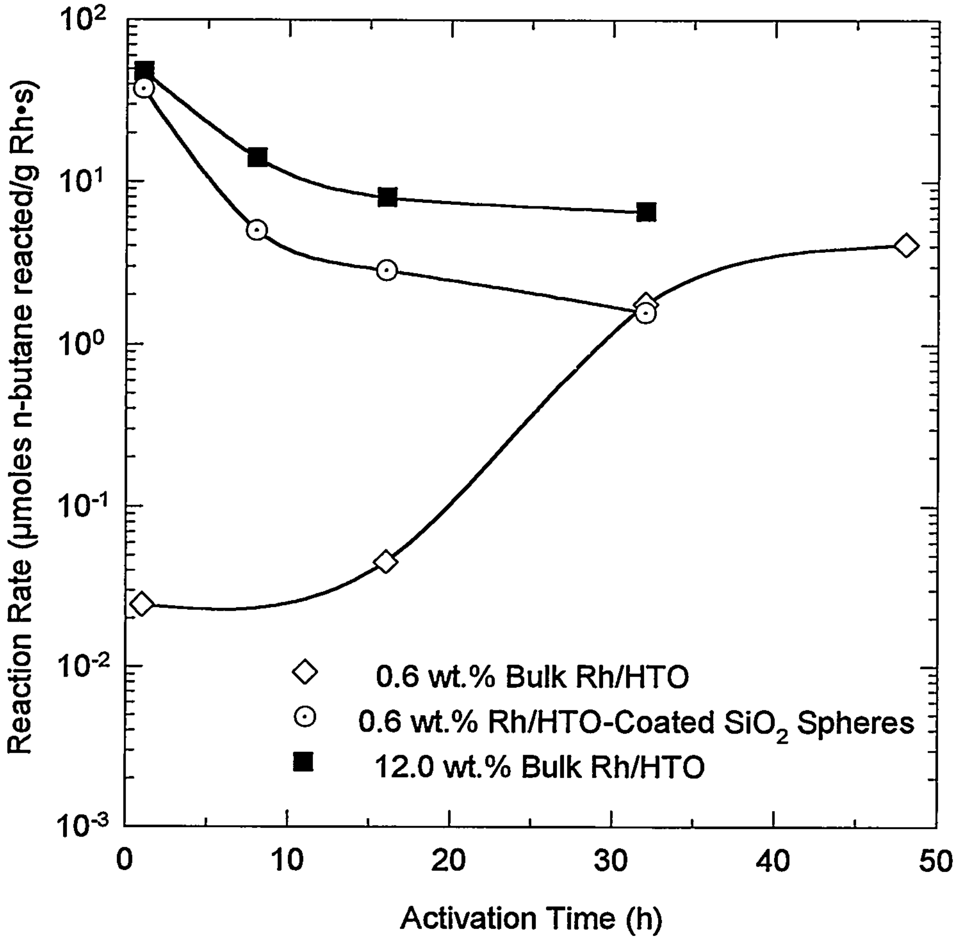

Figure 3: Comparison of n-Butane Hydrogenolysis Activity of Bulk and Thin Film Rh/HTO Catalysts. Reaction Conditions Same as Figure 1.

CONCLUSIONS

Substantial progress has been made in the growth of thin titania and HTO films on porous and nonporous substrates. With proper control of film growth conditions, titania films can be grown which completely cover porous silica substrates. HTO films are less well behaved due to the detrimental effects of NaOH in the precursor solutions on film growth. High quality monolayer HTO films have, however, been grown on nonporous silica spheres. These films appear fairly uniform in TEM images, and isopropanol dehydration indicates complete coverage of the silica surface. Ion-exchange of rhodium occurs readily on the monolayer HTO films, and the catalytic behavior of the Rh/HTO films corresponds closely to that expected based on studies of bulk Rh/HTO catalysts. This important result means that the large data base available for bulk HTO supported catalysts can be directly applied to the HTO films. Efforts are underway to further understand and control HTO film growth in order to produce high quality, high coverage films on high surface area substrates. Loading of both titania and HTO films with molybdenum is anticipated in the near future. These materials will be sulfided and tested for catalytic activity in reactions pertinent to coal liquefaction.

REFERENCES

1. (a) R. G. Dosch, H. P. Stephens, F. V. Stohl, B. C. Bunker, and C. H. F. Peden, "Hydrous Metal Oxide-Supported Catalysts: Part I. Preparation and Physical and Chemical Properties," *Sandia Report* (SAND89-2399). (b) R. G. Dosch, H. P. Stephens, and F. V. Stohl, "Hydrous Metal Oxide-Supported Catalysts: Part II. Catalytic Properties and Applications," *Sandia Report* (SAND89-2400). (c) R. G. Dosch and L. I. McLaughlin, "Hydrous Metal Oxide-Supported Catalysts: Part III. Development of NiMoHMO Catalysts," *Sandia Report* (SAND92-0388).

2. S. L. Anderson, A. K. Datye, E. J. Braunschweig, and C. H. F. Peden, *Appl. Catal.*, 82 (1992)185.

3. T. J. Gardner, C. H. F. Peden, and A. K. Datye, *Catal. Lett.*, 15 (1992) 111.

4. S. Srinivasan, A. K. Datye, M. Hampden-Smith, I. E. Wachs, G. Deo, J. M Jehng, A. M. Turek, and C. H. F. Peden, *J. Catal.*, 131 (1991) 260.

5. A. G. Sault, T. J. Gardner, C. S. Ashley, S. Srinivasan, and A. K. Datye, in Proceedings of the Seventh Annual Conference on Fossil Energy Materials, Department of Energy, Oak Ridge, TN, July, 1993, p. 139.

ADVANCED CERAMIC MATERIALS AND ELECTROCHEMICAL PROCESSES AT INTERFACES

T. R. Armstrong, J. L. Bates, L. R. Pederson,
J. W. Stevenson, and C. F. Windisch, Jr.

Pacific Northwest Laboratory[1]
P.O. Box 999
Richland, WA 99352

ABSTRACT

The overall purpose of this effort is to develop new ceramic materials for use as electrolytes, electrodes, and interconnects in solid oxide fuel cells and related devices; to identify primary features in solid oxide fuel cell operation that would limit system performance; to evaluate mechanical, structural and chemical stabilities of fuel cell materials; and to develop novel materials synthesis and processing methodologies to improve the quality and lower the cost of solid oxide fuel cell manufacture.

Interactions between the zirconia electrolyte and manganite cathode materials have been investigated. Such interactions are of interest because they may lead to changes in the cathode/electrolyte interfacial resistance. Interdiffusion profiles and diffusion coefficients were determined for electrolyte/electrode couples that had been sintered at temperatures from 1300 to 1500°C, similar to processing conditions necessary in the fabrication of some fuel cell designs. Manganese ions were found to be the most mobile species in zirconia, while lanthanum was the least mobile. Manganese penetration into the electrolyte was greatest for manganese-rich (A-site deficient) compositions and was favored by high level of substitution of calcium or strontium ions for lanthanum. The formation of interfacial lanthanum zirconate, and insulating phase, was not observed at the interface of zirconia and stoichiometric or A-site deficient manganites.

INTRODUCTION

Doped lanthanum manganites are among the most promising cathode materials for high-temperature solid oxide fuel cell applications. Compositions have been developed that exhibit high electrical conductivity, high electrocatalytic activity for the reduction of oxygen, provide a good thermal expansion match with other fuel cell components, and can withstand the high temperatures required for solid oxide fuel cell operation. In practical devices, long-term stability is a key issue. Reactions between fuel cell components, particularly at electrolyte/electrode interfaces, can lead to performance losses.

The reactivity of lanthanum manganite cathodes with yttria-stabilized zirconia (YSZ) has been studied by several researchers: Lau and Singhal[1] examined the reaction between Sr doped

---

[1] Operated by Battelle Memorial Institute for the US Department of Energy under Contract DE-ACC06-76RLO 1830

lanthanum manganite and YSZ, while Yamamoto et al.[2] investigated the kinetics of $La_2Zr_2O_7$ formation between lanthanum manganite and YSZ. Taimatsu et al.[3] examined the reaction between calcium doped lanthanum manganite and YSZ and concluded that the reaction proceeded by the diffusion of Mn, La and/or Ca into YSZ in one direction. Khandkar et al.[4] found that the diffusion of Mn into YSZ occurs along the YSZ grain boundaries. Most studies have concentrated on the reactions between YSZ and lanthanum manganite that take place during co-sintering of the cathode and electrolyte at elevated temperatures (>1300°C); little attention has been given to reactions that may occur during fuel cell operation at 1000°C. Furthermore, studies aimed at evaluating the diffusion of Mn into YSZ and determining the diffusion coefficient of Mn in YSZ have only been performed using single crystal YSZ. While this approach is necessary when determining solid-state diffusion coefficients, such results may not be applicable to predictions of the lifetimes of solid oxide fuel cells where polycrystalline zirconia electrolytes are used and the typical operating temperature is 1000°C.

CATHODE/ELECTROLYTE INTERACTIONS

Reaction couples of YSZ and $La_{1-x}A_xMnO_3$, where A is Ca or Sr and x varied from 0.1 to 0.3, were prepared using a two-step procedure. First, one powder was placed into a die and compacted using uniaxial pressure. The second powder was added to the die and the two were consolidated by a second uniaxial pressing. This step was followed by isostatic pressing at 140 MPa. These couples were heat treated at temperatures between 1300°C and 1500°C for 1 hour to determine the interactions that could occur during co-sintering. Reaction couples co-sintered at 1300°C for 1 hour were further held at 1000°C for times approaching 1000 hours to determine if reactions occur at the fuel cell operating temperature.

In every reaction couple involving $La_{1-x}Ca_xMnO_3$ or $La_{1-x}Sr_xMnO_3$ with YSZ, it was mainly the Mn ion that diffused significantly into YSZ; Zr and Y ions did not diffuse into the manganite, consistent with the results obtained by Lau and Singhal.[1] Calcium did diffuse into YSZ, but Sr did not at the temperatures studied. These data suggest that the solubilities of both Y_2O_3 and ZrO_2 in lanthanum manganite are low and that the reaction of lanthanum manganite with YSZ proceeds by diffusion of the cations in lanthanum manganite into the YSZ in one direction. Transmission electron microscopic analysis of a $(La_{0.60}Ca_{0.40})_{1.0}MnO_3$/YSZ couple sintered at 1400°C for 1 hour showed the formation of $CaZrO_3$, calcia-stabilized zirconia, and calcia, yttria-stabilized zirconia at the interface, as shown in Figure 1. Clearly, the solubility of Ca in zirconia is high and Ca diffuses into YSZ by bulk processes. Maximum migration distances of Mn and Ca are given in Table 1 for several diffusion couples following 1 hour soak at elevated temperatures.

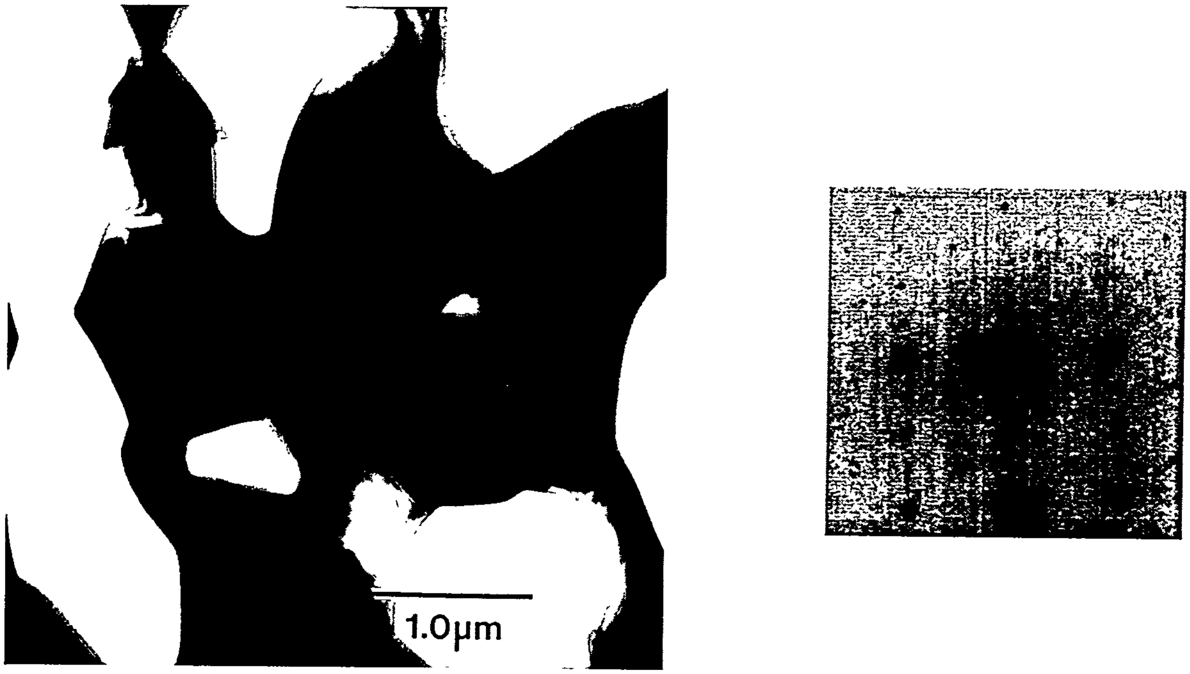

Figure 1. Transmission electron micrograph for a $La_{0.60}Ca_{0.40}MnO_3$/YSZ couple sintered at 1400°C for 1 hour, showing the formation of $CaZrO_3$. Electron diffraction pattern of $CaZrO_3$. [001] zone inset.

Table 1. Maximum Migration Distances of Manganese and Calcium From Manganite Cathodes into Yttria-Stabilized Zirconia During Sintering for 1 Hour. The Cathode Compositions Evaluated Provide a Good Thermal Expansion Match with Zirconia.

Reaction Couple, with YSZ	1300°C	1400°C	1500°C
$La_{0.6}Ca_{0.4}MnO_3$	Mn = 19 μm Ca = 10 μm	Mn = 47 μm Ca = 15 μm	Mn = 49 μm Ca = 25 μm
$La_{0.89}Sr_{0.1}MnO_3$	Mn = 20 μm	Mn = 25 μm	Mn = 30 μm
$Y_{0.6}Sr_{0.4}MnO_3$	Mn = 30 μm	Mn = 35 μm	Mn = 40 μm
$Y_{0.4}Ca_{0.6}MnO_3$	Mn = 19 μm Ca = 40 μm	Mn = 19 μm Ca = 40 μm	Mn > 200 μm Ca > 200 μm

Migration of cathode cations into the YSZ electrolyte were shown to be sensitive to the A-site to B-site ratios in these ABO_3 perovskites. Reaction couples that included cathode compositions enriched in Mn (B-site cation) relative to the sum of La, Y, Sr, and/or Ca (A-site cations) led to much-enhanced Mn penetration into the electrolyte but minimal migration of Ca. Cathode compositions that were enriched in A-site cations and containing Ca resulted in higher migration of that ion into the electrolyte but low penetration distances of Mn. Maximum migration distances for a $(La_{0.80}Ca_{0.20})_xMnO_3$/YSZ couple are given in Figure 2 following sintering at 1300°C for 1 hour and following sintering and soaking at 1000°C for 1000 hours, chosen to simulate fuel cell operation. Further Mn and Ca migration was apparent following the 1000°C treatment. These results emphasize the importance of precise stoichiometric control of cathode materials.

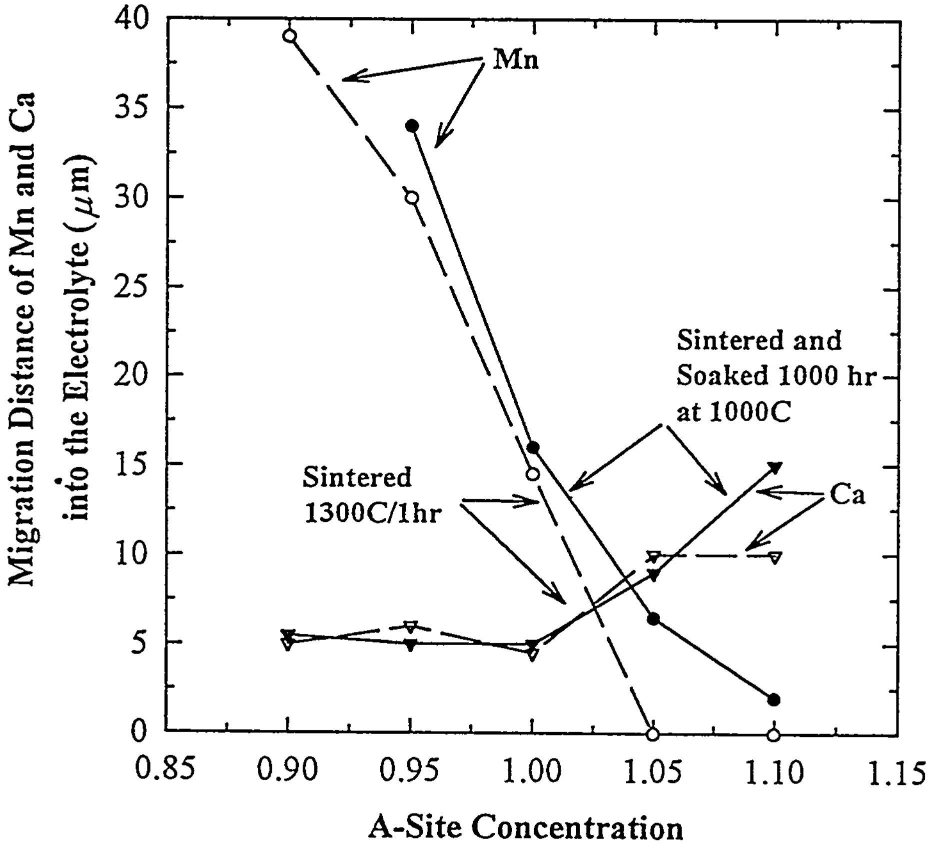

Figure 2. Maximum migration distances of manganese and calcium into the yttria-stabilized zirconia electrolyte from $(La_{0.80}Ca_{0.20})_xMnO_3$ cathodes as a function of the A/B site ratio.

In these studies, no $La_2Zr_2O_7$ pyrochlore phase formed at temperatures in the range 1300°-1500°C for time periods of 100 hours, for samples in which the perovskite A/B ratio was less than unity. When the A/B ratio exceeded unity a continuous layer of $La_2Zr_2O_7$ was found to form readily at the interface at 1300°C (100 hours). After soaking at 1300°C for 100 hours the thickness of the $La_2Zr_2O_7$ interfacial layer was 1-2 μm for both $(La_{0.8}Ca_{0.2})_{1.02}MnO_3$ and $(La_{0.84}Sr_{0.16})_{1.02}MnO_3$. These results again clearly indicate the important role that stoichiometry of the perovskite plays in formation of the pyrochlore phase and the need for precise control of stoichiometry during synthesis.

From the diffusion profiles of Mn and La into the zirconia electrolyte obtained for various diffusion couples, diffusion coefficients can be determined. Figure 3 shows the diffusion profile for a $La_{0.6}Ca_{0.4}MnO_3$/YSZ couple sintered at 1400°C for 1 hour. This figure shows that Mn diffuses ≈40 μm, La ≈10 μm and Ca≈18 μm into YSZ. Determination of the diffusion coefficients enables predictions of the times required for Mn or Ca to completely diffuse through YSZ. This is important since Mn doping of YSZ results in enhanced electronic conductivity, which will result in the development of a short circuit in the electrolyte. It was assumed that diffusion of La, Mn, and Ca into YSZ was unidirectional and that the boundary condition was maintained at constant concentration (C_o). It was further assumed that grain boundary diffusion was the dominant mechanism of mass transport. If the diffusion coefficient is constant in the diffusion region and no expansion of the region occurs during diffusion, then the solution can be given:[5]

$$C(x,t) = C_o \operatorname{erfc} (x/2(Dt)^{0.5}) \qquad (1)$$

where C(x,t) is the concentration at distance x during operating time t and D is the diffusion coefficient. Table 2 shows the diffusion coefficient for Mn in YSZ for co-sintered samples and for samples held at 1000°C for 1000 hours. The diffusion coefficient of Mn in YSZ decreases with the perovskite A/B ratio approaching 1. Further, the lanthanum manganites have lower diffusion coefficients than pure manganese oxide. This may be explained the reduction in activity of manganese oxide when combined with lanthanum and a dopant such as Ca or Sr.

Table 2. Diffusion Coefficients of Manganese into Yttria-Stabilized Zirconia for Strontium-Doped Lanthanum Manganites.

Sample	Temperature (°C)	Time (hours)	Diffusion Coefficient (cm^2/second)
$La_{0.89}Sr_{0.10}MnO_3$	1300	1	1×10^{-10}
$La_{0.89}Sr_{0.10}MnO_3$	1400	1	5×10^{-10}
$(La_{0.84}Sr_{0.16})_{0.96}MnO_3$	1300	1	2×10^{-10}
$(La_{0.84}Sr_{0.16})_{0.96}MnO_3$	1300	1	2×10^{-10}
$(La_{0.84}Sr_{0.16})_{0.96}MnO_3$	1300	1	1.5×10^{-11}
Mn_2O_3	1300	1	5×10^{-10}
$(La_{0.84}Sr_{0.16})_{0.96}MnO_3$	1000	1000	1.5×10^{-13}
$(La_{0.84}Sr_{0.16})_{0.96}MnO_3$	1000	1000	4×10^{-14}

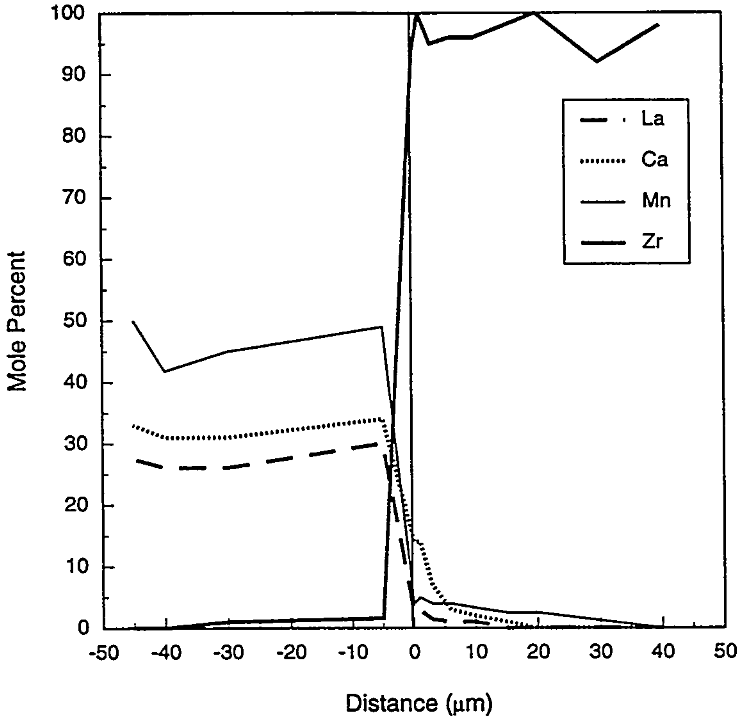

Figure 3. Diffusion profile of $La_{0.6}Ca_{0.4}MnO_3$/YSZ couple sintered at 1400°C for 1 hour.

Based on the diffusion coefficients in Table 2, for samples held at 1000°C, using $x \approx (Dt)^{0.5}$ Mn would completely diffuse through a 100 μm electrolyte in 277,000 hours, if the diffusion coefficient were 10^{-13} cm^2/sec.

Activation energies for manganese diffusion in YSZ could also be obtained from the present data. In Figure 4, diffusion coefficients are given as a function of reciprocal temperature for two (La,Ca)MnO_3 compositions and for Mn_2O_3. Lowest activation energies and highest diffusion constants were obtained for Mn_2O_3/YSZ reaction couples, while highest activation energies and lowest diffusion constants were found for (La,Ca)MnO_3 compositions containing the smallest concentration of calcium.

In summary, interfacial reactions between doped manganite cathode compositions and yttria-stabilized zirconia were evaluated. Manganese was found to be the most mobile into zirconia, while lanthanum was the least mobile. Manganese migration into zirconia was greatest for A-site-deficient compositions, and was also favored by high A-site substitution of alkaline earth cations for lanthanum or yttrium. Calcium readily diffused into YSZ whereas strontium did not. For reactions of A-site-deficient manganite compositions with zirconia, no interfacial lanthanum zirconate phase was ever observed, either at temperatures of 1300°C or greater that are needed for co-sintering or after extended periods at 1000°C, the standard operating temperature for solid oxide

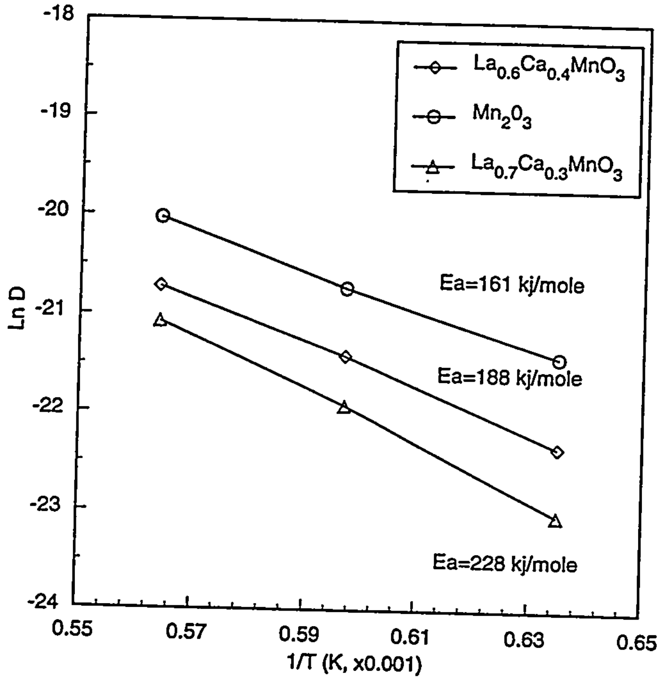

Figure 4. Diffusion constants for (La,Ca)MnO_3 cathodes and Mn_2O_3 as a function of reciprocal temperature.

fuel cells. Because lanthanum zirconate is electrically insulating, its formation may severely limit long-term fuel cell performance and is thus to be avoided. Cathode compositions where the A-site was enriched did lead to lanthanum zirconate formation, however. These results demonstrate that careful stoichiometric control of cathode compositions is essential to prevent the formation of secondary phases.

REFERENCES

1. S. K. Lau and S. C. Singhal, in Corrosion 85, The National Association of Corrosion Engineers (NACE) Meeting, Boston, MA, pp.345/1-9, March 25-29, 1985, National Association of Corrosion Engineers, Houston, TX, 1985.

2. O. Yamamoto, Y. Takeda, R. Tanneo, and T. Kojima, in Proceedins of the International Symposium on Solid Oxide Fuel Cells, Nagoya, Japan, pp. 87-89, November 13-14, 1989, SOFC Society of Japan, Nagoya, Japan.

3. H. Taimatsu, K. Wada, and H. Kaneko, *J. Am. Ceram. Soc.*, 75 [2] 401-405 (1992).

4. A. Khandkar, S. Elangovan, and M. Liu, *Solid State Ionics*, **52** 57-68 (1992).

5. H. S. Carslaw and J. C. Jaeger, pp. 60 in Conduction of Heat in Solids, Oxford University Press, Oxford, UK, 1959.

MICROWAVE-ASSISTED CHEMICAL VAPOR DEPOSITION

Mark A. Janney

Oak Ridge National Laboratory
P. O. Box 2008
Oak Ridge, Tennessee 37831-6087

OVERVIEW

The purpose of this research is to explore the feasibility of using microwave heating to enhance the chemical vapor infiltration (CVI) process developed under FEMP sponsorship. The goal is to achieve faster deposition rates, greater control over deposition conditions and resulting microstructures, and perhaps lower temperature infiltration.

INTRODUCTION

Forced flow chemical vapor infiltration has been demonstrated at ORNL to be an excellent technology for the fabrication of continuous filament composites. Silicon carbide is the preferred matrix and both silicon carbide and oxide fibers have been used successfully as the reinforcing phase. Combining CVI with microwave processing may result in an improved CVI process through better control of heating and enhanced reaction rates associated with the microwaves.

It is proposed that there will be specific benefits to be derived from combining the current CVI technology with microwave processing to form MW-CVI. First, from a purely physical perspective, microwave heating of the substrate may give more control to the heating pattern in the sample. This would be especially true for the combination of oxide fibers with an SiC matrix. The oxide fibers are transparent to the microwaves and the SiC is a good microwave absorber. Therefore, only the SiC phase will be heated. This will establish a natural gradient in temperature with the SiC being the hottest part of the sample. This gradient will be similar to that established by external cooling in the current forced flow CVI process. Second, there may be microwave-enhanced reactions that occur during deposition. In work at ORNL on the reaction of silicon with nitrogen gas, it has been demonstrated that the rate of reaction to form silicon nitride is much higher for microwave processing than for conventional processing. Similar rate increases have been demonstrated by other researchers in a variety of organic reactions in both the liquid and vapor phases. Therefore, CVI reactions might be accelerated by the use of microwave processing.

TECHNICAL PROGRESS

An existing 700W microwave furnace was modified to accommodate the CVI experiment. Modifications were made to the furnace so that a bell jar could be installed inside the microwave furnace to contain reactive gases such as methyltrichlorosilane (MTS). Appropriate gas handling equipment was constructed outside the furnace. The entire experiment was sited inside a fume hood. Non-contact methods of temperature measurement (2-color IR pyrometry) were developed to monitor the temperature of the preforms during deposition of the SiC into the fiber lay-up.

One of the most important areas to be determined at the beginning of this study was the particular experimental setup to be used. From other microwave processing studies, we had determined that experimental setup was a vital component of a successful project.

The first set of experiments focused on our ability to heat a Nicalon® preform to the coating temperature of 1200°C. A statistically-designed set of experiments was performed based on the Taguchi-style design of experiments. A reduced factorial design was used that allows one to investigate the effects of several factors using a limited number of experiments.

The following factors were selected as being most important to study:

(1) the number of layers of Nicalon® cloth - It has been demonstrated in many earlier studies of microwave heating of ceramic materials that the volume of material being heated is an essential element in how efficiently it heats. For many materials, the efficiency of microwave heating increases markedly with increasing mass up to a plateau value.

(2) the composition of the insulation - The two main insulations used in microwave processing are alumina and zirconia fiberboard. Alumina insulation is essentially transparent to microwave radiation for most applications and therefore acts only as a thermal insulator. Zirconia insulation is a reasonably good absorber of microwave radiation, especially at higher temperatures, and therefore may increase the highest temperature achievable during microwave irradiation.

(3) the amount of insulation - For conventional heating, a more efficient insulating arrangement would be expected to lead to better heating. However, in microwave processing, the unexpected happens more often than the expected.

(4) the atmosphere - The atmosphere may be expected to affect how efficiently the sample could be heated based on heat transfer considerations.

The Factor Table for the experiment, Table 1, shows the particular test conditions that were run in this study. Figure 1 shows the physical arrangement of the experiment.

Experiment Number	Insulation Arrangement (# Layers)	Preform Size	Atmosphere	Insulation Composition
1	Top & Bottom	10	air-no jar	alumina
2	Top & Bottom	20	air-jar	zirconia
3	Top & Bottom	15	H2-jar	zirconia
4	T&B + Ring	10	air-jar	zirconia
5	T&B + Ring	20	H2-jar	alumina
6	T&B + Ring	15	air-no jar	zirconia
7	T&B, Ring, T&B-2	10	H2-jar	zirconia
8	T&B, Ring, T&B-2	20	air-no jar	zirconia
9	T&B, Ring, T&B-2	15	air-jar	alumina

Table 1. A Taguchi-Style Reduced Factorial Design Was Used to Study the Heating of Nicalon® Preforms in the Microwave Furnace.

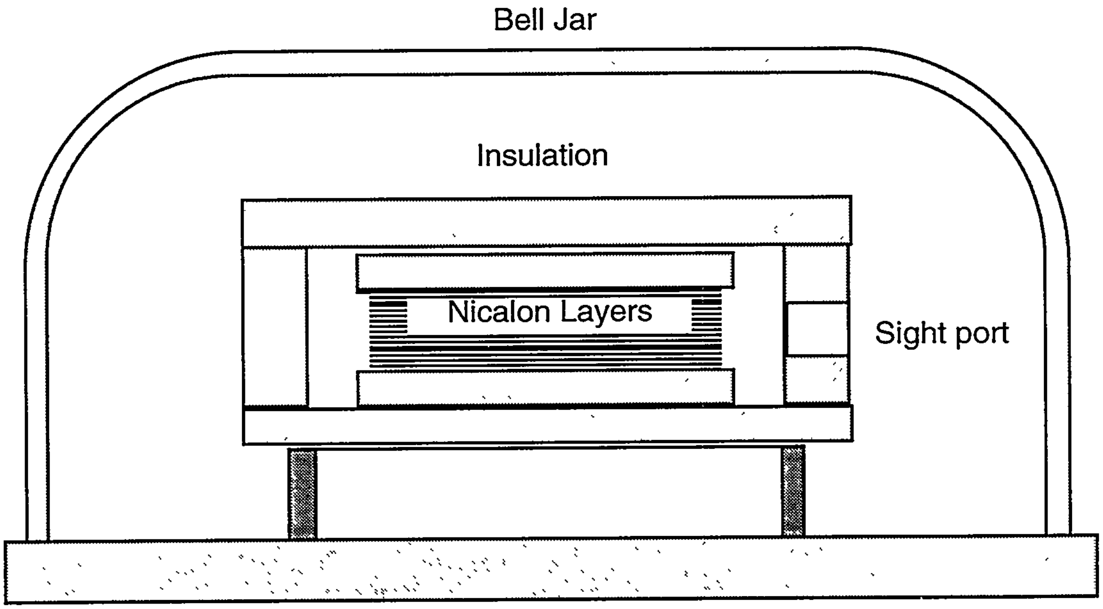

Figure 1. Experimental configuration for heating Nicalon® cloth lay-ups in a 700W microwave furnace. Nicalon® cloth lay-ups of 10 to 20 layers were insulated with different configurations of alumina or zirconia fiberboard and were heated in air, nitrogen, or hydrogen. Temperature was measured with a two-color infrared pyrometer which was sighted on the edge of the Nicalon® stack.

The results of the experiments are summarized in the Response Table, shown as Table 2. Two sets of experiments are reported in Table 2. In the first set, the three atmosphere test conditions were: (1) in air, (2) in air in the bell jar, and (3) in hydrogen at 0.5 atm pressure in the bell jar. In the second set, nitrogen at 1 atm pressure replaced hydrogen. The most important factor was determined to be the use of hydrogen at 1 atm. In this case, it was demonstrated that effective heating was not possible in the existing 700W microwave furnace. That is, temperatures above 800°C could not be generated because the hydrogen was highly effective in convecting heat away from the sample to the bell jar. In addition, it was demonstrated that samples could not be effectively heated at vacuum levels achievable with a mechanical vacuum pump (~50 mTorr). A plasma formed inside the bell jar which

Factor	**Temperature @ 415W (°C) (H_2 @ 0.5 atm)**	**Temperature @ 470W (°C) (N_2 @ 1 atm)**
Insulation configuration		
Top & Bottom	906	1195
T&B plus Ring	906	1246
T&B, Ring, 2nd T&B	933	1285
Layers of Nicalon® cloth		
10	938	1256
15	890	1232
20	916	1239
Atmosphere		
Air - no bell jar	1095	1357
Air - bell jar	999	1206
H_2 / N_2 - bell jar	650	1163
Insulation composition		
Alumina	873	1138
Zirconia	936	1294

Table 2. Response Table for Nicalon® Heating Experiments

absorbed virtually all of the microwave power. Essentially no heating of the Nicalon® sample occurred.

The second most important factor was the use of the bell jar, which markedly reduced the heating efficiency. The reason for the drop in heating effectiveness with the bell jar is as follows. The base of the bell jar is made of aluminum, which shields the sample from the microwave radiation. It therefore effectively reduces the power available for heating the sample.

Similar in importance to the use of the bell jar was the use of zirconia instead of alumina insulation. As was mentioned above, zirconia insulation absorbs microwaves quite effectively at elevated temperatures. It therefore acts like an "electric blanket" in helping to heat the sample it is surrounding.

Another important factor was the total amount of insulation. The more insulation, the better the heating efficiency. This suggests that conventional heat transfer considerations are important for this application of microwave heating.

The least important factor investigated was the number of layers of Nicalon® cloth used for the sample. The highest temperatures were achieved using the smallest number of layers of cloth. However, the effect of increasing the number of layers of cloth from 10 to 20 was small.

Based on what has been learned so far, we have decided that more power is required to conduct the CVI experiments on the current scale (nominal 10 to 20 grams of Nicalon® cloth) or on larger scales in the future. Therefore, the entire experiment is being transferred to a larger microwave furnace, which has 12 kW of microwave power available.

In the coming months, the MW-CVI process will be investigated in terms of the kinetics of deposition and microstructural evolution, and compared to the baseline conventional processing. A set of statistically-designed experiments (Taguchi-style) will be conducted to determine the key aspects that control the process. The parameters that will be studied will include the temperature of the substrate, size of the substrate, flow rates of the reactant gases, gas pressure, type of reactant gas e.g., (MTS vs $SiCl_4$ - CH_4), type of insulation system, microwave power levels and so on. We have been contacted by two industrial firms who are interested in working with us in the future on MW-CVI projects.

EFFECT OF HEAT TREATMENT TEMPERATURE ON CREEP-RUPTURE PROPERTIES OF Fe_3Al-BASED ALLOYS

C. G. McKamey and P. J. Maziasz

Oak Ridge National Laboratory
P. O. Box 2008
Oak Ridge, TN 37831-6114

ABSTRACT

The effects of heat treatment at 1100 to 1250°C on the creep-rupture properties of an Fe_3Al-based alloy were studied. Tests were conducted at 593°C (1100°F) and 207 MPa (30 ksi) in air. The modes of fracture were identified using optical metallography and scanning electron microscopy. Analytical electron microscopy was also used to study characteristics of the microstructure, including dislocations, ordered domains, and precipitates. The creep results showed maximum creep-rupture resistance with a heat treatment at approximately 1150°C, with significant decreases in rupture life after heat treatments at both lower and higher temperatures. The peak in creep life was associated with fine precipitates that were observed after the 1150°C heat treatment and persisted during prolonged creep at 593°C. Heat treatment at 1150°C appeared to cause dissolution of coarser precipitates which then reprecipitated as new fine particles upon cooling or during creep. These fine precipitates then pinned dislocations and grain boundaries to produce strength during creep.

INTRODUCTION

Past studies have shown that binary Fe_3Al possesses low creep-rupture strength compared to many other alloys, with creep-rupture lives of less than 5 h being reported for tests conducted at 593°C and 207 MPa (ref. 1). The combination of poor creep resistance and low room-temperature tensile ductility due to a susceptibility to environmentally-induced dynamic hydrogen embrittlement[2,3] has limited use of these alloys for structural applications, despite their excellent corrosion properties.[4] Improvements in room-temperature tensile ductility have been realized mainly through alloying effects, changes in thermomechanical processing to control microstructure, and by control of the surface condition.[5] These changes in metallurgical variables have produced ductilities of 10-20% and tensile yield strengths as high as 500 MPa (ref. 6,7). In terms of creep-rupture strength alone, small additions of Mo, Nb, and Zr have produced significant improvements, but at the expense of room-temperature tensile ductility and weldability.[1,8-10] Further efforts are therefore necessary to produce a Fe_3Al-based composition with an acceptable combination of both room-temperature tensile and high-temperature creep-rupture properties.

This study presents the results of efforts to further improve the creep-rupture strength of Fe_3Al-based alloy compositions through control of the microstructure. One composition containing small additions of Nb, Mo, Zr, B, and C was chosen as the base alloy to investigate the effect of heat treatment temperature on the microstructure and creep-rupture properties.

EXPERIMENTAL PROCEDURES

The alloy composition used in this study was Fe-28 at.% Al with 0.5% Nb, 0.8% Mo, 0.025% Zr, 0.05% C, and 0.005% B (Oak Ridge National Laboratory designation FA-180). It was prepared by arc-melting and drop-casting into a chilled copper mold. Fabrication to 0.8-mm-thick sheet was accomplished by hot-rolling, beginning at 1000°C and finishing at 600-650°C. After a stress relief heat treatment of 1 h at 700°C, flat tensile specimens (0.8 x 3.18 x 12.7 mm) were mechanically punched from the rolled sheet. Before testing, the tensile specimens were further annealed in air for 1 h at temperatures ranging from 1100 to 1250°C and air cooled. The results were compared to specimens which were heat treated at 750°C, a temperature which has been shown to result in predominantly a B2 ordered structure and to produce a maximum in the room temperature tensile ductility.[11,12] Creep-rupture tests were performed in air at

593°C and a stress of 207 MPa (30 ksi). Minimum creep rates (MCR) were measured as the slope of the linear portion of the test curve. Optical metallography and scanning electron microscopy (SEM) were used to study the microstructures and fracture modes. Analytical electron microscopy (AEM) using either a Philips CM30 (300 kV) or CM12 [120 kV, with ultra-thin-window x-ray energy dispersive spectrometry (XEDS) detector] electron microscope was performed on samples cut from the gage portion of selected test specimens.

RESULTS AND DISCUSSION

Creep-Rupture Behavior

The 750°C heat treatment temperature was used to provide a baseline for comparison with the other heat treatments. This heat treatment produced an average creep life of approximately 100 h for two tests (see Table I). Preliminary results on alloys with slightly different compositions indicated that only limited increases in creep life could be expected for heat treatments below approximately 1000°C (ref. 13,14). Therefore, for this series of tests, heat treatments were performed between 1100 and 1250°C. The temperatures chosen and the results of creep-rupture tests at 593°C are shown in Table I and Fig. 1. Creep-rupture life is plotted as a function of heat treatment temperature in Fig. 2, where the dashed line represents the 100-h average creep life for the 750°C heat treatment. The results show a dramatic maximum in creep-rupture lifetime with a heat treatment at about 1150°C. In addition, both MCR and elongation to rupture decreased to their lowest values at 1150°C. Compared to the specimens heat treated at 750°C, the total creep-rupture strain is decreased by about a factor of ten, while the MCR is reduced by a factor of more than 10^3 after heat-treatment at 1150°C. Together these results indicate that the increased creep resistance is mainly an issue of creep strength, with rupture occurring at fairly low creep strain values. Much lower creep-rupture strength was observed for heat treatment below 1125°C or above 1175°C.

Table I. Effect of 1-h heat treatment on creep-rupture properties of a Fe_3Al-based alloy[a]

Heat treatment temperature (°C)	Grain size (µm)	Life (h)	Elongation (%)	MCR (%/h)
750	b	91	79	0.3
		103	75	0.3
1100	62	187	44	0.03
		235	36	0.03
1125		349	42	0.04
		222	20	0.01
		602	12	0.004
1150		2732	9	0.0005
		1530[d]	7	0.001
1175		985	31	0.002
	122,350[c]	840	10	0.0001
1200		343	36	0.02
		285	31	0.05
		181	26	0.06
1225		135	17	0.09
	78	109	25	0.09

[a] Composition = Fe-28Al-5Cr-0.5Nb-0.8Mo-0.025Zr-0.05C-0.005B (at.%).

[b] Rolled microstructure, ≈10-20% recrystallized, with ≈20 µm grains.

[c] Duplex microstructure, see text for discussion.

[d] This specimen ruptured at room temperature after the furnace failed during testing. It was not plotted in Fig. 2.

Microstructural Analysis

The fracture surfaces were observed using SEM, while the microstructures in the fracture regions were studied using optical microscopy of cross-sectioned specimens. SEM of the fracture surfaces showed that a ductile dimple type of fracture, with many large creep cavities, occurred for all heat treatment temperatures, including 750°C. Coarse precipitates could be observed at the bottom of most of these dimples (Fig. 3).

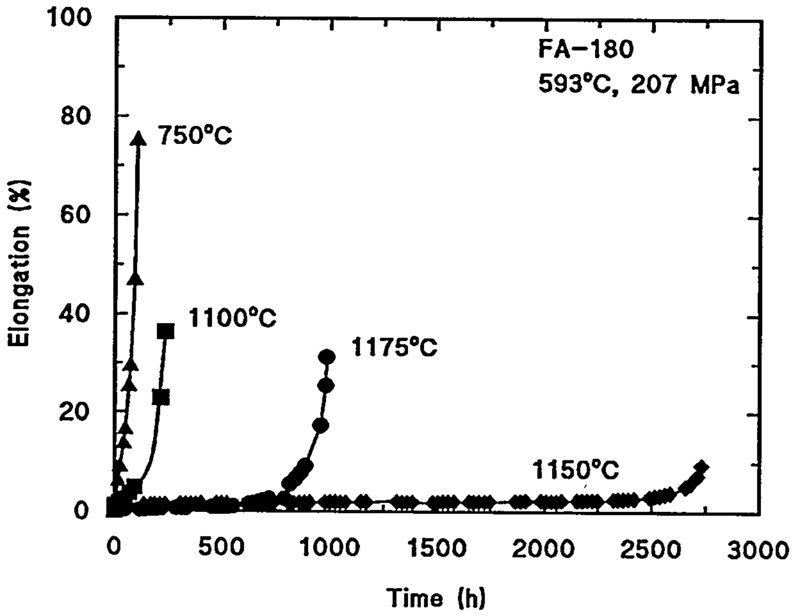

Fig. 1. Creep-rupture curves of alloy FA-180 heat treated at temperatures of 750, 1100, 1150, and 1175°C. Tests were conducted at 593°C and 207 MPa.

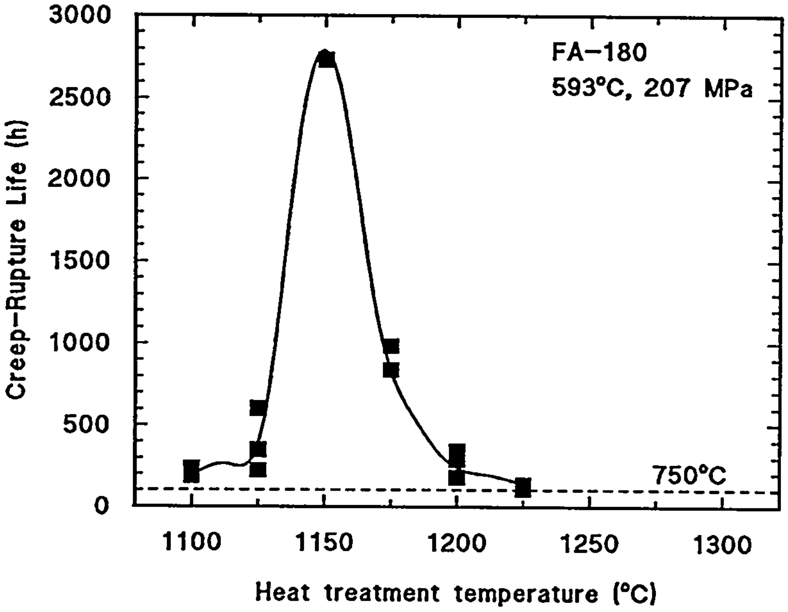

Fig. 2. Creep-rupture life as a function of heat treatment temperature for tests conducted on alloy FA-180 at 593°C and 207 MPa.

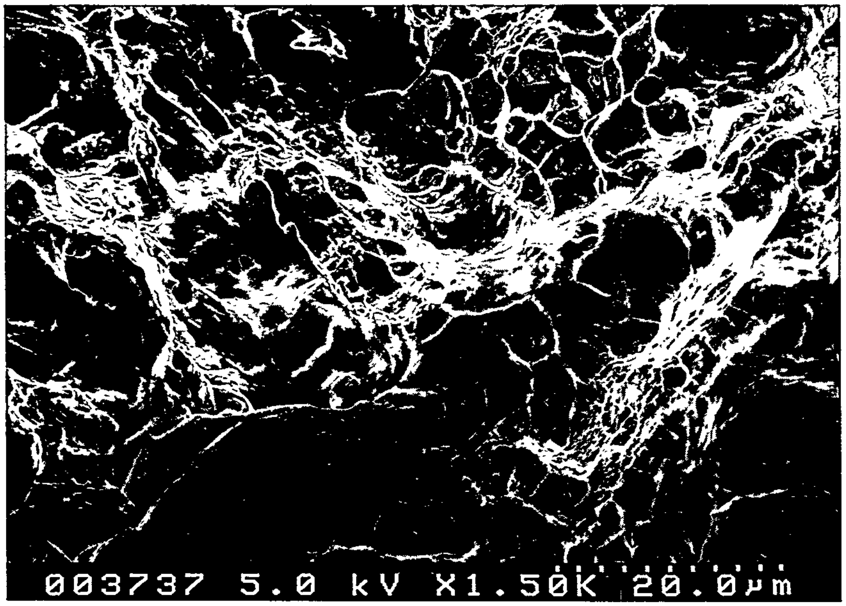

Fig. 3. Scanning electron fractograph showing ductile creep failure of alloy FA-180 and the presence of precipitates at the bottom of most dimples.

The effect of creep on the optical microstructure was determined by comparing the strained microstructure from the gage of the specimen to the unstrained microstructure of the shoulder. The 750°C heat treatment produced primarily a highly banded structure, typical of sheet hot-rolled at 650°C [Fig. 4(a)], with small equiaxed grains (about 20 µm in diam.) nearer to the surfaces indicating about 20% recrystallization [Fig. 4(a)]. Grains for the 1100 and 1225°C heat treatments were equiaxed and ranged from 60-80 µm in size [Fig. 4(b,d)]. These grain sizes are smaller than those reported earlier for binary Fe_3Al heat treated at 850°C (ref. 1), indicating a substantial effect of alloying additions in FA-180 on retarding grain growth. The starting grain size was also determined for a specimen heat treated at 1175°C. Measurements from six different fields through the cross section indicated a bimodal grain-size distribution [Fig. 4(c)], with grain diameters ranging from approximately 120-125 µm to a few unusually coarse grains as large as 500-700 µm. While such a maximum in grain size with heat treatment temperature is unusual, it does correlate well with the creep life data shown in Fig. 2; the

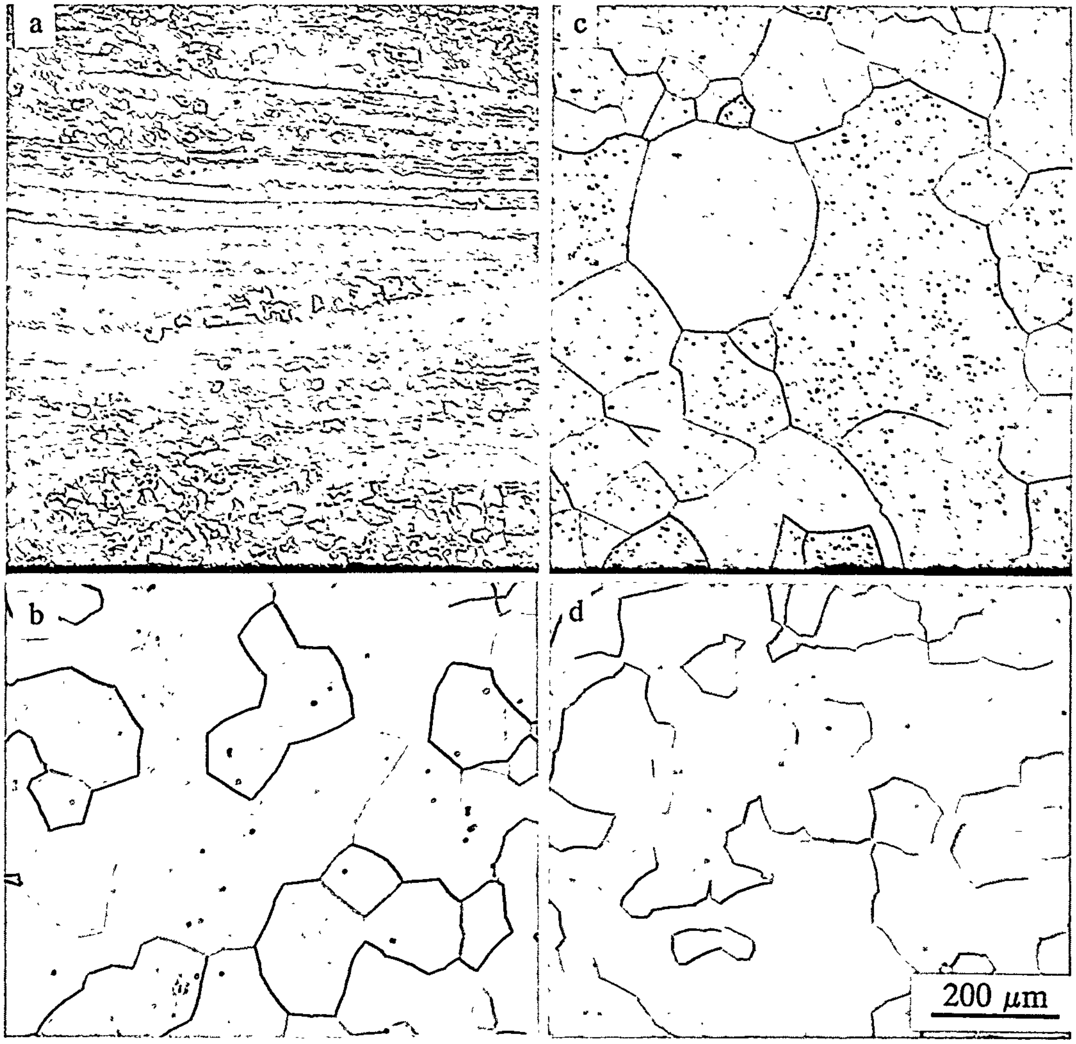

Fig. 4. Optical micrographs showing microstructures before creep testing of FA-180 specimens heat treated at (a) 750, (b) 1100, (c) 1175, and (d) 1225°C.

large-grained bimodal microstructure produced by the 1175°C heat treatment is consistent with the maximum in creep-rupture resistance observed compared to the smaller-grained microstructures produced by the 1100 and 1225°C heat treatments.

Figure 5 shows optical cross-section micrographs of the fractured specimens with various heat treatments. Again, optical analysis confirmed the ductile fracture mode with varying degrees of necking near the failure surfaces. None of these specimens showed the gross grain boundary separation that was observed in a Fe_3Al binary (Fe-28 at.% Al) alloy similarly

Fig. 5. Optical micrographs showing the microstructure at the fracture of specimens heat treated at (a) 1100, (b) 1175, and (c) 1225°C and tested at 593°C.

creep tested.[1] However, there were some differences in grain size and morphology in the failure regions for this heat-treatment series. The specimen heat treated at 1100°C retained its uniform grain size of 60-80 μm in the gage during creep testing at 593°C for 187 h, but the grains were elongated due to the higher creep strain (44%) that it sustained [see Fig. 5(a)]. By contrast, the specimen heat treated at 1225°C, which had a more uniform grain size of approximately 78 μm before testing, showed a bimodal grain morphology after testing for only 109 h, with small areas of 100-150 μm diameter grains and much larger areas of very coarse grains which filled the thickness of the specimen (~700 μm) [see Fig. 5(c)]. The specimen heat treated at 1175°C showed behavior in between these extremes. It had a bimodal grain size morphology prior to testing and then maintained that morphology throughout the entire 840 h of testing [see Fig. 5(b)]. The grain morphology in this specimen also remained fairly equiaxed during the test, consistent with the low creep strain measured (10%), and serves as evidence of a strengthening mechanism that completely stabilized the microstructure.

Transmission electron microscopy (TEM) was used to examine both the as-heat-treated microstructures and the post-creep-tested microstructures of specimens heat treated at 750, 1100, 1150, and 1225°C. Before creep testing, the specimen heat treated at 750°C had a recovered matrix microstructure typical of a warm-rolled structure, with dislocations primarily forming subgrain boundary arrays that were about 1 μm or less in size (Fig. 6). Small recrystallized grains (1-3 μm diam.) were also observed along grain boundaries, consistent with the partial recrystallization observed optically. Most of the matrix dislocations appeared to be two-fold B2 superdislocations, and no fine precipitation was detected. This specimen did contain a few large particle clusters made up of several smaller particles. AEM analysis showed most of these particles to be either zirconium-rich carbides or niobium-rich carbides with some zirconium. Some of these clusters had aluminum nitride particles at the core.

Fig. 6. Transmission electron micrograph showing microstructural features of FA-180 as-heat-treated at 750°C.

TEM examination of untested specimens heat treated at 1100-1225°C revealed coarse dislocation-free grains and the coarse B2 and fine $D0_3$ anti-phase boundary (APB) structure characteristic of well-annealed material.[12,15] However, these specimens also showed strong effects of solution-annealing temperature on fine precipitation behavior. The specimen annealed at 1100°C showed no detectable precipitation at grain boundaries or in the matrix. The specimen annealed at 1150°C showed abundant fine (5-10 nm diam.) precipitates uniformly distributed in the matrix, but no such precipitation along the grain boundaries (Fig. 7). Dynamical strain-contrast image behavior (rotation of the black-white strain image with the diffracting vector) indicated that these fine features were indeed precipitates, and not dislocation loops.[12] By contrast, the specimen annealed at 1225°C had no fine matrix precipitates, but did have abundant fine precipitates along the grain boundaries. This specimen also had sparse stringers of coarser precipitates rather than the isolated clusters of MC carbides found in the hot-rolled material heat treated at 750°C.

In specimens heat treated at 750°C, creep deformation produced a uniform and much denser tangled network of 2-fold superdislocations with fewer dislocation subgrain-boundary

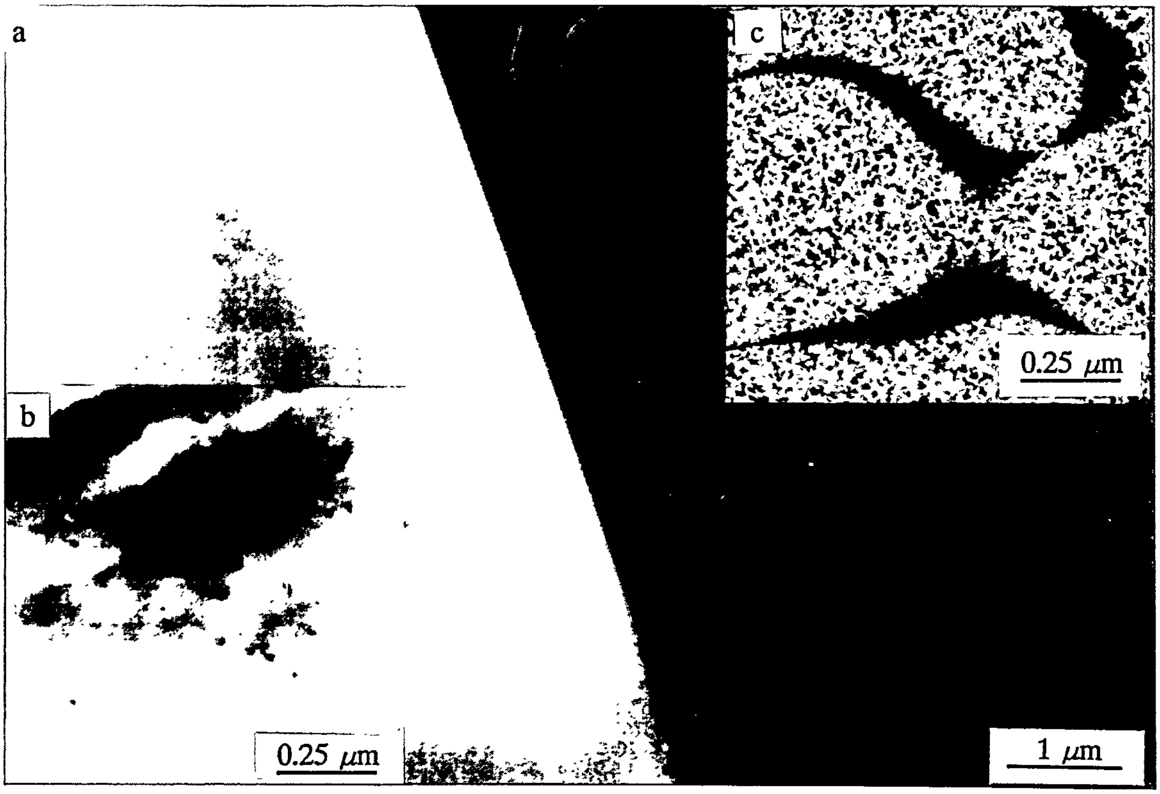

Fig. 7. Electron micrographs showing microstructural features of FA-180 as-heat-treated at 1150°C: (a) clean grain boundaries, (b) fine matrix precipitates, (c) fine $D0_3$ structure within coarse B2.

arrays relative to the microstructure found after heat treatment at 750°C. The coarse MC clusters present in the as-heat-treated material remained after creep, but some additional 0.1-0.3 μm particles appeared adjacent to these clusters after creep. There were no fine precipitates detected in the matrix.

Creep (over 1500 h at 593°C) of the specimen heat treated at 1150°C produced a denser, more tangled network of 2-fold superdislocations compared to the previously described specimen. Within the more densely tangled regions, there was a mixture of straight and highly-bowed dislocation segments, suggestive of very fine obstacles pinning the structure. Further higher magnification TEM analysis revealed some small (10-50 nm diam.) and many ultrafine (3-5 nm diam.) precipitates along dislocations and in the matrix. Similar particles were seen along the grain boundaries as well (Fig. 8). AEM analysis

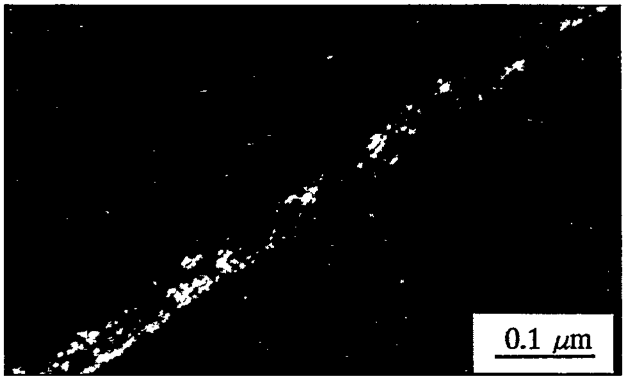

Fig. 8. Darkfield transmission electron micrograph showing fine grain boundary precipitates.

of precipitates extracted on a replica made from this specimen indicated that the coarser precipitates and clusters were a mixture of Cr- and Fe-rich M_7C_3 and more Nb-rich and Zr-rich MC particles which also contained some Mo, Cr, and Fe. Smaller (40-60 nm) particles found on the replica contained varying combinations of Cr, Fe, Nb, and Mo. The ultrafine precipitates were not detected on the replica and were too small for XEDS analysis within the foil. Work continues to examine additional creep-tested specimens and to identify these ultrafine precipitates.

From all this data, two points needing discussion emerge: (a) the mechanisms causing the effect of solution-annealing temperature on creep strength and rupture resistance in this particular complex Fe_3Al alloy and (b) the cause of the unusual behavior of grain size with increasing annealing temperature at 1100-1225°C. It appears that both (a) and (b) are related to precipitation behavior during solution-annealing, including both dissolution of some of the coarser precipitates present from prior hot processing and the formation of new dispersions of fine precipitates either during annealing or afterwards during cooling or creep. The TEM evidence clearly indicates that fine matrix precipitates were present only in the specimen heat-treated at 1150°C, and that more fine precipitates formed during creep at 593°C, both in the matrix and at the grain boundaries. Such precipitation would tend to stabilize the microstructure and produce the very low minimum creep rates observed in the specimens heat-treated at 1150-1175°C. Despite the lower values of creep strain, a precipitate-dislocation pinning mechanism would also enable ductile fracture to occur, as was observed in this study. Coarser grain size in the annealed specimens would also contribute to increased creep-rupture strength. The lack of creep-rupture strength observed after annealing at 1225°C, which did produce grain boundary precipitation, also argues for the dominant role of precipitate-dislocation pinning in the creep-strengthing produced by annealing at 1150-1175°C.

The unusual grain size behavior with annealing temperature appeared to be caused by grain boundary precipitation retarding grain growth at 1225°C relative to more normal grain growth behavior at 1100-1175°C. This precipitation is assumed to have been caused by the dissolution and reprecipitation of coarse higher-melting-temperature carbides of niobium and zirconium. Annealing at 1100°C caused no dissolution of coarse precipitates, as evidenced by the lack of fine precipitation after annealing and microstructural deformation during creep. Annealing at 1150°C caused some dissolution of coarser precipitates, because fine precipitates formed uniformly in the as-heat-treated specimen, as well as during creep-testing at 593°C. Annealing at 1225°C appeared to produce more dissolution, because new precipitates formed along the grain boundaries and some additional coarser precipitates (most likely involving other elements like Cr, Fe and Mo) were found.

CONCLUSIONS

The results of creep-rupture tests on an Fe_3Al-based alloy containing additions of Nb, Mo, Zr, B, and C showed that significant increases in creep life can be produced through microstructural control. A heat treatment of 1 h at 1150°C produced over 2700 h of creep life in a specimen tested at 593°C under a stress of 207 MPa, whereas the same material heat treated at 750°C and similarly tested lasted only 100 h. Correlation of optical and TEM microstructural analysis indicated that fine precipitation pinning of matrix dislocations was the main strengthening mechanism. Examination of as-heat-treated control specimens indicated that the strengthening was associated with the dissolution of coarse carbides at

1150°C and reprecipitation of fine precipitates which then pinned dislocations.

ACKNOWLEDGEMENTS

Research sponsored by the U.S. Department of Energy, Fossil Energy AR&TD Materials Program and by the Assistant Secretary for Energy Efficiency and Renewable Energy, Office of Industrial Technologies, Advanced Industrial Materials (AIM) Program under contract DE-AC05-84OR21400 with Martin Marietta Energy Systems, Inc.

REFERENCES

1. C. G. McKamey, P. J. Maziasz, and J. W. Jones, "Effect of Addition of Molybdenum or Niobium on Creep Rupture Properties of Fe_3Al," J. Mater. Res., 7(8) (1992), 2089-2106.

2. C. T. Liu, C. G. McKamey, and E. H. Lee, "Environmental Effects on Room-Temperature Ductility and Fracture in Fe_3Al," Scripta Metall. Mater., 24(2) (1990), 385-90.

3. C. T. Liu and C. G. McKamey, "Environmental Embrittlement-A Major Cause for Low Ductility of Ordered Intermetallics," High Temperature Aluminides and Intermetallics, ed. S. H. Whang, C. T. Liu, D. P. Pope, and J. 0. Stiegler, (Warrendale, PA: The Metallurgical Society, 1990), 133-151.

4. P. F. Tortorelli and J. H. DeVan, "Behavior of Iron Aluminides in Oxidizing and Oxidizing/Sulfidizing Environ ments," Mat. Sci. & Eng., A153 (1992), 573-77.

5. C. G. McKamey and C. T. Liu, "Environmental Embrittlement of Iron Aluminides in Moisture-Containing Atmospheres," Proceedings of ADVMAT/91, First International Symposium on Environmental Effects on Advanced Materials, edited by R. D. Kane, (Houston, TX: NACE, 1992), paper no. 17-1.

6. V. K. Sikka, "Ductility Enhancement of Iron-Aluminide Alloys," SAMPE Quart., 22(4) (1991), 2-10.

7. V. K. Sikka, S. Viswanathan, and C. G. McKamey, "Development and Commercialization Status of Fe_3Al-Based Intermetallic Alloys," Structural Intermetallics, eds. R. Darolia, J. J. Lewandowski, C. T. Liu, P. L. Martin, D. B. Miracle, and M. V. Nathal, (Warrendale, PA: The Metallurgical Society, 1993), 483-91.

8. C. G. McKamey, J. H. DeVan, P. F. Tortorelli, and V. K. Sikka, "A Review of Recent Developments in Fe_3Al-Based Alloys," J. Mater. Res., 6(8) (1991), 1779-1805.

9. P. J. Maziasz and C. G. McKamey, "Microstructural Characterization of Precipitates Formed During High-Temperature Testing and Processing of Iron-Aluminide Alloys," Mater. Sci. & Eng., A152 (1992), 322-34.

10. D. M. Dimiduk, M. G. Mendiratta, D. Banerjee, and H. A. Lipsitt, "A Structural Study of Ordered Precipitates in an Ordered Matrix within the Fe-Al-Nb System," Acta Metall., 36 (1988), 2947-58.

11. J. R. Knibloe, R. N. Wright, and V. K. Sikka, "Microstructure and Mechanical Properties of P/M Fe_3Al Alloys," 1990 Advances in Powder Metall, Vol. 2 (Princeton, NJ: Metal Powder Industries Federation, 1990), 219-31.

12. P. J. Maziasz, C. G. McKamey, and C. R. Hubbard, "Designing Precipitation-Strengthened Iron-Aluminides for High-Temperature Applications," Alloy Phase Stability and Design, eds. G. M. Stocks, D. P. Pope, and A. F. Giamei (Pittsburgh, PA: Materials Research Society, 1990), 349.

13. C. G. McKamey, P. J. Maziasz, G. M. Goodwin, and T. Zacharia, "Effects of Alloying Additions on the Microstructures, Mechanical Properties, and Weldability of Fe_3Al-Based Alloys," Mat. Sci. & Eng., A174 (1994), 59-70.

14. C. G. McKamey, unpublished results.

15. J. A. Horton, C. T. Liu, and C. C. Koch, "Alloying Effects and Microstructure of Iron Aluminides," High-Temperature Alloys: Theory and Design, eds. J. O. Stiegler (Warrendale, PA: The Metallurgical Society, 1984), 309-21.

IN-SITU FIRESIDE CORROSION TESTING

J. L. Blough
M. T. Krawchuk
S. F. Van Weele

Foster Wheeler Development Corporation
12 Peach Tree Hill Road
Livingston, NJ 07039

ABSTRACT

A variety of developmental and commercial tubing alloys and claddings has previously been exposed to laboratory fireside corrosion testing simulating a superheater or reheater in a coal-fired boiler. This program will expose 347, RA-85H, HR-3C, 253MA, Fe_3Al + 5Cr, 310 modified, NF-709, 690 clad, and 671 clad samples to the actual operating conditions of a 250-mW coal-fired boiler. The samples will be installed on an air-cooled, retractable corrosion probe, installed in the reheater cavity, controlled to the operating metal temperatures of an existing and advanced-cycle coal-fired boiler and exposed for 4000, 12,000, and 16,000 hours of operation. After the various exposures, the samples will be metallurgically examined to determine the wastage rates and mode of attack.

The final design of the 2-temperature zone probe has been completed, and the samples are being prepared for fabrication of the probe.

INTRODUCTION

In the first half of this century, advances in fossil-fuel-fired power systems technology evolved gradually, setting the groundwork for the explosion of technology that occurred in the second half. Steam temperatures rose an average of 6.6°F/y from 1903 to about 621°C (1150°F) in 1955. However, the excursion above 538°C (1000°F) was short-lived; by 1960 most steam generators were designed for 565°C (1049°F), and by 1970 they were back to 538°C (1000°F). There are several reasons for this regression; one is a materials problem that has defied a technical or economic solution. There are materials available with strength to withstand higher temperatures and pressures; but in the environment of a conventional furnace, the integrity of the material can be affected by the quality of the coal being burned and the corrosive nature of the slag.

High-temperature fireside metal wastage in conventional coal-fired steam generators can be caused by gas-phase oxidation or liquid-phase coal-ash corrosion. Gas-phase oxidation is usually not a problem if tube and support materials are selected for their oxidation resistance at operating temperatures and for spalling, flaking, or other reactions to their environment. Coal-ash corrosion, on the other hand, usually results in accelerated attack and rapid metal wastage—even of stainless steels. The cause of this type of corrosion is generally accepted as the presence of liquid sulfates on the surface of the metal beneath an overlying ash deposit[1-4]. Approaches to solving this problem have included changing the fuel or providing protective baffling with sheaths of corrosion-resistant material around selected tubes. In some cases, metal temperatures have been lowered. Another approach has been the replacement of sections of tubing with more corrosion-resistant materials or with duplex tubing—a conventional core alloy with good high-temperature strength and an outer surface of a more corrosion-resistant material. Selectively applied, these methods have minimized problem in units burning mildly corrosive coal. Sprayed metal coatings and ceramic coatings have generally been unsuccessful, showing spalling, erosion, and rapid deterioration.

There have been a number of literature reviews and recent updates discussing the variables affecting the corrosion mechanism[5-7]. Additionally, two sizeable research projects were conducted—one a laboratory and in-situ field testing at three utilities of commercially available alloys[8-9] and the program that is the basis for this paper (ORNL-FW2), combining laboratory and field testing to more completely cover the controlling variables for a longer duration[10].

Fireside corrosion increases substantially with rising temperatures, up to a maximum level; then it drops above 725 to 740°C (1337 to 1364°F), assuming the coals used are high in alkali and iron and low in calcium and magnesium. The attack may be delayed or erratic for various reasons. However, when firing the more aggressive coals such as Illinois No. 6, the more susceptible stainless steels cannot be used reliably in improved coal-fired power plants to achieve 1101°C (594°F) steam. A review of available data on fireside corrosion proves that, among the widely used alloys, the variation in corrosion as coal composition changes is more significant than the effect of alloy composition[6]. When any one of the ingredients of the corrosive process is removed, metal loss is greatly reduced. As a result a number of investigators have prepared corrosivity indices that are functions of the impurities in the coal[11-12].

While substantial progress has been achieved through laboratory testing, actual utility service exposures are evidently necessary to verify any conclusions drawn from laboratory testing. A number of important environmental parameters cannot be fully simulated in the laboratory[9]:

- The actual composition of the deposits formed on the tubes is more complex than the composition of the simulated ash.
- The SO_3, formed by heterogeneous reaction on cooled surfaces, is variable.
- Very large temperature gradients occur within the ash deposits.
- The ash and fuel gas move past tubes at high velocity; the rate varies with design.

- The composition of the corrosive deposits changes with time.
- Temperatures are not constant.
- Fly-ash erosion removes the protective oxides; fresh aggressive sulfate ash replenishment results.

PHASE I RESULTS

In Phase I of this ORNL program, "Fireside Corrosion Testing of Candidate Superheater Tube Alloys, Coatings, and Claddings," 20 commercial and developmental alloys were evaluated[10]. The coupons of the metals were exposed to synthetic coal ash and synthetic flue gases at 650 and 700°C (1202 and 1292°F) for up to 800 hours.

Chromium content was found to be the largest factor in determining the resistance of an alloy to liquid coal-ash corrosion. For stainless steels and nickel alloys, additions of chromium up to 25 percent provide increased resistance to coal-ash attack; however, above the 25-percent chromium level, there does not appear to be any added benefit from more chromium, possibly because of the higher nickel content of those alloys. Silicon and aluminum were also beneficial, but to a lesser extent. The iron aluminide intermetallics also show a chromium dependence. Aluminides containing 5-percent chromium performed markedly better overall than those containing 2-percent chromium. The more resistant alloys show lower corrosion rates at longer exposure times, indicating the formation of a passive layer; the less-resistant alloys exhibit increasing corrosion rates at longer exposures.

Average thickness loss rates for a selection of alloys exposed at 650 and 700°C (1202 and 1292°F) are shown in Figure 1. Lower-chromium alloys generally suffered greater wastage rates at the higher testing temperature [700°C (1292°F)], while higher-chromium alloys suffered the same amount of wastage at 650 (1202) as at 700°C (1292°F). Note that the corrosion rates of the alloys drop as the chromium content increases, illustrating the beneficial effect of chromium. The exception is the reduced corrosion rate of the 5-percent chromium in the iron-aluminide matrix.

Both the alkali content in the ash and SO_2 concentration in the flue gas affect the corrosivity of the alkali-iron trisulfates in the ash layer. As Figures 2 and 3 show, an increase in either results in a more corrosive environment and higher wastage rates.

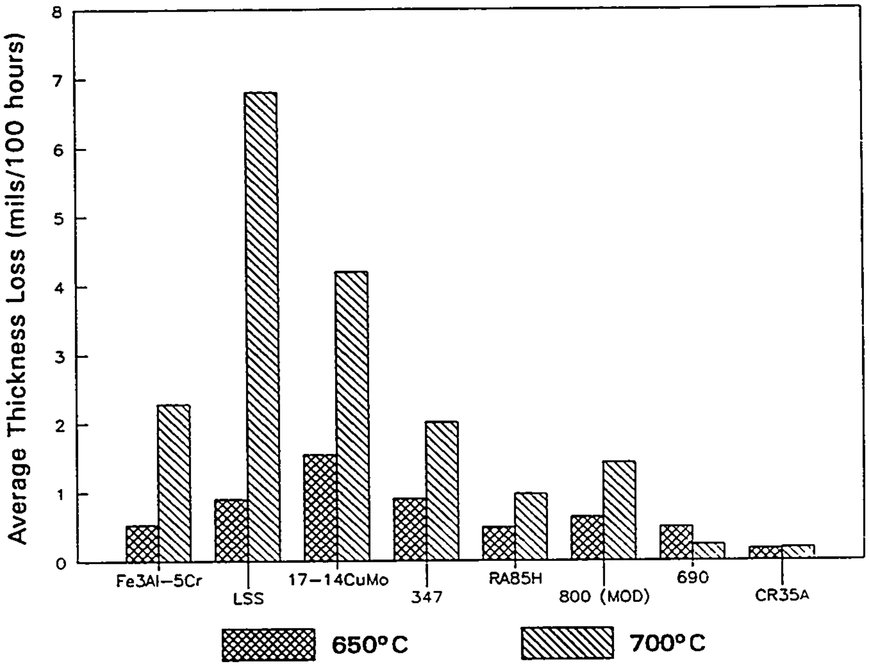

Fig. 1. Average thickness loss rates of representative alloys coated with ash containing 10 wt% alkali sulfates and exposed at 650 (1202) and 700°C (1292°F) for 800 hours to flue gas containing 1.0 vol% SO_2

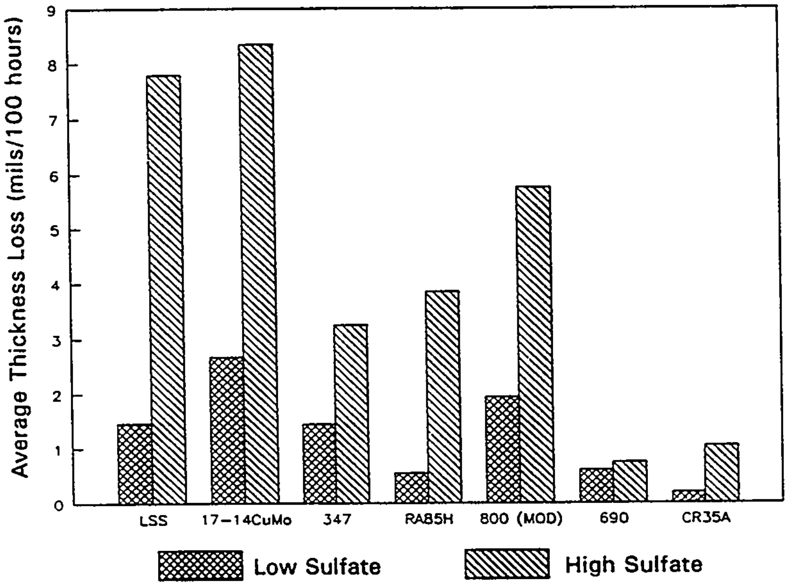

Fig. 2. Average thickness loss rates of representative alloys coated with ash containing either 10 or 75 wt% alkali sulfates and exposed at 700°C (1292°F) for 200 or 800 hours respectively to flue gas containing 0.25 vol SO_2

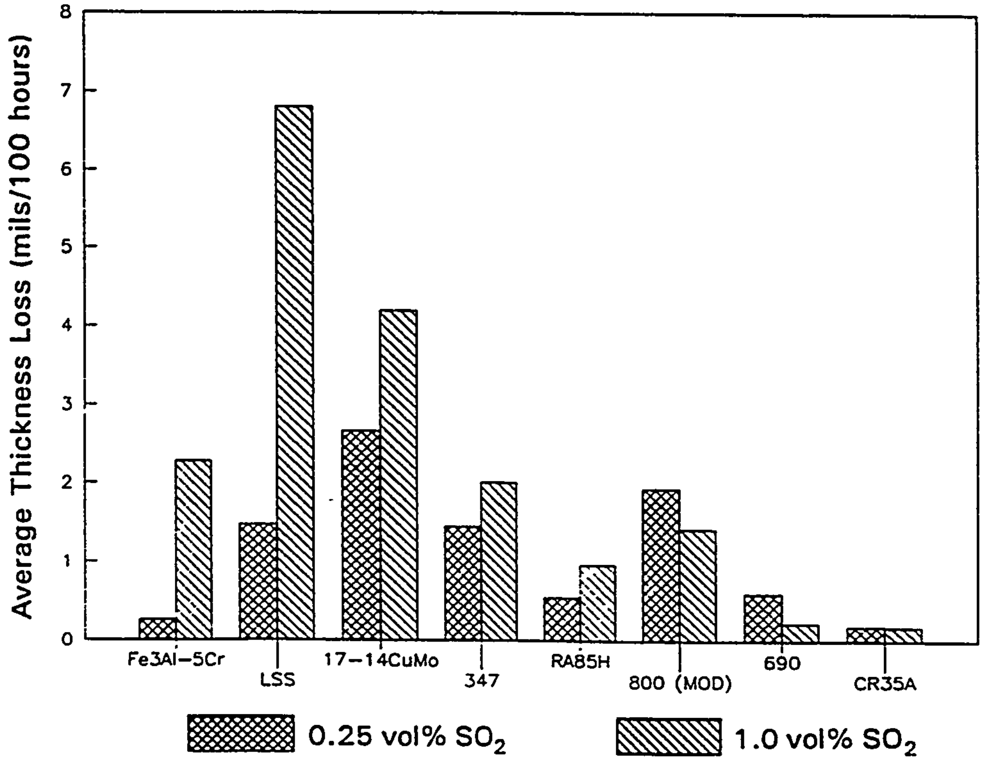

Fig. 3. Average thickness loss rates of representative alloys coated with ash containing 10 wt% alkali sulfates and exposed at 700°C (1292°F) for 800 hours to flue gas containing either 0.25 or 1.0 vol% SO_2

PHASE II CORROSION PROBE TESTING

In this project, the field tests will comprise corrosion probe testing, coal characterization, and deposit analysis. The coals and their deposits, which are formed on the tube surfaces, will be analyzed to provide fuel characterization, a deposit analysis data bank, and possibly a corrosivity index for predicting corrosivity under various combustion conditions. The equipment and the procedures for this phase have been previously used and perfected at three different utilities for over 3 years of in-situ testing at each station.

The utility for test exposures should be burning an aggressive fuel to adequately evaluate the candidate alloys. The coal being burned at Tennessee Valley Authority's (TVA's) Gallatin Station had been previously analyzed, and numerous corrosion indices predicted high corrosivity in addition to the fact that installed T22 and Type 304SS tubing experienced about 7 years of life in the superheaters and reheaters of Units 1 and 2.

Selection of Materials for Corrosion Probes

Foster Wheeler Development Corporation (FWDC) laboratory-tested 20 different materials[10]. Because this quantity was impractical from both an economic and a probe-length standpoint, fewer (the nine listed in Table 1) had to be selected for the field tests. These materials provide a range of compositions and cost for both the commercially available and developmental alloys and claddings.

Table 1 Chemical Composition of Candidate Alloys (%)

Alloy	Cr	Ni	Others
Type 347	17-19	9-13	(Nb + Ta) = 10 × C (min.)
85 H	18	15	Al = 1, Si = 3.9
NF 709	20	25	Mo = 1.5, Mn = 1.0, Si = 0.6
690 Clad	30	58	
671 Clad	48	52	
Fe_3Al + 5% Cr	5	---	Al = 17
HR-3C	25	20	Nb = 0.4
253 MA	21	11	Si = 1.7
Modified 310	25	20	Modified

Field Corrosion Probe Design

The corrosion probes are being designed to provide realistic exposures of metal samples to both actual boiler environments and also at the higher anticipated metal temperatures of an advanced plant. The parameters are independence from the main boiler, removal without a boiler outage, and a fail-safe design, one that removes the probe from the boiler if there are any malfunctions. With these features, years of testing will not be compromised with a sudden system overheating.

The probes will be exposed for 4000, 12,000, and 16,000 hours. This will be accomplished by utilizing two probe test locations. At one test location, the probe will be exposed for

16,000 hours. At the other test location, the probe will be removed after 4000 hours and a new probe inserted for the remaining 12,000 hours.

Each probe is a 2.56-m (8.4-ft)-long, 60.20-mm (2.37-in.)-OD tube that will extend into the furnace for approximately 2.3 m (7.6 ft). Ring samples [38.1 mm (1.5 in.) wide] of the candidate alloys listed in Table 1 will be installed at the end of the probe farthest from the furnace wall. The probe is cooled by air that flows in the annular region between the probe tube ID and the tapered inner tube OD. The tapered inner tube is designed to obtain two bands of temperature on the outer surface of the samples. The alloy samples will be duplicated in such a manner as to expose each alloy to a temperature in each of the temperature bands [643 to 677°C (1190 to 1250°F) and 677 to 710°C (1250 to 1310°F)].

Each probe will have a retraction mechanism, and three K-type thermocouples in duplicate to monitor the mean tube wall at the beginning and end of each test section group. A 6.35-mm (1/4-in.) sheathed thermocouple will be mounted on the OD of one of the corrosion probes in each set to measure flue gas temperature. Each probe has its own cooling-air control valve.

The control system monitors the selected control thermocouple and modulates the airflow to maintain an average surface metal temperature for each temperature band. The probes retract automatically if failure of the cooling-air supply system or any other malfunction (instrument signal, power failure, or computer failure) causes the probe temperature to exceed the set limit of 746°C (1375°F) for 2 minutes. FWDC personnel access the field computer automatically for probe status and temperature data each morning at 6 a.m. or manually through its modem.

The locations at each plant were chosen because of cavity access and because they best represent the locations for the finishing superheater outlet tube legs on the "Advanced Cycle" unit.

The ideal coal-ash corrosion probe exposure would have been realized if only one coal were being burned at each plant. This practice is not common at many utilities; in fact, many are buying coal on the spot market. Gallatin burns a number of eastern high-sulfur coals, mainly Island Creek, Warrior, Dotiri, and Pattiki, which are known to be corrosive and prone to alkali-iron-trisulfate formation. The Borio Index for these coals typically range from 2.0 to 4.1, and the chloride level is 450 to 3000 ppm.

Post-Exposure Analysis

Quarterly Examinations

During the quarterly inspections, FWDC personnel at the site will manually retract the probes, selectively remove deposits, and make ultrasonic wall thickness measurements on the "A" samples of the probe set.[*] The "B" probe will be left untouched at this time. The quarterly inspections will provide preliminary nondestructive corrosion data before the three destructive examinations. With these data, corrosion can be tracked, and a total loss of data can be avoided if there is a catastrophic failure. The automatic retraction feature, if cooling air is lost and test specimen temperatures become excessive, minimizes the possibility of such a catastrophic failure.

The laboratory analysis of the removed deposits at FWDC will characterize the composition and determine whether alkali sulfates are present and aid in interpreting the effect of fuel changes on coal-ash corrosion.

Destructive Testing

At 4000; 12,000; and 16,000 hours, probes (A-1," "A-2," and "B" respectively) will be removed and sent to FWDC for metallurgical evaluation, which includes:

- Visual examination and selective photographic documentation
- Selective removal of deposits
- Disassembly of probes
- Cutting of two transverse sections through the center of the ring sample
- Retention of half the transverse section as mounted for wall thickness measurements. Selective cutting of the other half section for microscopic and SEM/EDX examination
- Light grit blasting and NaOH cleaning of one transverse ring section of each sample
- Visual examination of the cleaned samples
- Wall thickness measurements at 45-deg points or maximum loss areas on the leading 180-deg side of cleaned samples
- Mounting of the uncleaned ring samples removed from in the as-exposed condition to retain the scale/deposit during future cutting
- Microscopic measurement of the sound metal in the mounted samples and calculation of total metal loss
- Selective SEM/EDX examination.

---

[*] To aid in describing the operations, "A" (inspected quarterly) and "B"(untouched) have been assigned to the two probes in a set. The operations will be performed on the "A" or "B" probes in each 4000-, 12,000-, and 16,000-hour exposure set.

Output

The outcome of the metallurgical examination will be the quantitative measurement and qualitative characterization of the corrosion process occurring on the test materials. These field-obtained corrosion tests will be correlated with the laboratory corrosion exposures from Phase I.

REFERENCES

1. W. Nelson and C. Cain, Jr., "Corrosion of Superheaters and Reheaters of Pulverized-Coal-Fired Boilers," *Transactions of the ASME, Journal of Engineering for Power,* July 1960, pp. 194-204.

2. W. T. Reid, "Formation of Alkali Iron Trisulphates and Other Compounds Causing Corrosion in Boilers and Gas Turbines," Project Review July 1, 1966-June 30, 1968, prepared by Battelle Memorial Institute, Columbus, OH, June 1968.

3. W. T. Reid, *External Corrosion and Deposits: Boilers and Gas Turbines,* American Elsevier Publishing Company, New York, 1974.

4. G. J. Hills, "Corrosion of Metals by Molten Salts," *Proceedings of the Marchwood Conference: Mechanism of Corrosion by Fuel Impurities,* Johnson and Littler, eds., Butterworths, London, 1963.

5. I. M. Rehn, "Fireside Corrosion of Superheater and Reheater Tubes," Palo Alto, CA: Electric Power Research Institute, 1980. CS-1653.

6. I. M. Rehn, "Fireside Corrosion of Superheater Alloys for Advanced Cycle Steam Plants," Palo Alto, CA: Electric Power Research Institute, 1987. EPRI 5195.

7. S. Van Weele and J. L. Blough, "Literature Search Update—Fireside Corrosion Testing of Candidate Superheater Tube Alloys, Coatings, and Claddings," Livingston, NJ: Foster Wheeler Development Corporation, September 1990. FWC/FWDC/TR-90-11.

8. W. Wolowodiuk, S. Kihara, and K. Nakagawa, "Laboratory Coal Ash Corrosion Tests," Palo Alto, CA: Electric Power Research Institute, July 1989. GS-6449.

9. J. L. Blough, G. J. Stanko, M. Krawchuk, W. Wolowodiuk, and W. Bakker, "In-Situ Coal Ash Corrosion Testing for 2 Years at Three Utilities," International EPRI Conference on Improved Technology for Fossil Power Plants New and Retrofit Applications, Washington, DC, March 1-3, 1993.

10. S. Van Weele and J. L. Blough, "Fireside Corrosion Testing of Candidate Superheater, Tube Alloys, Coatings, and Claddings," Livingston, NJ: Foster Wheeler Development Corporation, August 1991. ORNL/SUB/89-SA187/02.

11. R. W. Borio and R. P. Hensel, "Coal-Ash Composition as Related to High-Temperature Fireside Corrosion and Sulfur-Oxides Emission Control," *Transactions of the ASME, Journal of Engineering for Power,* Vol. 94, 1972, pp. 142-148.

12. J. Shegeta, et al., "Development of a Coal Ash Corrosivity Index for High Temperature Corrosion," 1986. ASME 86-JPGC-FACT-3.

13. S. Kihara, K. Nakagawa, A. Ohtomo, H. Aoki, and S. Ando, "Simulating Test Results for Fireside Corrosion of Superheater & Reheater Tubes Operating at Advanced Steam Conditions in Coal-Fired Boilers, *High Temperature Corrosion in Energy Systems,* TMS/AIME, M. F. Rothman, ed., 1984, pp. 361-376.

14. W. Wolowodiuk, et al., "Coal-Ash Corrosion Investigations," *Proceedings of the First International Conference on Improved Coal-Fired Power Plants.* Palo Alto, CA: Electric Power Research Institute, November 1986.

15. J. L. Blough, M. T. Krawchuk, G. J. Stanko, and W. Wolowodiuk, "In-Situ Coal Ash Corrosion Probe Testing," to be published.

16. J. L. Blough and W. T. Bakker, "Measurement of Superheater Corrosion Caused by Molten Alkali Sulfates," First International Conference on Heat-Resistant Materials, to be presented at the ASM International, Lake Geneva, WI, September 22-26, 1991.

17. T. Hammond, W. Wolowodiuk, J. L. Blough, J. Brooks, "Replacement of Reheater at TVA's Gallatin Station Unit 2," presented at the Third International Conference on Improved Coal-Fired Power Plants (ICPP), San Francisco, April 1991.

18. R. W. Borio and R. P. Hensel, "Coal-Ash Composition as Related to High-Temperature Fireside Corrosion and Sulfur-Oxides Emission Control," *Transactions of the ASME, Journal of Engineering for Power,* Vol. 94, 1972, pp.142-148.

TENSILE PROPERTIES OF AS-CAST Fe_3Al-BASED ALLOYS

S. Viswanathan, C. G. McKamey, and P. J. Maziasz

Oak Ridge National Laboratory
Metals and Ceramics Division
P.O. Box 2008
Oak Ridge, TN 37831

ABSTRACT

Room-temperature tensile properties of as-cast Fe_3Al-based FA-129 alloy were investigated. Tensile properties were obtained in the as-cast condition in air, oxygen, and water-vapor environments, and after homogenization at 700, 900, and 1200°C. Transmission electron microscopy (TEM) was used to characterize ordered phases and dislocation structure, and optical metallography and scanning electron microscopy (SEM) were used to characterize the grain microstructure and fracture morphology. Tensile properties in the as-cast condition exhibited an environmental effect; tensile ductilities in oxygen atmosphere were greater than those obtained in laboratory air. Homogenized samples of FA-129 alloy exhibited almost twice the ductility found in the as-cast condition. Microstructural characterization of the homogenized samples and comparison of the as-cast and homogenized microstructures provided clues that helped to explain the poor ductility in the as-cast state.

INTRODUCTION

In recent years, alloys based on Fe_3Al have received considerable attention due to their wear, oxidation, and sulfidation-resistance properties.[1-4] However, the bulk of the work, involving both alloy development and studies on their corrosion, deformation, and fracture behavior, have been on samples in the wrought condition.[1-4] Before iron-aluminide alloys can be developed for structural applications on a large scale, it is important to characterize the as-cast microstructure and mechanical properties of iron-aluminide alloys, both from the view of further processing and for use as cast components. The first phase of this research characterized the various components of cast structure in FA-129 alloy.[1,2] This phase of the research characterized the as-cast mechanical properties of Fe_3Al-based alloys. Room-temperature tensile properties of as-cast Fe_3Al-based FA-129 alloy were investigated in air, oxygen, and water-vapor environments. Room-temperature tensile properties of FA-129 alloy are also investigated after homogenization at 700, 900, and 1200°C. Finally, tensile properties are correlated with the microstructure and fracture morphology, and some observations are made about tensile properties, in particular, the ductility in the as-cast condition.

DISCUSSION OF CURRENT ACTIVITIES

Experimental Procedure

Vacuum-induction melts of Fe_3Al-based FA-129 alloy (Fe-28% Al-5% Cr-0.5% Nb-0.2% C) were prepared (all weights indicated are in atomic percent and refer to nominal compositions) and cast into graphite molds of dimensions 25 × 150 × 100 mm or 32 × 180 × 110 mm (see Fig. 1). Coupons (15 × 15 × 89 mm) machined from the first ingot were homogenized at 700, 900, and 1200°C for 1h and air-cooled, and undersized tensile specimens (6.4 mm diam by 25.4 mm gauge length) were machined from the coupons. All homogenized specimens were tested in laboratory air. From undersized specimens machined from the second ingot, two specimens each were tested in water-vapor environments (water-vapor pressure corresponding to water at room temperature and 0.01 or 0.05 MPa total pressure), in oxygen environment (0.07 MPa pressure), and in laboratory air (30% humidity). Screw-driven Instron test machines were used for all tensile tests, and tests were conducted at room temperature and at a strain rate of 0.003 s^{-1}.

Tensile Properties of As-Cast Alloys

Figure 2 compares tensile properties for tests conducted in air, oxygen, and water-vapor environments. The alloy exhibited similar strength values in air and water-vapor environments, approximately 200 MPa for yield strength and 300 MPa for ultimate tensile strength. Ductility values, as measured by total elongation, are also similar, and comparatively low, about 1.5%, although values in the water-vapor environment were marginally lower than those in air. In the oxygen environment, the alloy exhibited yield strength very similar to that in air and water-vapor environments. However, both ultimate tensile strength at 400 MPa and total elongation at 3% were significantly higher in the oxygen environment. The results point to the existence of an environmental effect due to hydrogen present in water vapor, and parallel those obtained earlier for wrought materials.[4]

ORNL-DWG 94-10713

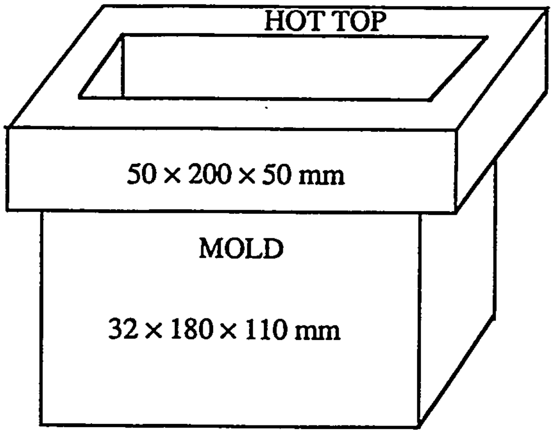

Fig. 1. Dimensions of graphite mold used for iron-aluminide alloy ingots.

ORNL-DWG 94-10714

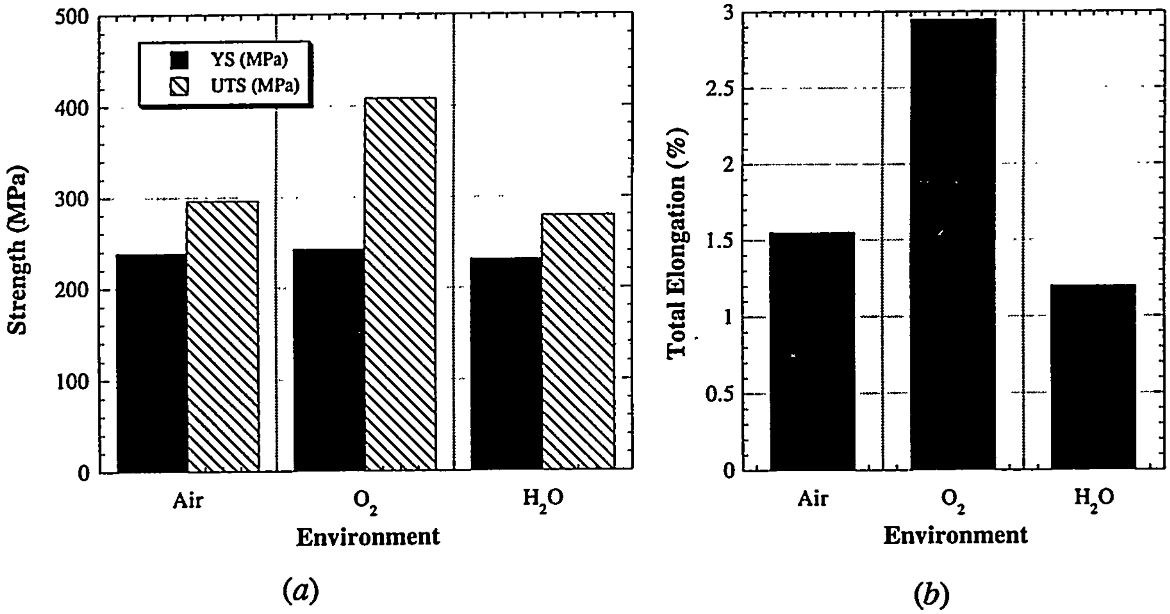

(*a*)

(*b*)

Fig. 2. Room-temperature tensile properties in air, oxygen, and water vapor environments for FA-129 alloy: (*a*) yield and ultimate tensile strength, and (*b*) total elongation.

Figure 3 shows tensile properties for samples homogenized at 700, 900, and 1200°C for 1 h. The yield strength increases with homogenization temperature, possibly due to niobium going into solution. Ultimate tensile strength and total elongation are also higher in the homogenized condition than in the as-cast condition, exhibiting a maximum at a homogenization temperature of 900°C. Total elongation for the sample homogenized at 900°C is 3%, almost twice the total elongation obtained in the as-cast condition.

Microstructural Characterization

Tensile specimens were examined visually with a low-power microscope and the fracture behavior was characterized by scanning electron microscopy (SEM). In addition, samples were examined by transmission electron microscopy (TEM) in order to determine the fine-scale microstructure and the type and extent of ordered phases.

The fracture mode at room temperature was similar for the different heat treatments and also did not change when tests were conducted in different environments, including air, water vapor, and oxygen. SEM fractography indicated that the typical fracture mode for these specimens was a mixture of transgranular cleavage and intergranular failure. The typical fracture morphology is shown in Fig. 4. These results are similar to those found previously in a study of as-cast FA-129.[5] While homogenization heat treatments did not discernably affect the final failure mode, there did seem to be a measurable effect of these heat treatments on the propensity for secondary cracking along the specimen gauge surface away from the fracture area; homogenized specimens exhibited fewer secondary cracks along the gauge relative to the as-cast specimens. This does indicate that the heat treatments are reducing crack initiation somewhat, consistent with the observed increases in uniform elongation and ultimate tensile strength.

TEM studies of the finer scale microstructures of these specimens showed some small differences between the as-cast and the various heat treated specimens of FA-129, but not much differences between the various homogenization heat treatments. Figure 5 shows a typical comparisons of the as-cast material with a specimen heat treated at 900°C for 1h. The matrix of the as-cast material was entirely $D0_3$ phase, with a domain size range of 30 to 110 n [Fig. 5(*a*)]. The matrix of the homogenized specimens also appeared to be mainly the $D0_3$ phase, with a finer domain size (10 to 60 n) than the as-cast material [see Fig. 5(*b*)]. There was, however, no measurable difference in ABP structure among the various heat treatments. Both the as-cast and homogenized samples exhibited low

ORNL-DWG 94-10715

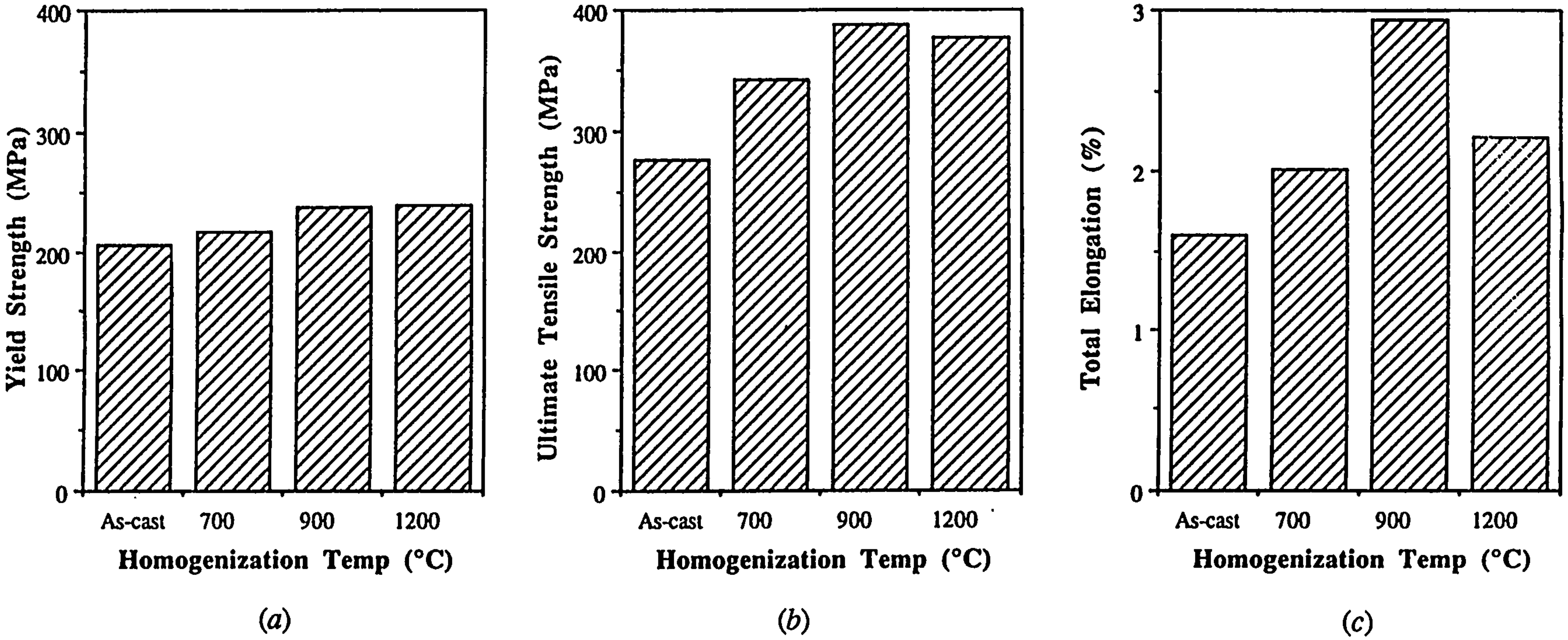

(*a*) (*b*) (*c*)

Fig. 3. Room-temperature tensile properties for FA-129 alloy tested in air, and after homogenization at 700, 900, and 1200°C: (*a*) yield strength, (*b*) ultimate tensile strength, and (*c*) total elongation.

ORNL-PHOTO 4871-94

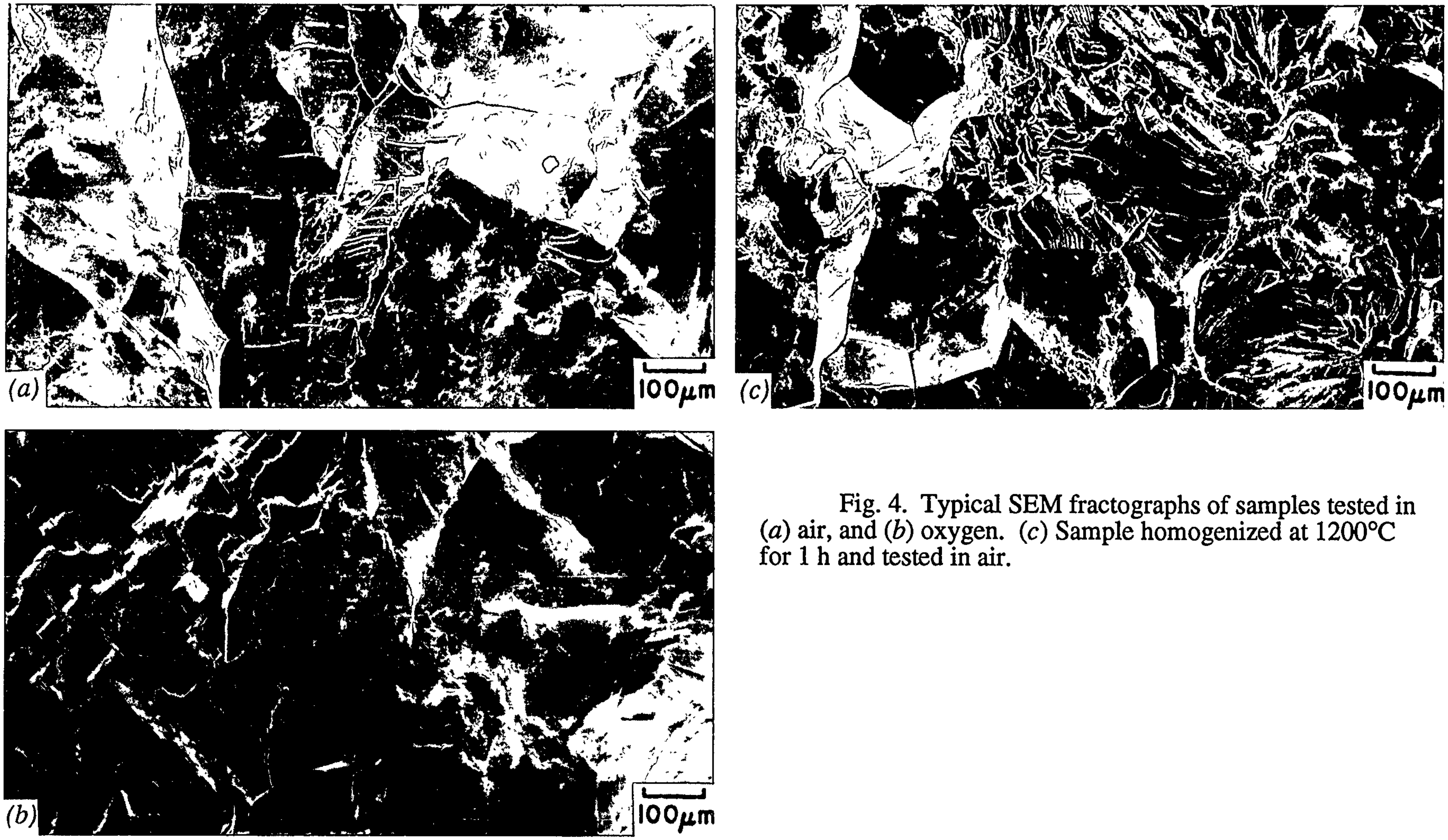

Fig. 4. Typical SEM fractographs of samples tested in (*a*) air, and (*b*) oxygen. (*c*) Sample homogenized at 1200°C for 1 h and tested in air.

ORNL-PHOTO 4872-94

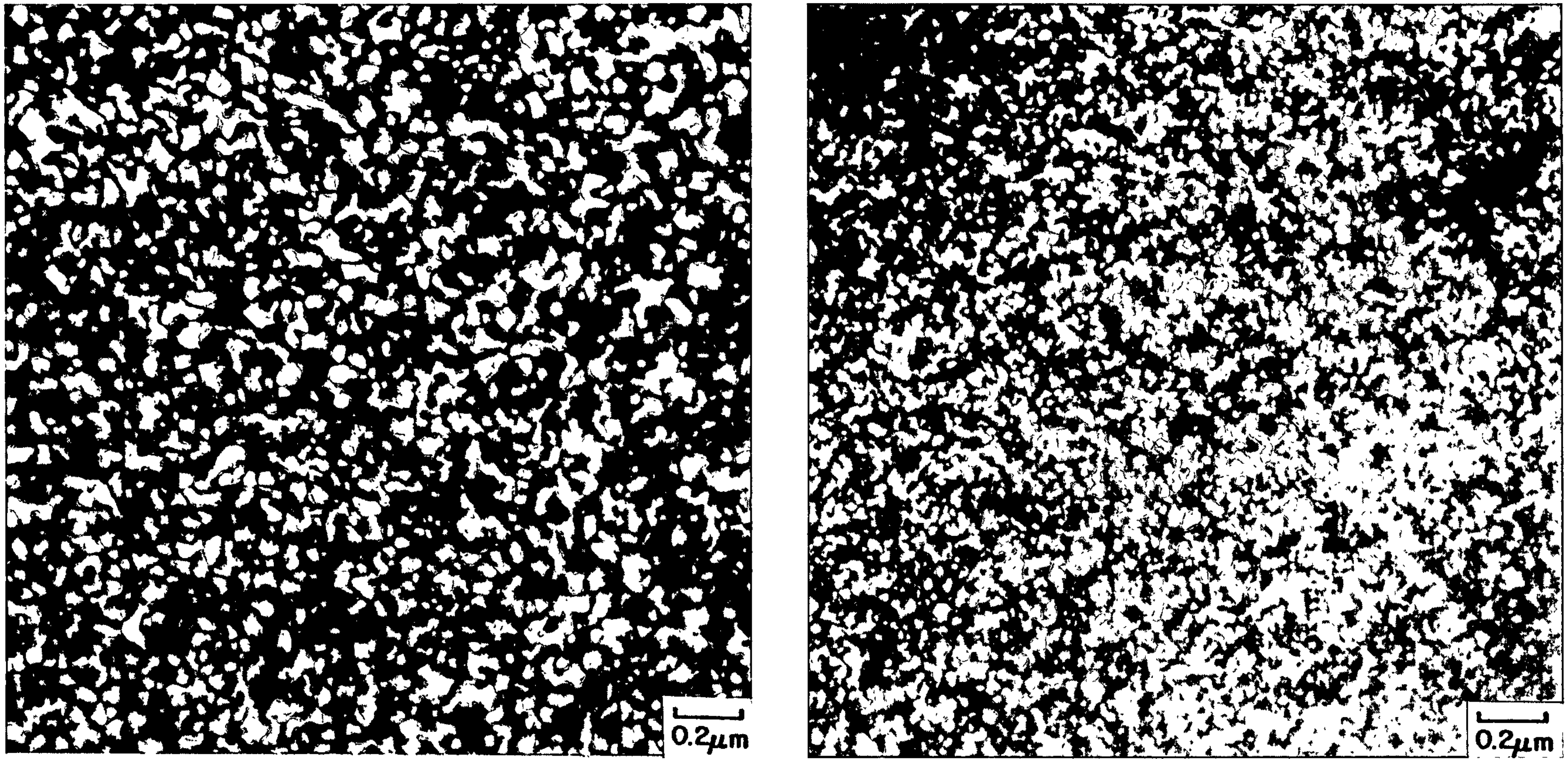

(*a*) (*b*)

Fig. 5. Transmission electron micrographs of as-cast FA-129 alloy illustrating typical dark-field image of antiphase boundaries separating $D0_3$ domains, in the (*a*) as-cast sample, and (*b*) material homogenized at 900°C.

dislocation densities (see Fig. 6). However, the as-cast material typically had a dislocation density that was nonuniform, with regions of loose dislocation networks, and large portions of grains without any dislocations [Fig. 6(*a*)]. Usually, the as-cast material had denser tangles of dislocations immediately adjacent to coarse NbC precipitate particles. There were also some minor differences in details of the dislocation structures between the as-cast and the various heat-treated specimens that may also be relevant to the differences found in mechanical properties. The as-cast material appeared to have a significant density of 4-fold superdislocations, with most segments being wavy and many of the partials showing some separation and slip-traces in the foil. By contrast, the heat-treated specimens, particularly those that were heat-treated at 700 and 900°C, showed mainly 2-fold superdislocations with straight, smooth segments [Fig. 6(*b*)]. While more work is needed to analyze these minor differences in detail, these preliminary observations could suggest a rationale for the observed mechanical properties differences.

Conclusions

There is a definite effect of heat-treatment that improves the ductility and ultimate tensile strength of the as-cast FA-129 iron-aluminide alloy. While heat-treatments for 1 h at 700, 900, and 1200°C all provide some margin of improvement, the largest effect is observed at 900°C. While heat-treatment does not affect the inherent fracture mode (transgranular cleavage and intergranular separation), it does reduce the propensity for secondary cracking along the gauge surface. Such an effect is consistent with better resistance to crack initiation, which is also consistent with increases in uniform plastic strain and ultimate tensile strength. TEM analysis of the fine-scale matrix microstructures of these specimens indicates that while heat-treatment does not radically change the microstructure, there are some observable differences between the heat-treated and as-cast microstructures that may ultimately help explain the mechanical properties differences. All of the heat-treated specimens have a finer $D0_3$ domain structure; furthermore, subtle detail differences (2-fold vs 4-fold superdislocations and residual stresses) in the microstructure may also contribute to the measured properties differences.

ORNL-PHOTO 4873-94

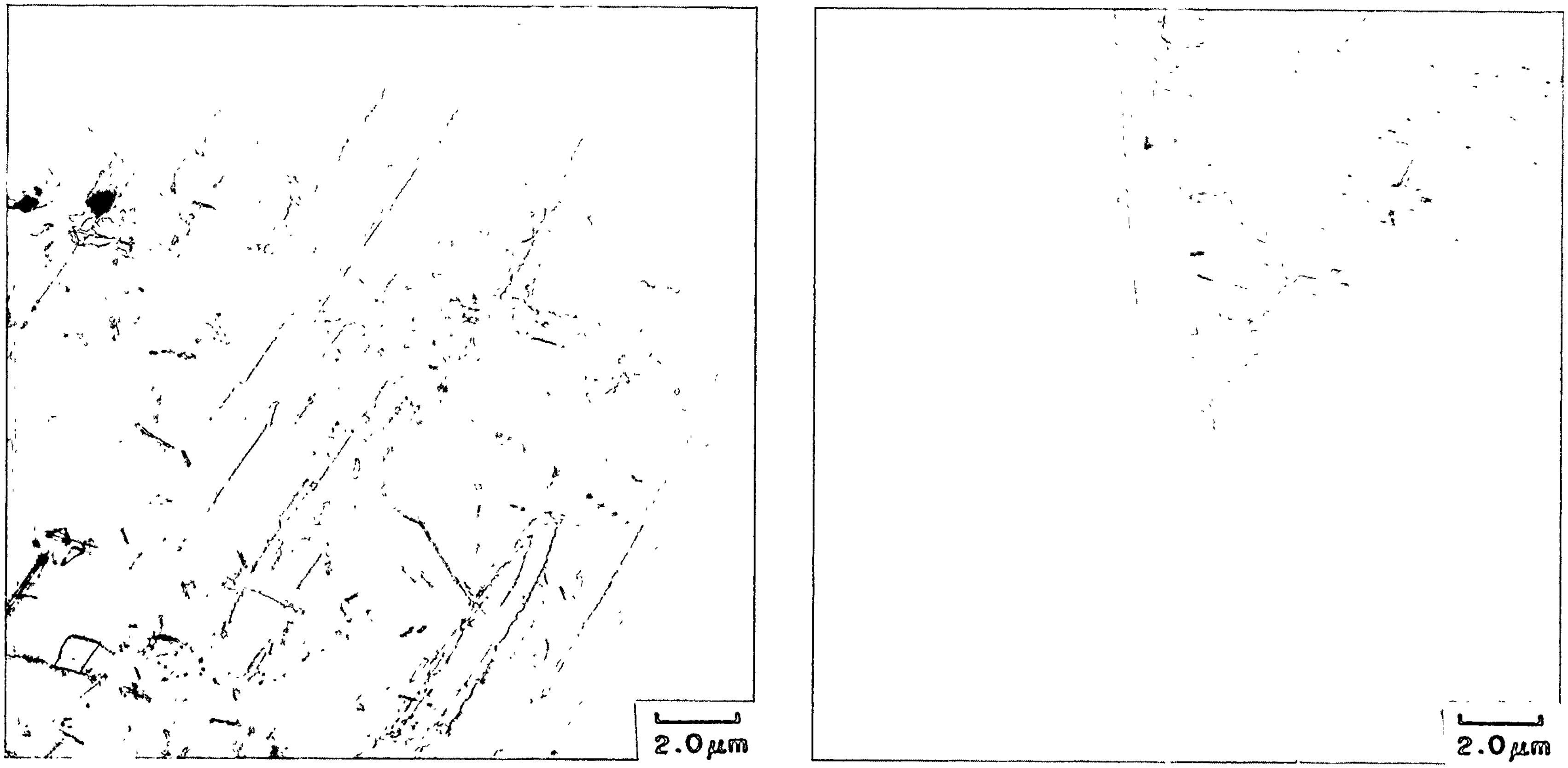

(*a*) (*b*)

Fig. 6. Transmission electron micrographs of as-cast FA-129 alloy illustrating dislocation densities in the (*a*) as-cast sample, and (*b*) material homogenized at 900°C.

ACKNOWLEDGMENTS

The authors thank C. R. Howell and R. H. Baldwin for tensile testing, K. B. Alexander and R. W. Swindeman for reviewing the manuscript, and M. L. Atchley and F. W. Christie for preparing the manuscript.

REFERENCES

1. S. Viswanathan, P. J. Maziasz, and V. K. Sikka, "Solidification Behavior of FA-129 Iron-Aluminide Alloy," p. 283 in *Proceedings of the Sixth Annual Conference on Fossil Energy Materials*, ORNL/FMP-92/1, Martin Marietta Energy Systems, Inc., Oak Ridge Natl. Lab., July 1992.

2. S. Viswanathan, P. J. Maziasz, and V. K. Sikka, "Solidification Behavior of Iron Aluminides," p. 293 in *Semiannual Progress Report, Fossil Energy AR & TD Materials Program*, ORNL/FMP-92/2, Martin Marietta Energy Systems, Inc., Oak Ridge Natl. Lab., December 1992.

3. C. G. McKamey, J. A. Horton, and C. T. Liu, "Effect of Chromium on Properties of Fe_3Al," *J. Mater. Res.*, **4**(5), 1156 (1989).

4. C. T. Liu, C. G. McKamey, and E. H. Lee, "Environmental Effects on Room-Temperature Ductility and Fracture in Fe_3Al," *Scr. Metall. Mater.*, **24**, 385 (1990).

5. S. Viswanathan, C. G. McKamey, P. J. Maziasz, and V. K. Sikka, "Tensile Properties of As-Cast Iron-Aluminide Alloys," p. 171 in *Proceedings of the Seventh Annual Conference on Fossil Energy Materials*, ORNL/FMP-93/1, Martin Marietta Energy Systems, Inc., Oak Ridge Natl. Lab., July 1993.

WELDABILITY OF IRON ALUMINIDES

G.M. Goodwin, P.J. Maziasz, C.J. McKamey, J.H. DeVan, V.K. Sikka

Oak Ridge National Laboratory
P.O. Box 2008
Oak Ridge, TN 37831-6096

ABSTRACT

Corrosion-resistant weldable iron aluminide alloys are being developed for weld overlay cladding of conventional steels and alloys and possible structural applications.

Weld hot cracking can be minimized by careful choice of alloying additions, and hot cracking resistance equivalent to commercial austenitic stainless steels has been achieved. Hydrogen-induced cold cracking, however, continues to be a problem with these alloys, both in monolithic weldments and weld overlay cladding applications.

We have found that preheat and postweld heat treatment can reduce hydrogen cracking, and that composition is also an important variable. Experiments in controlled atmospheres have confirmed that a major source of hydrogen is provided by the reduction of water vapor from the environment, and that oxygen helps to reduce cracking sensitivity.

Concurrently, we are developing filler metals using the aspiration-casting process, for use both as filler metals with the gas tungsten arc process, and as core wire for the production of shielded metal arc electrodes.

DISCUSSION OF CURRENT ACTIVITIES

Hot Cracking

Initially one of the commonly ocurring problems with these alloys, hot cracking is no longer considered to be a major concern. Certain compositional effects must, however, be kept in mind; carbon and boron are beneficial within limits, and niobium,, molybdenum, and zirconium can be deleterious at higher levels. Figure 1 summarizes sigmajig hot cracking, test results for a number of iron aluminide compositions, compared with similar data for other alloys. As noted from the figure, by careful selection and control of composition, we have been able to achieve hot cracking resistance equivalent to some commercial heats of austenitic stainless steels.

This research was sponsored by the Fossil Energy Advanced Research and Technology Development (AR&TD) Materials Program, U.S. Department of Energy, under contract DE-AC05-840R21400 with Martin Marietta Energy Systems, Inc.

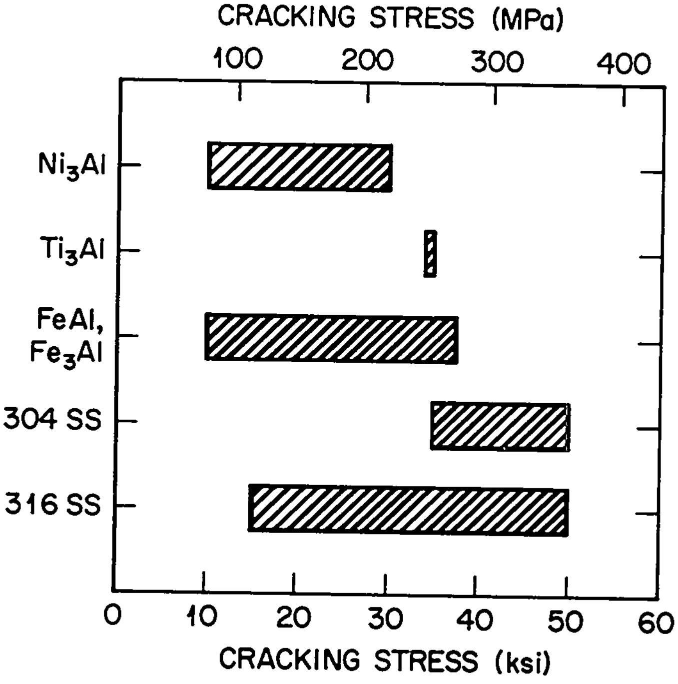

Fig. 1. Summary of sigmajig test results

Cold Cracking

Hydrogen induced cold cracking continues to be a problem with these alloys; we are studying cold cracking sensitivity using two approaches, viz. welding of monolithic thin sheet in controlled atmospheres, and, concurrently, development of aspiration-cast filler metal for weld overlay applications.

Welding of Thin Sheet in Controlled Atmospheres

To evaluate cold cracking in thin sheet material, we are using the sigmajig test fixture in a controlled atmosphere chamber, as shown in Figure 2. After welding, transverse stress is applied as in hot crack testing. The chamber can be evacuated to approximately 10^{-5} torr and backfilled with high purity inert gas; total oxygen and water vapor as impurities can be maintained at less than 50 ppm by volume. Controlled amounts of oxygen and/or water vapor can be added as desired. A single heat of a "simplified" Fe_3Al alloy (FA-185) has been used for all of the controlled atmosphere tests; its composition is 16% Al - 5% Cr - 0.1% C, balance iron (weight %).

Fig. 2. Sigmajig test fixture installed in controlled atmosphere chamber

Tests to date have shown:

- when welded in pure argon, no cold cracking occurs, even at post-weld stresses of approximately 20 ksi (138 MPa);
- when welded in argon-hydrogen mixtures (≤ 2% H_2), cracking occurs at intermediate stresses [8-16 ksi (55-110 MPa)]; and
- when welded in argon-water vapor mixtures, cracking occurs at low stresses [≤ 8 ksi(55 MPa)].

Since equal amounts of hydrogen or water vapor would be expected to charge the weld metal with equal amounts of dissolved hydrogen, these tests demonstrate that, as observed with base metal, cracking is primarily induced (after welding is completed) by environmental moisture. Additional confirmation of this mechanism was demonstrated by welding in pure argon and then introducing water vapor; at 15 ksi (103 MPa), rupture of the specimen occurred when the water vapor level reached 0.75%.

These observations are in agreement with tensile test results on base metal in varying atmospheres, with the exception that welds seem to be even more susceptible. We conclude that hydrogen cracking is still a problem with these alloys.

Development of Filler Metals for Weld Overlay Applications

Aspiration-cast filler metals have been produced both in-house and by a commercial supplier (Haynes International). Since some of the alloying elements are lost during deposition (particularly Al and Zr), and dilution from the substrate base metal must be accommodated, several iterations have been needed to arrive at the desired deposit composition. So far, successful weld overlay deposits (i.e. free of both hot and cold cracks) have been produced only with some compositions on some substrate materials. Figure 3 shows a crack-free deposit of a developmental iron aluminide composition on 2¼ Cr - 1 Mo alloy base plate. In all cases, preheat is required (350-400° C), interpass temperature must be maintained (≥ 350° C), and postweld heat treatment (≥ 750° C) is needed for stress relief.

Environmental Testing

An overlay clad deposit on 2¼ Cr- 1 Mo alloy made with one of the commercially-obtained filler metals was used for environmental testing. The deposit analysis was 21.2 Al, 2.88 Cr, 0.37 Nb, 0.4 Ti, 0.13 C, 0.51 Mo, 0.17 Zr, 70 PPM B, balance Fe, all in weight %. A corrosion coupon 0.6 mm thick, was cut from the top surface of the weld deposit, and exposed to a simulated coal gas containing 5.4% H_2S, 1.4% H_20, 79.4% H_2, balance argon (by volume) for 168 h at 800° C.

Weight changes of the weld clad, as shown in Figure 4, were extremely small, and visual examination showed only a superficial, tightly adhering oxide scale.

Also shown in the figure are the weight changes for a wrought Fe_3Al alloy (FAS) containing 28 atomic % Al + 2% Cr. The 28% Al alloy is representative of the most corrosion-resistant Fe_3Al alloy composition developed for service in the test atmosphere, and the weld clad [with 35.8 atomic % (21.2 weight %) Al] has essentially identical behavior. For comparison, the responses of an 18% Cr - 12% Al and a 27% Cr alloy are also shown.

Fig. 3. Iron aluminide weld overlay on 2¼ Cr - 1 Mo base plate using the gas tungsten arc (GTA) process. (magnification: 3.5x)

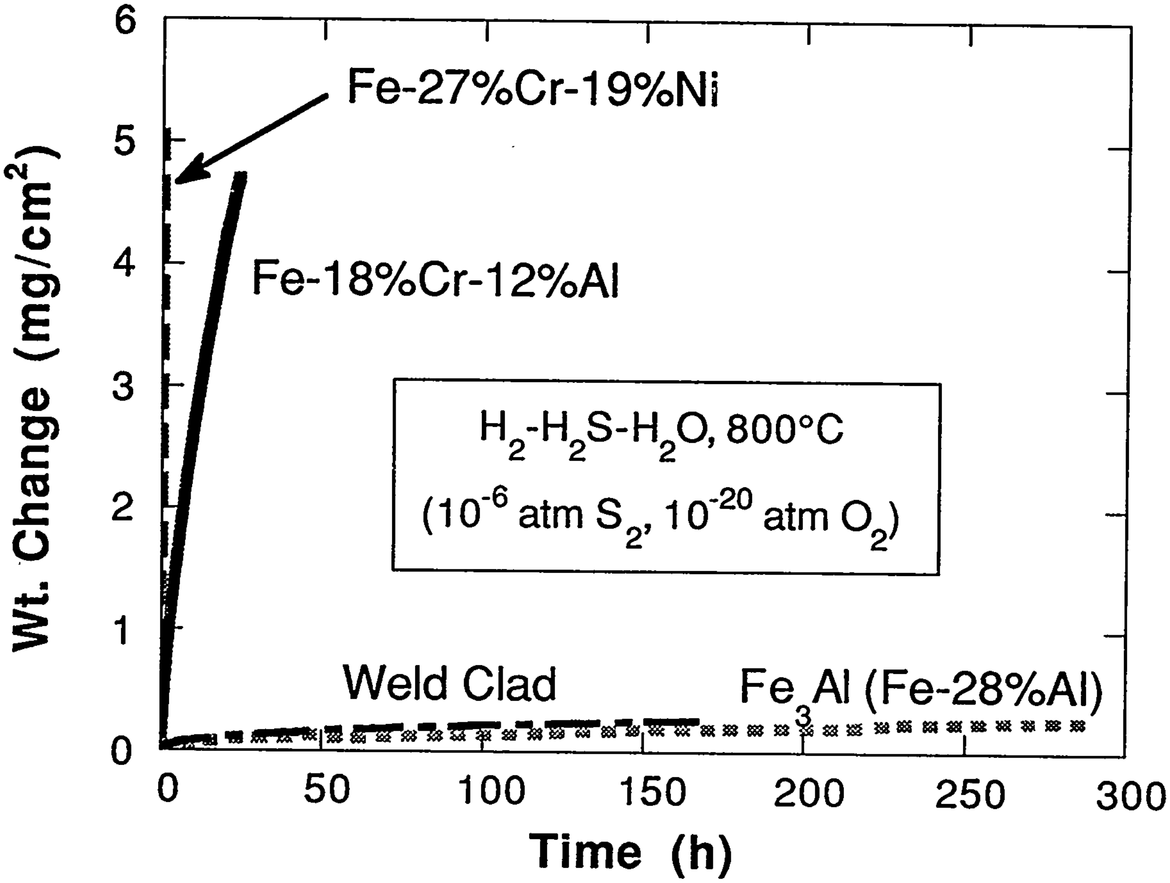

Fig. 4. Weight gain vs. time for several alloys in a simulated coal gas environment

CONCLUSIONS

From our studies to date, we can conclude:

- Hot cracking: occurrence is highly variable and needs continuing consideration; can be as good as some austenitic stainless steels. It is strongly affected by compositional effects.
- Cold cracking: its occurrence is still a concern requiring further study. It is currently only avoided by special measures including preheat and postweld heat treatment, and may limit structural applications of these alloys.
- Filler metal development: welding consumable production using the aspiration-casting approach needs additional development, but appears feasible.
- Environmental testing: developmental overlay clads can perform as well as wrought material in simulated coal gas environments at 800° C.